Study on the Physics of Metal/Si Interfaces in Si-based Spin Devices

Naoto Yamashita

Study on the Physics of Metal/Si Interfaces in Si-based Spin Devices

by

Naoto Yamashita

The cutting-edge technology based on silicon (Si) has constructed the information society. Miniaturization and integration have driven the evolution of electronic devices dealing with the heat issue. Spintronics has provided a new insight to bypass the issue by using the spin degree of freedom. In this field, Si is still indispensable: it has a long spin relaxation time due to the small atomic number and crystal inversion symmetry of the diamond structure with high quality, and the compatibility of the fabrication process with the electronic industry.

An important device in this field is the spin metal-oxide-semiconductor field-effect transistor (MOSFET); much effort has been paid to realize and make use of it in recent years. A major obstacle on the way to the application is the small magnetoresistance (MR) ratio, which is defined as the spin-dependent change in the resistance divided by the spin-independent parasitic resistance of the device. To increase the MR ratio of Si-based spin devices such as spin MOSFET, both of the two approaches are required: increase the numerator and decrease the denominator. Since the metal/Si interfaces are keys in both approaches as described in chapter 1, I studied the physics of the metal/Si interfaces.

Spintronics researchers have dedicated themselves to enhance the spin polarization of current in Si that dominates spin-dependence of the resistance in case of electrical spin injection. This electrical method to create spin current is vital to Si-based spin devices, and the spin polarization depends on the quality of the metal/Si interfaces. I found that thermal annealing at 300°C enhances spin signals two-fold. I also enhanced the thermal tolerance of the Si-based spin devices to 400°C, which provides the compatibility of the fabrication process with electronic devices. This theme is described in chapter 2.

To solve the heat issue, I focus on a spin caloritronic effect – the spin-dependent Seebeck effect, which is similar to the Seebeck effect at a ferromagnet/nonmagent interface. The spin-dependent Seebeck effect injects spin current from the ferromagnets to the nonmagnet using heat emitted by

the electronic device. I provided proof of the concept using a spin valve structure based on Si and evaluate the magnitude of the contribution to spin signal in a Si-based spin device. This theme is described in chapter 3.

I also focus on the resistance of metal/Si interfaces to decrease the spin-independent resistance. Generally, ferromagnetic metals such as Fe or Co is used as a ferromagnetic electrode to make spin current in Si. The Schottky barrier must appear in the interface because the work functions of these transition metals is higher than the electron affinity of Si. These barriers are detrimental to the spin polarization of current in the Si channel and the MR ratio. In conventional Si-based electronics, highly doped Si is applied to reduce the resistance of the metal/Si interface; however, highly doped Si is inappropriate for spin devices because the dense impurities degrade the spin polarization in the Si channel. The engineering on the metal side is required to keep the spin polarization and reduce the interface resistance. I suggest a way to realize two requirements at the same time by alloying Fe with Gd. I also discovered that the work function of Fe is decreased by more than 1.5 eV by adding Gd just 20%. This theme is described in chapter 4.

Finally, I combine three contributions to the MR ratio of Si-based spin devices and state the conclusion in chapter 5.

Acknowledgment

It would not be an overstatement, exaggeration, or cliche to say that I would not be here without the support of many who gave me insight, advice, encouragement, or unwittingly provided themselves as a positive role model. Here, I attempt to thank them.

I would first like to express my gratitude and sincere thanks to my supervisor, Prof. Masashi Shiraishi, whose expertise in whole of the modern condensed matter physics was invaluable in formulating the research questions and methodology. Your insightful feedback pushed me to sharpen my thinking and brush my work to a higher level.

I would like to thank Prof. Tsunenobu Kimoto, who is my advisor since I was an undergraduate student. I learned from you how interesting and useful semiconductors are.

I would like to thank Prof. Takashi Hikihara, who is my advisor. Your panoramic perception refined my work. I really enjoyed discussing with you every time.

I would like to thank Program-Specific Associate Prof. Yuichiro Ando. Your plentiful comments support me in overcoming numerous obstacles I have been facing through my research.

I would like to thank Mr. Hayato Koike and Dr. Tomoyuki Sasaki at TDK corporation for their kind comments. I would like to thank Prof. Yoshishige Suzuki at Osaka University, Associate Prof. Shinji Miwa at the University of Tokyo, and Assistant Prof. Minori Goto at Osaka University. It's an honor for me to be involved in the joint project on silicon spintronics. I could never conduct my Ph.D. research without your supports based on your unparalleled experimental skills.

I would like to thank Associate Prof. Syuta Honda at Kansai University, for his supporting my study from the theoretical aspects.

I would like to thank Dr. Eiichi Tamura and Dr. Teruya Shinjo for their invaluable comments. I would like to thank Assistant Prof. Mitsuaki Kaneko, Assistant Prof. Yasuyuki Kondo, Assistant Prof. Ryo Ohshima, and Assistant Prof. Ei Shigematsu at Kyoto University. Many experimental tips and valuable comments of yours improved my work a lot.

I would also like to thank Mrs. Ritsuko Mikage and Mrs. Yuko Hitomi.

I would like to thank Dr. Makoto Kameno and Dr. Sooboem Lee, who were members of the silicon group in the Shiraishi laboratory. It was a lot of fun for me to conduct experiments, discuss the results, and fit several Hanle curves with you. Your advice helped me and brushed up my study a lot.

I acknowledge the support from the Japan Society of the Promotion of Science (JSPS) Research Fellow Program (Grant No. 20J22776), Tateisi Science and Technology Foundation (Grant No. C2207007), and WISE Program "Innovation of Advanced Photonic and Electronic Devices" at Kyoto University. A part of this work was supported by Kyoto University Nano Technology Hub as a program of "Nanotechnology Platform" of the Ministry of Education, Culture, Sports, Science and Technology(MEXT), Japan, Grant Number A-20-KT-0017.

Finally, I would like to thank everyone involved with me. To those who have supported, encouraged, and trusted me.

Contents

List of Figures

Chapter 1

Introduction

In recent years, electronics researchers and engineers have struggled to address the heat issue of electronic devices. All of the electronic devices use the charge of electrons as an information carrier, which involves Joule heating in the devices themselves. The heat issue gets more significant because of technological, social, and economical reasons. The technological reason is brought by the everlasting evolution in integration and miniaturization of electronic circuits. Cutting-edge manufacturing technology realized the transistors of the gate length less than 10 nm, but the integration is hampered by the large heat density. The electronic circuits need a large area to be cooled. The social reason is the demand from modern society. In 2015, the United Nations adopted the statement that "By 2030, double the global rate of improvement in energy efficiency" as the goal 7.3 in SDGs (Sustainable Development Goals). The economical reason is to save batteries in mobile and wireless devices, which rapidly spread in the last decade. In a mobile device, the battery is the heaviest, the largest, and the most expensive part. Saving the battery becomes one of the advantages of the product such as a longer range of electric cars.

Many methods have been suggested to circumvent the heat issue and to improve the energy efficiency: wiring by light [1], power gating [2], and so on. Spintronics uses the spin angular momentum of electrons. The electron spins need no energy to store the information by using the spontaneous magnetization of ferromagnetic materials. Spintronic devices, which store, transport, and manipulate the electron spins, can address the heat issue of electronic devices [3]. Spin MOSFET, for example, allows making a memory bit with just a single transistor that is useful for energy-efficient in-memory

computing[4]. Therefore, spin devices attract many researchers in the fields of materials science and applied physics.

Because of its high potential for spintronics devices, I focused on a semiconducting material – silicon. In semiconductor-based spin devices, spin-polarized electrons propagate in the channel by drift or diffusion. During the propagation, momentum scattering and spin-orbit interactions disperse the electrons' spins[5]. The length scale of the relaxation is called the spin diffusion length or the spin transport length[6–8]. The time scale is called spin relaxation time, τ_{sf} (the basic theory of spin transport is described in Appendix A). Silicon (Si) has a long τ_{sf}, the highest quality in crystals among semiconductors, and nice compatibility with the mature technologies in the electronics industry. Figure 1.1 compares τ_{sf} of several materials and indicates the advantage of Si: the long τ_{sf} due to the small atomic number and the crystalline inversion symmetry.

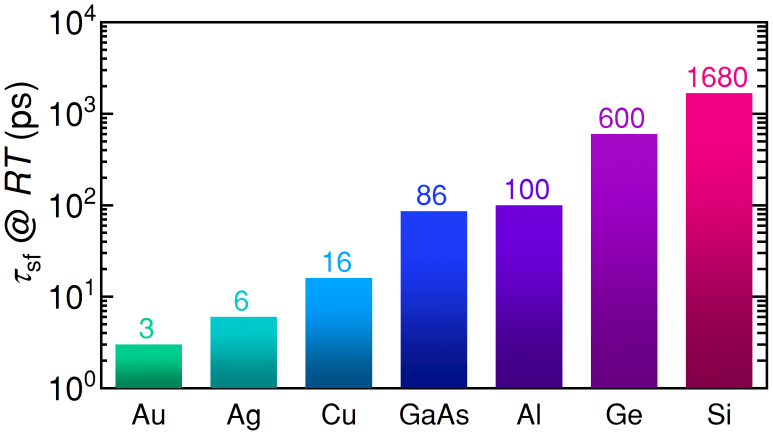

Figure 1.1: Comparison of spin relaxation time among typical materials

The values of the spin relaxation time, τ_{sf}, are measrued at room temperature. The values of Au[9], Ag[10], Cu[11], GaAs[12], Al[13], Ge[14], and Si[15] are quoted from the literatures.

Si-based spin devices have proved the potential, but the small magnetoresistance (MR) ratio hinders the straight way for application comparing with other devices without semiconductors[16,17]. To improve the MR ratio, a metal/Si interface plays a crucial role, so I studied three aspects of the interface: the effects of thermal annealing, the spin-dependent Seebeck effect, and the Schottky barrier. To make more spin currents in Si, I improved the spin polarization at the metal/Si interface

by thermal annealing (chapter 2). I also developed a new way to generate additional spin currents using joule heating – paraphernalia in the electronic devices (chapter 3). A Schottky barrier is an important problem at the metal/Si interfaces. I studied a way to reduce the Schottky barrier height of the ferromagnetic metal/Si interface (chapter 4). In chapter 5, I conclude this study and state the future vision of spin devices based on Si.

1.1 Spin Currents

1.1.1 Triggers of the Evolution of Spin Devices

The discovery of spin current gave birth to the field of spintronics. The giant magnetoresistance (GMR) effect was found and attributed to the spin current: the flow of electrons' spin [18]. The GMR of Fe/Cr multilayers is shown in Fig. 1.2 [18]. They found that "the resistivity is lowered by almost a factor of 2" in a magnetic field and "the magnetoresistance is still very significant at room temperature." [18] Many researchers were attracted by the large change of the resistance – the equivalent MR ratio of 100% at room temperature. The tunneling magnetoresistance (TMR) less attracts the researchers because the change of resistance was only 14% and detected only at a low temperature (4.2K) [19], although the effect was found earlier than GMR. The TMR at room temperature was observed in 1994 [20,21], which triggered the development race of the magnetoresistive random-access memories (MRAM). Hence, the target of the Si-based spin device should be an MR ratio of 100% at room temperature (300K). There is plenty of room for improvement because the state-of-the-art of MR ratio of Si-based spin device is 1.4% at room temperature [22].

1.1.2 Effect of Metal/Si Interfaces

The metal/Si interfacial physics is critical to the spin current in Si, which determines the MR ratio in Si based spin devices. An interface of the materials involving largely different resistivities, such as semiconductor and metal, reflects spin current that is a significant issue for making spin current in semiconductors — conductance mismatch [23]. Most of the ferromagnetic materials (even at 300K, which enables electrical spin injection to nonmagnetic materials) are transition metals such as Co, Fe, and Ni. These resistances are several orders lower than that of the semiconductors including Si, which

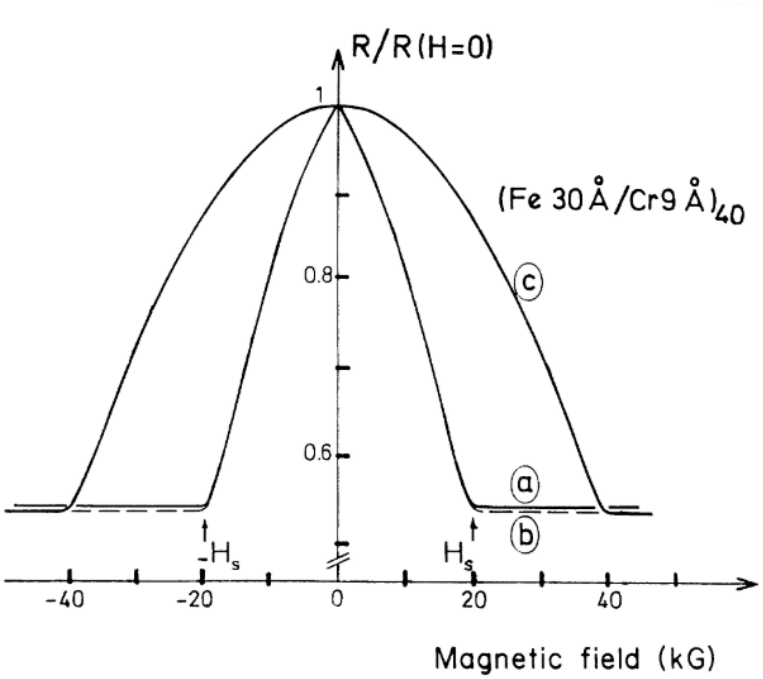

Figure 1.2: Giant magnetoresistance of Fe/Cr superlattices at 4K.

The value of R/R(H=0) varies from 0.5 to 1, which is equivalent to MR ratio of 100%. Each curve shows magnetoresistance in the different direction of the magnetic fields. The figure is quoted from [18].

arise the conductance mismatch [23]. When we apply an electric current on the metal/Si interface, the spins of ferromagnet are reflected at the interface and do not enter nor propagate in Si. Even if some spins are injected to Si, the spins also flow backward and the polarization is suppressed much [24]. To avoid the problem, a MgO tunnel barrier is often installed to the interface because the large resistance of the tunnel barrier blocks the backflows and reflection of spins [25]. Cutting-edge technology enabled to make 0.8 nm-thick MgO tunnel barrier and investigate the physics of spin transport in Si even at room temperature [15,16,26].

The essence of the spin polarization is spin coherent tunneling of MgO-based magnetic tunneling junctions (MTJs) [27,28]. A bcc Fe (0 0 1) layer can be epitaxially grown on a crystalline MgO (0 0 1) barrier, which enables the spin coherent tunnelling [29]. In the ideal case, Fe Δ_1 states are dominant to the tunnel current through the MgO barrier; the Fe Δ_1 band is fully spin-polarized at the Fermi level [29]. The coherent tunneling provides a large MR ratio of up to 200% at room temperature [30,31], which requires engineering of high-quality epitaxial growth of Fe/MgO interface. Since the structure is often applied to the ferromagnetic electrodes of the Si-based spin devices [32–34], understanding the physics of the ferromagnetic metal/Si interface including the tunneling barrier is necessary to achieve the target.

1.2 Spin Devices Based on Si

Silicon has a long spin relaxation time due to small spin-orbit coupling and lattice inversion symmetry. The spin-orbit coupling depends on the atomic number. The lattice inversion symmetry eliminates Dresselhaus spin-orbit interactions and spin scattering [15,35]. Many spintronics devices have been suggested using the benefits of Si [36–39].

An important spin device based on Si is spin metal-oxide-semiconductor field-effect-transistor (MOSFET), which has been proposed in 2004 [39] and picked up to a candidate for the beyond CMOS device in International Roadmap for Devices and Systems 2020. It has two functions to control the output: the gate voltage and the spin states. The spin-dependent output characteristics involve the function of nonvolatile memory, which enables the spin MOSFET to normally-off and energy-efficient computing [39]; therefore, many researchers have tackled the creation of the Si-based spin MOSFET [16,17,32,40,41]. A schematic image of the spin MOSFET is shown in Fig. 1.3a. It has a

similar structure as planer MOSFET consisting of source, drain, and gate electrodes applied on the Si channel. The main difference is the ferromagnetic material employed to the source and the drain electrodes to inject and detect spin current in the Si channel. A schematic image of the operating circuit and the characteristics are shown in Fig. 1.3b and Fig. 1.3c, respectively. The inputs are the gate voltage (V_{GS}) and the two spin states, and the output is the drain current (I_{SD}). The white arrows in Fig. 1.3c indicate the magnetization direction of these ferromagnetic electrodes. Parallel (P) is a spin state that their directions are the same; Antiparallel (AP) is a spin state that their directions are opposite. The spin states are switched by a magnetic field and the I_{SD} changes under a fixed voltage of V_{GS} depending on the spin states because the resistance is different in each state.

Two types of spin MOSFETs have been examined[42,43]: vertical type and lateral type. The vertical spin MOSFET has the surrounding gate structure (Fig. 1.3d); the lateral spin MOSFET has the back gate structure (Fig. 1.3e). Both types of devices have been investigated extensively, and the researchers have sought the best structure and materials for the application of spin MOSFETs[16,17,43–48].

1.2.1 Figure of Merits of Spin MOSFETs

Since spin MOSFETs have two mechanisms to modulate the spin current, two characteristics are required: MR ratio, G_s, and the on-off ratio of electrical current, G_e. The MR ratio G_s is defined as the resistance difference between two spin states (P and AP), ΔR_{s}, divided by the electrical resistance independent to the spin states R_0, which is expressed as:

$$G_s \equiv \frac{\Delta R_s}{R_0}. \tag{1.1}$$

More ΔR_{s} and less R_0 provide more MR ratio. The On-Off ratio G_e is defined as the ratio of the source-drain currents at on and off states switched by a gate voltage.

Figure 1.4a shows the comparison of spin MOSFETs' performance including vertical and lateral structures and shows the difficulty in the coexistence of high G_s and high G_e. The vertical spin MOSFETs provide better G_s than the lateral spin MOSFETs, but the G_e is several orders lower than that of the lateral spin MOSFETs. The trade-off is ascribable to the channel length of both structures. The vertical structure has a shorter semiconductor channel (less than a few nm) and a

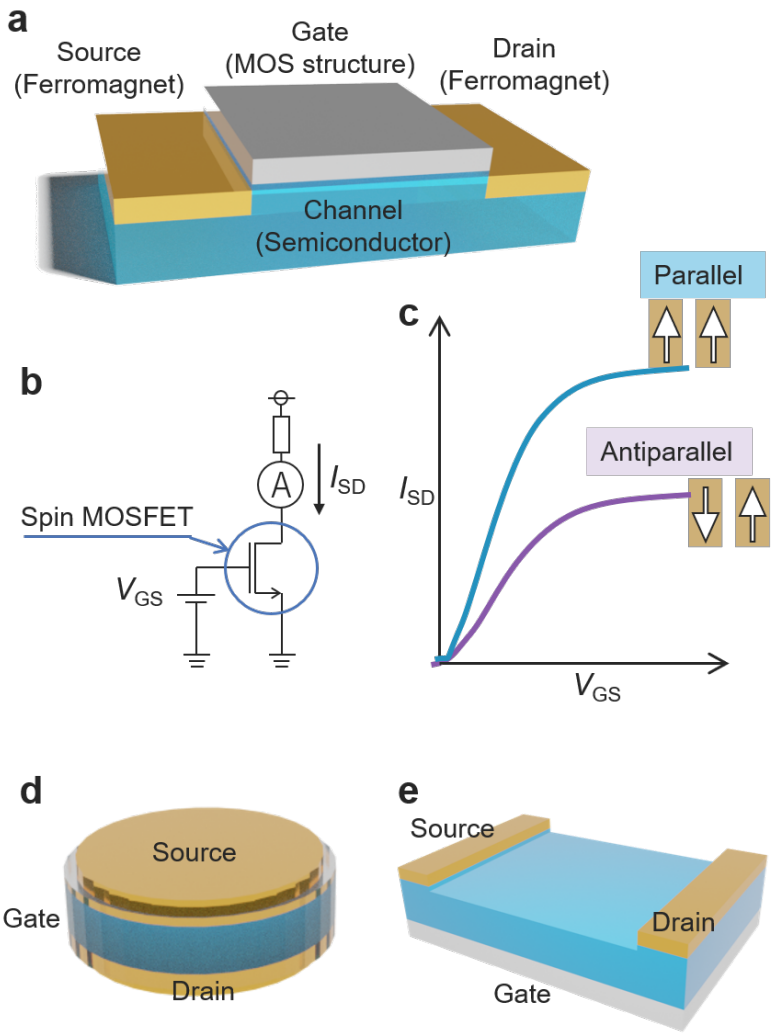

Figure 1.3: Schematic image of Si spin MOSFET.

(a) The structure of spin MOSFETs. **(b)** A example of the circuit including spin MOSFET. **(c)** An output characteristic of the spin MOSFET in the circuit (b). Both the gate voltage V_{GD} and the spin configuration (parallel and antiparallel) control the source-drain current I_{SD}. White arrows indicate the magnetization direction of each ferromagnetic electrode. **(d)** Schematic image of a vertical spin MOSFET. **(e)** Schematic image of a lateral spin MOSFET.

larger area of the current path than those of the lateral structure. The lateral structure provides higher G_e than the vertical structure mainly because of the uniform electric field in the channel because the semiconductor channel is thin enough (15 nm [46]) to be controlled by gate electric field. To enhance both G_s and G_e, miniaturization in structure is efficient for both vertical and lateral spin MOSFETs, but the trade-off remains. By making the smaller area of vertical structure (-100 nm^2), G_e will enhance because the gate electric field gets able to affect entire the channel, but the channel resistance increase and decrease G_s. By make the channel length shorter in lateral spin MOSFET (-100 nm^2), G_s will enhance because the channel resistance decrease, but the G_e decreases.

Here, I define a new parameter, the R factor to compare the total performance of the spin MOSFETs including G_s and G_e as shown in Fig. 1.4b. R is defined by the squared distance from the left bottom (10^{-1},10^{-3}) to each plot described by the following equation:

$$R \equiv \left(\frac{\log_{10} G_s + 3}{6}\right)^2 + \left(\frac{\log_{10} G_e + 1}{8}\right)^2 \tag{1.2}$$

The factors of 1/6 and 1/8 are the normalization coefficient for fair comparison of G_s and G_e. Si-based lateral spin MOSFETs evolve gradually and have reached R of 0.77 [46] in 2019, which is higher than that of any vertical spin MOSFETs. In addition, the large R operation was demonstrated at room temperature. These facts support a strong advantage of the Si lateral structure of the spin MOSFET application. The target is G_s of 100% and G_e of 10^6 at room temperature, which equivalent to R of more than 1.46; The Si-based lateral spin MOSFET requires improvement of G_s.

1.2.2 Lateral Spin Valves

A lateral spin valve (LSV) device is often used to study the spin currents in nonmagnetic materials including Si. A schematic image of the Si-based LSV is shown in Fig. 1.5a. It consists of a spin transport channel made of Si, two nonmagnetic electrodes on the ends of the channel (N1 and N2), and two ferromagnetic electrodes on the middle of the channel (F1 and F2). The structure includes the structure of the lateral type spin MOSFET and can be used to study the spin current and MR ratio of the spin MOSFET. By making spin current in the nonmagnetic materials, the spintronics researchers measure the spin polarization and the spin diffusion length, which can be evaluated by the spin signals measured by the non-local four terminals (NL4T) method or the local three terminals (L3T) method.

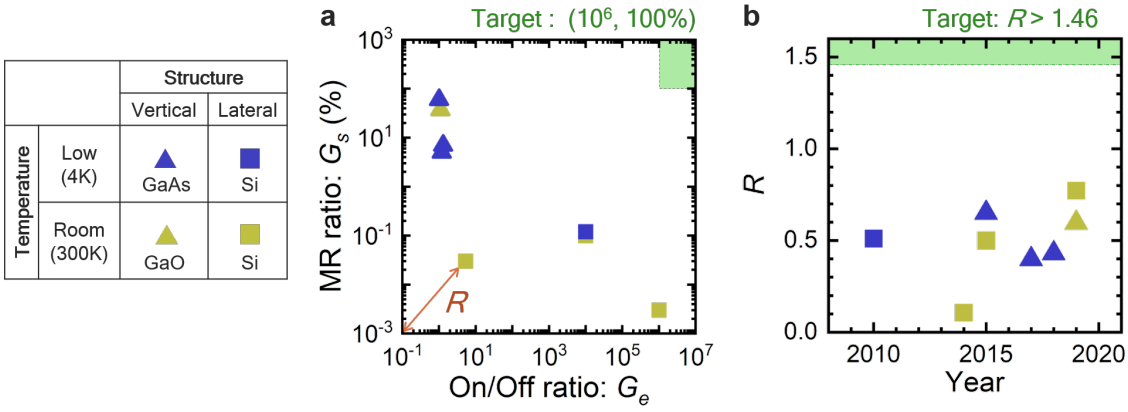

Figure 1.4: Benchmarking of spin MOSFETs.
The blue and yellow plots represent the value measured at low temperature (up to 4K) and room temperature. Squares and triangles mean that their structures of the spin MOSFETs are vertical and lateral, respectively. The materials of each plot were shown in the same box. The values were adopted from the literature[16,17,43–48] **(a)** Comparison of G_e and G_s. The orange allow indicate the example of the R factor defined in the Eq.(1.2). **(b)** Comparison of the R factors of spin MOSFETs.

To measure the spins propagated by diffusion, the NL4T method is generally used, a schematic image of which is shown in Fig. 1.5b. A current is applied on a ferromagnetic electrode to the neighboring nonmagnetic electrode. By the current, the spin current is injected from F2 and diffuse in the Si channel as shown in the black dashed arrows. A nonlocal voltage, V_{nl}, is measured at the other ferromagnetic electrode based on the other nonmagnetic electrode. To measure the spins propagated by drift, the L3T method is generally used, a schematic image of which is shown in Fig. 1.5c. A current is applied between the ferromagnetic electrodes to apply an electric field on the Si channel between F1 and F2. A voltage difference of the ferromagnetic electrode and the Si channel, $V_{3\mathrm{t}}$, is measured at a ferromagnetic electrode based on the neighboring nonmagnetic electrode. Although the configuration of NL4T and L3T methods are different, the shapes of the measured signals are similar, which is shown in Fig. 1.5d. In both schemes, the spin current propagates between F1 and F2, and the spin accumulation voltage is measured at a ferromagnetic electrode based on a nonmagnetic electrode. The spin transport in the channel can be confirmed by switching the magnetization configuration or spin states of P and AP since the spin accumulation voltage depends on it as described in Appendix A.

The spin states of P and AP is switched by the external magnetic field along the y direction, B_y. The blue and red lines in Fig. 1.5d are the spin accumulation voltages measured in the case of down sweep (from positive to negative) and up sweep (from negative to positive), respectively. The difference of the coercivities of F1 and F2 provides two symmetrical rectangular signals, which is evidence for the spin transport between them in the Si channel. The height of the rectangular signals is identical to the difference of the spin accumulation signals in P and AP, which is named the spin signal.

1.3 Purpose of the Study

The purpose of this thesis is to find ways to increase G_s and achieve the target of R of Si-based spin devices, which is a promising candidate as the energy-efficient device that solves the heat issue of modern electronics.

I draw my strategy in Fig. 1.6. There are two ways to enhance the MR ratio considering the definition of Eq.(1.1): increase ΔR_s and decrease R_0. The increasing of ΔR_s requires more spin current in Si. To make more spin current in Si, I examined two ways: thermal annealing and thermal spin injection. The topic of thermal annealing is described in chapter 2; The topic of thermal spin injection is described in chapter 3. The decrease of R_0 requires small resistance at metal/Si interfaces. To reduce the interface resistance, I reduce the Schottky barrier in the ferromagnet/Si interfaces, which is described in chapter 4. This plan needs more description because of the conductance mismatch, which is quantitatively described in Appendix A.6. A short channel length of less than 10 nm is a probable candidate for spin MOSFET in the future considering the evolution of electronic devices. In the future spin MOSFETs, the resistance of the Si channel is reduced, and the required interface resistance to avoid the conductance mismatch also decreases by a factor of 100. Thus, reduce RA is effective to enhance the MR ratio of the future lateral type spin MOSFETs. Finally, I stated the conclusion in chapter 5.

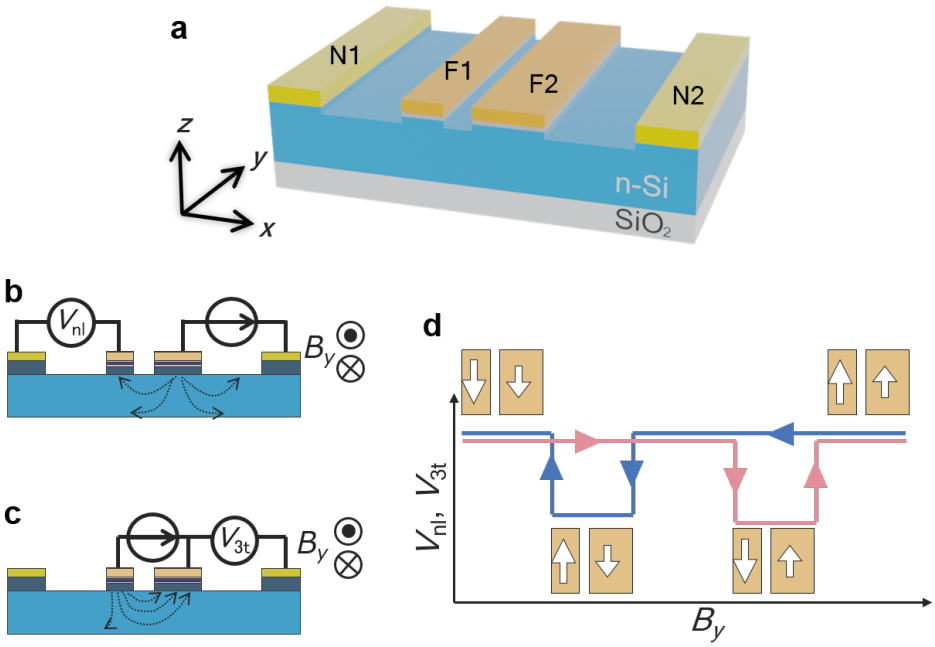

Figure 1.5: Schematic images of a lateral spin valve device and the measruement schemes of the spin currents

(a) A schematic image of a lateral spin valve device based on Si. The spin transport channel made of Si is shown as the light blue part on the SiO_2 layer shown in white. Four electrodes are installed on the Si channel. N1 and N2 are made of non magenteic metal such as Al or Ta. F1 and F2 are made of ferromagentic metal such as Fe or Co. There is a thin insulating layer (less than a few nm) made of MgO between the ferromagnetic metal and Si channel. The width of the F1 and F2 (the length of each electrode in the y direction) are different for obtaining different coercivities. The spin currents propagate between F1 and F2 along the Si channel. The distance of F1 and F2 in the x direction is called the length of the Si channel. **(b)** A configuration to measure diffusive pure spin currents in the Si channel, which is named as nonlocal four-terminal (NL4T) method. **(c)**A configuration to measure spin currents in the Si channel including spindrift effect, which is named as local three-terminal (L3T) method. **(d)** A schematic image of spin signals measured by NL4T and L3T methods (they provide apparently the same signals except for the polarity). By sweeping y direction magnetic field (B_y), the magnetization configurations are switched as parallel and antiparallel. The blue and red lines indicate the measured voltage when B_y is swept from positive to negative (called down sweep), and from negative to positive (up sweep), respectively. Two symmetrical rectangular signals appear after both sweeps if the spin currents propagate between F1 and F2. The height of the rectangular voltage signal is called the spin signal.

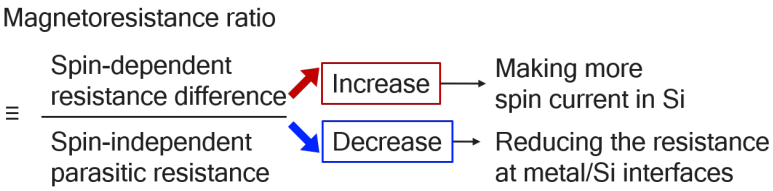

Figure 1.6: Logical strategy to improve MR ratio.

Chapter 2

Effects of Thermal Annealing on Metal/Si Interfaces in Spin Devices

In this chapter, I report the finding that thermal annealing enhances the spin signals by a factor of 2 in Si-based lateral spin valves. The spin polarization of the current increased because the annealing brought a well-textured interface of the ferromagnetic metal and MgO tunneling barrier, which is confirmed by X-ray diffraction spectroscopy. I also examined the mechanism of the thermal degradation of the metal/Si interfaces that is critical to the tolerance of the device. Metallic materials diffused from nonmagnetic electrodes to ferromagnetic electrodes along with the interface between the AlN capping layer and the Si channel. A thermally tolerant design of nonmagnetic electrodes, which improved the thermal tolerance of whole the device 100°C, was demonstrated.

Results presented in this chapter were published in the papers:

1. **N. Yamashita**, S. Lee, R. Ohshima, E. Shigematsu, H. Koike, Y. Suzuki, S. Miwa, M. Goto, Y. Ando, and M. Shiraishi, "Enhancement of spin signals by thermal annealing in silicon-based lateral spin valves", *AIP Advances* **10** 095021 (2020), selected as Editor ' s Pick. Published by AIP Publishing.
2. **N. Yamashita**, S. Lee, R. Ohshima, E. Shigematsu, H. Koike, Y. Suzuki, S. Miwa, M. Goto, Y. Ando, and M. Shiraishi, "Investigation of the thermal tolerance of silicon-based lateral spin valves", *Scientific Reports* **11** 10583 (2021). Published by Springer Nature.

2.1 Introduction and Motivation

Thermal annealing is often used to obtain large magnetoresistance (MR) in tunneling magnetoresistance (TMR) devices[29,31,49,50]. It improves the quality of the metal/tunneling barrier interfaces made of MgO tunneling barrier and bcc structure ferromagnetic metals (FMs)[29]. The results of TMR after annealing at different temperatures are compared in Fig. 2.1. The annealing at 360°C provided a large TMR ratio of 140% in the MTJ structure using CoFe and MgO[31]. Spin coherent tunneling enhances the spin polarization of tunneling current and TMR after the annealing, which is an advantage of the combination of the MgO tunnel barrier and the ferromagnetic metal (FM) having a bcc structure[29]. The structure is also employed to the ferromagnetic electrode of the Si-based spin devices; the thermal annealing may enhance the spin polarization and the MR ratio based on the same mechanism.

Some reported the appearance of the spin signals[51]; others reported the reduction of the spin signals of Si-based spin valves[52]. Post annealing temperature dependence of non-local four terminal (NL4T) signal in a previous study using Co_2FeSi/MgO/Mg/n^+-Si structure is shown in Fig. 2.2[52]. The signal decreased slightly after annealing at 350 °C and significantly after annealing at 400 °C (Fig. 2.2a). The annealing temperature dependence shows the reduction clearly (Fig. 2.2b). Another study compared spin signals of the structure of $Co_2Fe_{0.4}Mn_{0.6}Si$ and CoFe deposited on MgO/Mg/n^+-Si in the local three-terminal (L3T) geometry[51]. The spin signal was only detected after annealing at 350°C for $Co_2Fe_{0.4}Mn_{0.6}Si$ sample even at such a low temperature as 10K, whilst the CoFe sample shows spin signal without annealing. The authors claim thermal annealing at a proper temperature improves the structural ordering of the $Co_2Fe_{0.4}Mn_{0.6}Si$[51]. These two reports only discussed the structural ordering of the Heusler alloys; however, the physics behind the spin polarization of them is different from that of the bcc FMs. In the former case, the spin polarization depends on the band structures of the Heusler alloys. In the latter case, the spin polarization depends on the coherent tunneling due to perfect spin polarization of Δ_1 band in bcc FMs[29]. Thermal annealing still has the potential to increase spin signals and MR ratio of the bcc structure FM/MgO/Si-based spin devices. Here I study the effect of thermal annealing on the spin polarization at the bcc FM/MgO/Si structure.

In this chapter, the effect of thermal annealing on the Si-based lateral spin valve has been investigated. I found the thermal annealing at 300°C enhances the spin signal and disclosed the mechanism

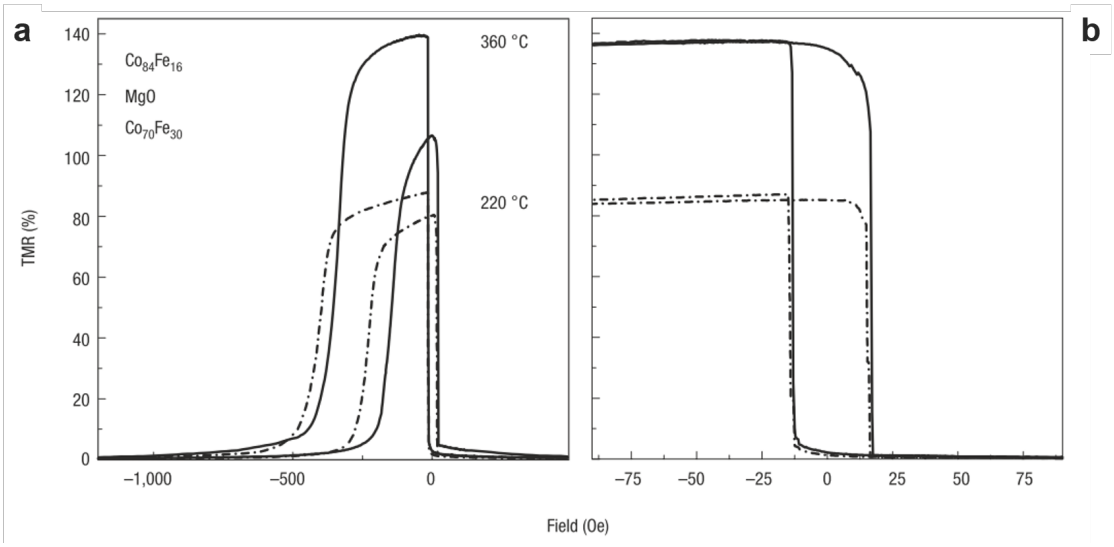

Figure 2.1: Effects on thermal annealing on the magnetic tunnel junction made of CoFe/MgO/CeFe This figure is quoted from [31].

of thermal degradation of the device.

The theory of the spin transport in the LSV is described in the theoretical part § 2.2.1. The first of the experimental part § 2.3 shows the procedure of the sample structures and the sequence of experiments. Then, I discuss the results and deduced the mechanism of the thermal degradation. In § 2.5, I summarize this chapter and evaluate how much thermal annealing improves the MR ratio of Si-based spin devices.

2.2 Spin Currents in Si

Here, I describe the theory of the spin transport and the spin signal detected in a LSV based on the spin diffusion equation, the details of which are described in Appendix A.3 [6].

2.2.1 One-dimentional Model of Lateral Spin Valves

I use the one-dimensional model of the spin valve as shown in Fig. 2.4 defining five regions (F1, F2, N3, N4, and N5), which is generally used in the analysis of the spin current in the LSV [26,53]. Charge

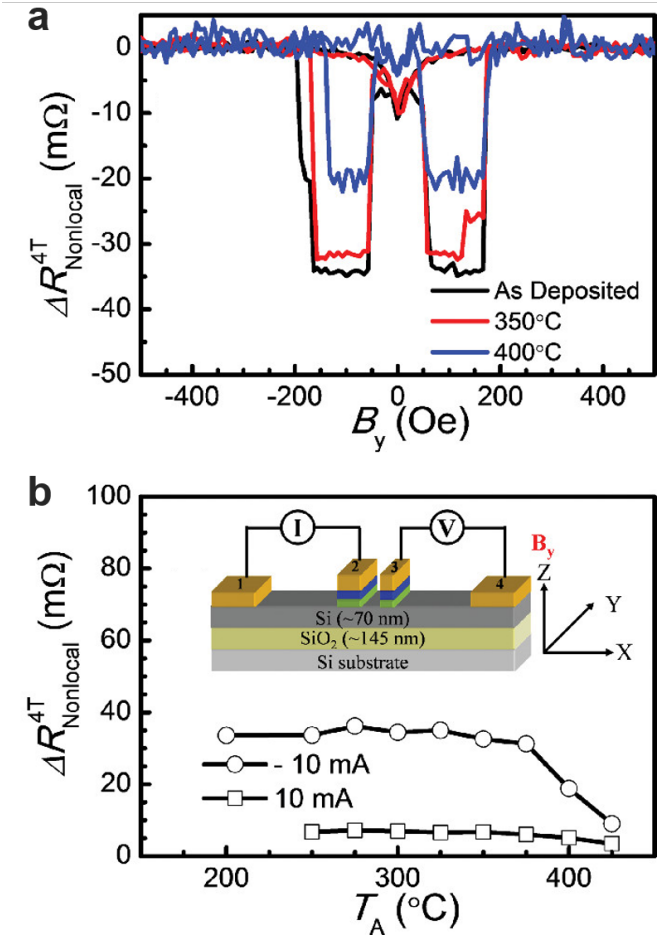

Figure 2.2: Effects on thermal annealing on Si-based spin device. This figure is quioted from [52].

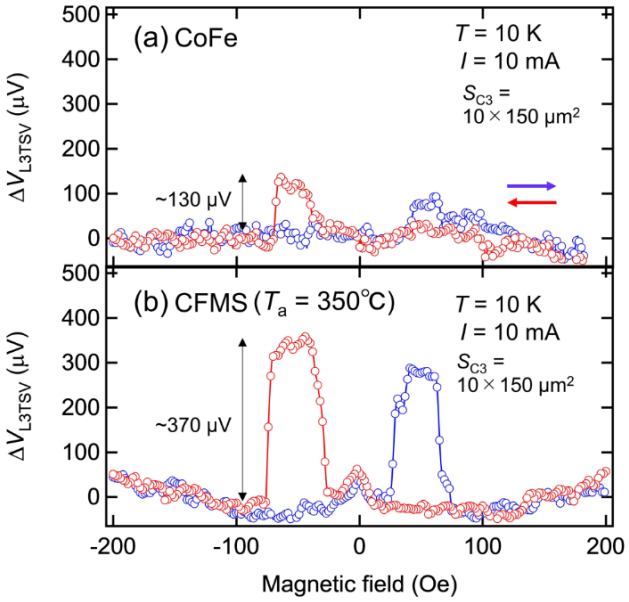

Figure 2.3: CoFe and CFMS annealed at 350 °C on Si spin devices. The figure is quoted from [51].

current is applied from F2 to N5 and spins diffuse along N3 from $x = L$ to $x = 0$ without the spindrift effect.

I start from the spin diffusion equation [54]:

$$\nabla^2(n_\uparrow - n_\downarrow) - \frac{n_\uparrow - n_\downarrow}{\lambda_{\rm N}^2}, \tag{2.1}$$

where, $n_\uparrow$ and $n_\downarrow$ are the up and down electron density, respectively, and $\lambda_{\rm N}$ is the spin diffusion length of the nonmagnetic material, Si channel. By using the spin-dependent conductivity for the up (down) spin, $\sigma_{\uparrow(\downarrow)}$, the spin-dependent voltage, $V_{\uparrow(\downarrow)}$, and the spin current, $J_{\uparrow(\downarrow)} = -\sigma_{\uparrow(\downarrow)}\nabla V_{\uparrow(\downarrow)}$, in each region are expressed as follows [26]:

- F1 ($x_{\rm F} < 0$)

$$V_{\rm F1\uparrow(\downarrow)} = (-)\frac{\sigma_{\rm F1\downarrow(\uparrow)}}{\sigma_{\rm F1}} \exp\left(-\frac{x_{\rm F}}{\lambda_{\rm F1}}\right)\frac{V_1}{2} + D, \tag{2.2}$$

$$J_{\rm F1\uparrow(\downarrow)} = (-)\frac{1}{R_{\rm F1}} \exp\left(-\frac{x_{\rm F}}{\lambda_{\rm F1}}\right)\frac{V_1}{2} + D, \tag{2.3}$$

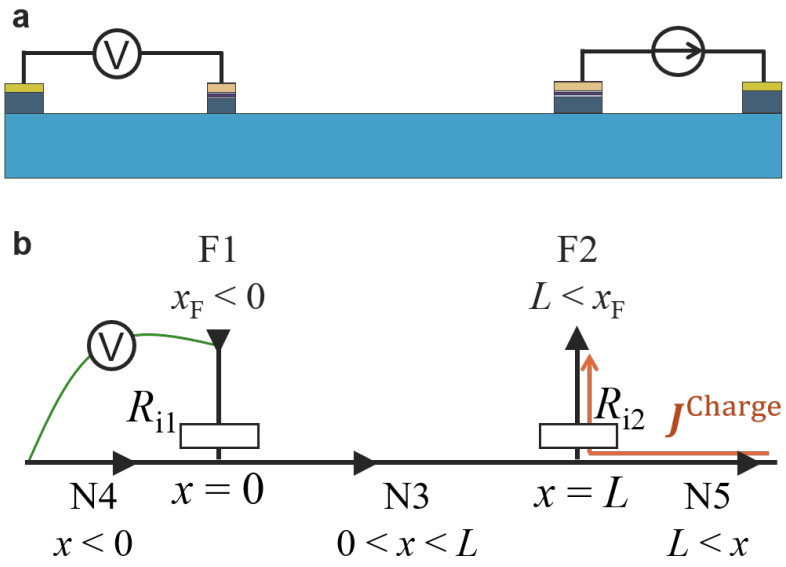

Figure 2.4: One-dimentional model of Si-based lateral spin devices.

(a) The schematic side view of the non-local four terminal measurement using a Si-based lateral spin valve. **(b)** One-dimentional model of the Si-based lateral spin valve.

- F2 ($x_{\mathrm{F}} > L$)

$$V_{\mathrm{F2}\uparrow(\downarrow)} = -\frac{J}{\sigma_{\mathrm{F2}}} x_{\mathrm{F}} + (-)\frac{\sigma_{\mathrm{F2}\downarrow(\uparrow)}}{\sigma_{\mathrm{F2}}} \exp\left(-\frac{x_{\mathrm{F}} - L}{\lambda_{\mathrm{F2}}}\right) \frac{V_2}{2} - E, \tag{2.4}$$

$$J_{\mathrm{F2}\uparrow(\downarrow)} = \frac{J}{\sigma_{\mathrm{F2}}} \mathrm{F2} \uparrow (\downarrow) - (+)\frac{1}{R_{\mathrm{F2}}} \exp\left(-\frac{x_{\mathrm{F}} - L}{\lambda_{\mathrm{F2}}}\right) \frac{V_2}{2} - E, \tag{2.5}$$

- N3 ($0 < x < L$)

$$V_{\mathrm{N3}\uparrow(\downarrow)} = (-)\exp\left(-\frac{x}{\lambda_{\mathrm{N}}}\right) \frac{V_3^+}{2} + (-)\exp\left(-\frac{x - L}{\lambda_{\mathrm{N}}}\right) \frac{V_3^-}{2}, \tag{2.6}$$

$$J_{\mathrm{N3}\uparrow(\downarrow)} = (-)\frac{1}{R_{\mathrm{N}}}\exp\left(-\frac{x}{\lambda_{\mathrm{N}}}\right) \frac{V_3^+}{2} + (-)\frac{1}{R_{\mathrm{N}}}\exp\left(-\frac{x - L}{\lambda_{\mathrm{N}}}\right) \frac{V_3^-}{2}, \tag{2.7}$$

- N4 ($x < 0$)

$$V_{\mathrm{N4}\uparrow(\downarrow)} = (-)\exp\left(-\frac{x}{\lambda_{\mathrm{N}}}\right) \frac{V_4}{2}, \tag{2.8}$$

$$J_{\mathrm{N4}\uparrow(\downarrow)} = (-)\frac{1}{R_{\mathrm{N}}}\exp\left(-\frac{x}{\lambda_{\mathrm{N}}}\right) \frac{V_4}{2}, \tag{2.9}$$

- N5 ($x > L$)

$$V_{\mathrm{N5}\uparrow(\downarrow)} = -\frac{J}{\sigma_{\mathrm{N}}} x + (-)\exp\left(-\frac{x - L}{\lambda_{\mathrm{N}}}\right) \frac{V_5}{2}, \tag{2.10}$$

$$J_{\mathrm{N5}\uparrow(\downarrow)} = -\frac{1}{2} J + (-)\frac{1}{R_{\mathrm{N}}}\exp\left(-\frac{x - L}{\lambda_{\mathrm{N}}}\right) \frac{V_5}{2}, \tag{2.11}$$

where, $R_{\mathrm{F1(2)}} = \left(\frac{1}{\sigma_{\mathrm{F1(2)}\uparrow}} + \frac{1}{\sigma_{\mathrm{F1(2)}\downarrow}}\right)\lambda_{\mathrm{F}}$ and $R_{\mathrm{N}} = 2\lambda_{\mathrm{N}}/\sigma_{\mathrm{N}}$. The spin-dependent conductivities are described with the spin polarizations of F1 (α_{F1}) and F2 (α_{F2}) as $\sigma_{\mathrm{F1}\uparrow(\downarrow)} = \frac{1+(-)\alpha_{\mathrm{F1}}}{2}\sigma_{\mathrm{F1}}$ and $\sigma_{\mathrm{F2}\uparrow(\downarrow)} = \frac{1+(-)\alpha_{\mathrm{F2}}}{2}\sigma_{\mathrm{F2}}$, respectively. λ_{FM} is the spin diffusion length of the FM material, L is the center-to-center distance between F1 and F2, σ_{N} is the conductivity of the channel, $\sigma_{\mathrm{F1(2)}}$ is the conductivity of the FM materials of F1(2), and J is the current density. $V_1, V_2, V_3^-, V_3^+, V_4$, and V_5 are constant values. The boundary conditions of the spin-dependent voltages and currents at $x = x_{\mathrm{F}} = 0$ and $x = x_{\mathrm{F}} = L$ are given by Kirchhoff's laws as follows:

- $x = x_{\mathrm{F}} = 0$

$$\frac{\sigma_{\mathrm{F1}\downarrow}}{\sigma_{\mathrm{F1}}}\frac{V_1}{2} - R_{\mathrm{i1}\uparrow}\left(\frac{V_1}{2R_{\mathrm{F1}}}\right) + D = \frac{V_4}{2} = \frac{V_3^+}{2}\eta + \frac{V_3^-}{2}, \tag{2.12}$$

$$-\frac{\sigma_{\mathrm{F1}\uparrow}}{\sigma_{\mathrm{F1}}}\frac{V_1}{2}+R_{\mathrm{i1}\downarrow}\left(\frac{V_1}{2R_{\mathrm{F1}}}\right)+D=-\frac{V_4}{2}=-\frac{V_3^+}{2}\eta-\frac{V_3^-}{2}, \tag{2.13}$$

$$\frac{V_1}{2R_{\mathrm{F1}}}+\frac{V_4}{2R_{\mathrm{N}}}=\frac{V_3^+}{2R_{\mathrm{N}}}\eta-\frac{V_3^-}{2R_{\mathrm{N}}}, \tag{2.14}$$

$$-\frac{V_1}{2R_{\mathrm{F1}}}-\frac{V_4}{2R_{\mathrm{N}}}=-\frac{V_3^+}{2R_{\mathrm{N}}}\eta+\frac{V_3^-}{2R_{\mathrm{N}}}, \tag{2.15}$$

- $x=x_{\mathrm{F}}=L$

$$\frac{\sigma_{\mathrm{F2}\downarrow}}{\sigma_{\mathrm{F2}}}\frac{V_2}{2}-R_{\mathrm{i2}\uparrow}\left(\frac{\sigma_{\mathrm{F2}\uparrow}}{\sigma_{\mathrm{F2}}}J+\frac{V_2}{2R_{\mathrm{F2}}}\right)-E=\frac{V_5}{2}=\frac{V_3^+}{2}+\frac{V_3^-}{2}\eta, \tag{2.16}$$

$$-\frac{\sigma_{\mathrm{F2}\uparrow}}{\sigma_{\mathrm{F2}}}\frac{V_2}{2}-R_{\mathrm{i2}\downarrow}\left(\frac{\sigma_{\mathrm{F2}\downarrow}}{\sigma_{\mathrm{F2}}}J+\frac{V_2}{2R_{\mathrm{F2}}}\right)-E=-\frac{V_5}{2}=-\frac{V_3^+}{2}-\frac{V_3^-}{2}\eta, \tag{2.17}$$

$$\frac{\sigma_{\mathrm{F2}\uparrow}}{\sigma_{\mathrm{F2}}}J-\frac{V_2}{2R_{\mathrm{F2}}}=\frac{V_5}{2R_{\mathrm{N}}}+\frac{J}{2}+\frac{V_3^+}{2R_{\mathrm{N}}}-\frac{V_3^-}{2R_{\mathrm{N}}}\eta, \tag{2.18}$$

$$\frac{\sigma_{\mathrm{F2}\downarrow}}{\sigma_{\mathrm{F2}}}J+\frac{V_2}{2R_{\mathrm{F2}}}=-\frac{V_5}{2R_{\mathrm{N}}}+\frac{J}{2}-\frac{V_3^+}{2R_{\mathrm{N}}}+\frac{V_3^-}{2R_{\mathrm{N}}}\eta, \tag{2.19}$$

where, $\exp\left(-\frac{L}{\lambda_{\mathrm{N}}}\right)=\eta$. D and E are the voltages generated by the spin accumulation at $x=0$ and L, respectively. The interface resistances depending on the spin are described as $R_{\mathrm{i1}\uparrow(\downarrow)}=\frac{2}{1-(+)\beta_1}R_{\mathrm{i1}}$ and $R_{\mathrm{i2}\uparrow(\downarrow)}=\frac{2}{1-(+)\beta_2}R_{\mathrm{i2}}$ by using spin polarization of the interfaces β_1 and β_2. I calculate the voltage at F1 as:

$$D=-\frac{(1-\beta_1^2)R_{\mathrm{F1}}\alpha_1+4\beta_1R_{\mathrm{i1}}}{2(1-\beta_1^2)R_{\mathrm{N}}}V_3^-, \tag{2.20}$$

where

$$\begin{aligned}V_3^- &= -\frac{R_{\mathrm{N}}\eta}{\left\{\frac{2}{R_{\mathrm{N}}}+\frac{2(1-\beta_2^2)}{(1-\beta_2^2)R_{\mathrm{F2}}+4R_{\mathrm{i2}}}\right\}\left(R_{\mathrm{N}}+R_{\mathrm{F1}}+\frac{4R_{\mathrm{i1}}}{1-\beta_1^2}\right)-\frac{2(1-\beta_2^2)R_{\mathrm{N}}\eta^2}{(1-\beta_2^2)R_{\mathrm{F2}}+4R_{\mathrm{i2}}}}\\ &\quad\times\left\{\alpha_2-\frac{2(1-\beta_2^2)}{(1-\beta_2^2)R_{\mathrm{F2}}+4R_{\mathrm{i2}}}\frac{R_{\mathrm{i2}\uparrow}\sigma_{\mathrm{F2}\uparrow}-R_{\mathrm{i2}\downarrow}\sigma_{\mathrm{F2}\downarrow}}{\sigma_{\mathrm{F2}}}\right\}J\end{aligned} \tag{2.21}$$

Because the spin resistance of a ferromagnet is much smaller than that of the interface resistance ($R_{\mathrm{F2}}\ll R_{\mathrm{i2}}$), I assumed $\frac{(1-\beta_2^2)R_{\mathrm{F2}}}{R_{\mathrm{i2}}}\simeq 0$, and I calculate the second member of Eq.(2.21) $\{\ldots\}$ as

$$\{\ldots\}=\alpha_2-\frac{4R_{\mathrm{i2}}(\alpha_2-\beta_2)}{(1-\beta_2^2)R_{\mathrm{F2}}+4R_{\mathrm{i2}}}=\frac{\frac{\alpha_2(1-\beta_2^2)R_{\mathrm{F2}}}{R_{\mathrm{i2}}}+4\alpha_2-4\alpha_2+4\beta_2}{\frac{(1-\beta_2^2)R_{\mathrm{F2}}}{R_{\mathrm{i2}}}+4}\simeq\beta_2. \tag{2.22}$$

Similarly, by assuming $R_{\rm F1} \ll R_{\rm i1}$, and $\frac{(1-\beta_1^2)R_{\rm F1}}{R_{\rm i1}} \simeq 0$, I obtain

$$\begin{aligned} D &\simeq -\frac{2\beta_1 R_{\rm i1}}{(1-\beta_1^2)R_{\rm N}} V_3^- \\ &= \frac{1}{2}\frac{\beta_1\beta_2\eta J}{\left(\frac{2}{R_{\rm N}}+\frac{1-\beta_2^2}{2R_{\rm i2}}\right)\left\{\frac{(1-\beta_1^2)R_{\rm N}}{4R_{\rm i1}}+1\right\}-\left\{\frac{1-\beta_2^2}{2R_{\rm i2}}\right\}\left\{\frac{1-\beta_1^2}{4R_{\rm i1}}\right\}R_{\rm N}\eta^2} \end{aligned} \tag{2.23}$$

I set $V_{\rm nl}^{\rm P} = D^{\rm P} = D(\beta_1, \beta_2)$ for the parallel state and $V_{\rm nl}^{\rm AP} = D^{\rm AP} = D(\beta_1, -\beta_2)$ for the antipalallel state. From Eq.(2.23), $D^{\rm AP} = -D^{\rm P}$. The spin signal in the NL-4T configuration is expressed as:

$$\begin{aligned} \Delta V_{\rm nl} &= V_{\rm nl}^{\rm P} - V_{\rm nl}^{\rm AP} = D^{\rm P} - D^{\rm AP} = 2D \\ &= \frac{\beta_1\beta_2\eta J}{\left(\frac{2}{R_{\rm N}}+\frac{1-\beta_2^2}{2R_{\rm i2}}\right)\left\{\frac{(1-\beta_1^2)R_{\rm N}}{4R_{\rm i1}}+1\right\}-\left\{\frac{1-\beta_2^2}{2R_{\rm i2}}\right\}\left\{\frac{1-\beta_1^2}{4R_{\rm i1}}\right\}R_{\rm N}\eta^2}. \end{aligned} \tag{2.24}$$

I also assumed $1-\beta_1^2 = 1-\beta_2^2 = \simeq 1$ to obtain a simpler expression:

$$\begin{aligned} \Delta V_{\rm nl} &= \frac{\beta_1\beta_2 G_{\rm N} J}{\left(G_{\rm N}+\frac{1}{2}G_{\rm i1}\right)\left(G_{\rm N}+\frac{1}{2}G_{\rm i2}\right)\eta^{-1}-\frac{1}{4}G_{\rm i1}G_{\rm i2}\eta} \\ &= \frac{\beta_1\beta_2 J}{\left\{G_{\rm N}+\frac{1}{2}(G_{\rm i1}+G_{\rm i2})+\frac{G_{\rm i1}G_{\rm i2}}{4G_{\rm N}}\right\}\eta^{-1}-\frac{G_{\rm i1}G_{\rm i2}}{4G_{\rm N}}\eta}. \end{aligned} \tag{2.25}$$

Here, I set the spin conductance of N and the interface as $G_{\rm N} \equiv \frac{2}{R_{\rm N}} = \frac{\sigma_{\rm N}}{\lambda_{\rm N}}$ and $G_{\rm i1(2)} \equiv \frac{1}{R_{\rm i1(2)}}$, respectively. Finally by putting $\beta_1 = \beta_2 = \beta$, we obtain the spin signal as:

$$\Delta V_{\rm nl} = \frac{\beta^2 J}{\left\{G_{\rm N}+\frac{1}{2}(G_{\rm i1}+G_{\rm i2})+\frac{G_{\rm i1}G_{\rm i2}}{4G_{\rm N}}\right\}\exp(\frac{L}{\lambda_{\rm Si}})-\frac{G_{\rm i1}G_{\rm i2}}{4}\exp(-\frac{L}{\lambda_{\rm Si}})} \tag{2.26}$$

2.3 Experimental Details

2.3.1 Experimental Procedure

The experimental procedure is shown in Fig. 2.5. To study the effects of thermal annealing on the Si-based spin devices, the annealing was carried out after fabricating whole the devices. Electrical measurements including *I*-*V* and NL4T measurements were carried out at room temperature (RT) before and after the annealing. I focused on the *I*-*V* characteristics of ferromagnetic electrodes to

examine the metal/Si interfaces including MgO tunneling barriers. After the thermal annealing, the same measurements were carried out at RT. The experiments were repeated with increasing annealing temperature until the spin signal disappeared. The sample was examined by transmission electron microscopy (TEM) and energy dispersion X-ray spectroscopy (EDX) to investigate the mechanism of the thermal degradation. I successfully determined the mechanism and improved the thermal tolerance of the device.

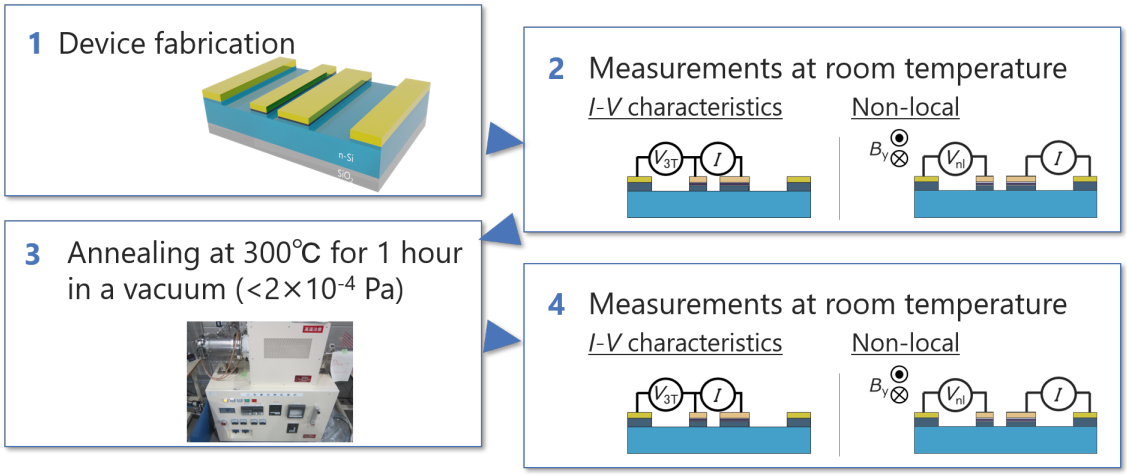

Figure 2.5: Outline of a sequence of the experiments to study the effects of thermal annealing on the Si-based spin devices

2.3.2 Sample Structure

Two types of Si-based LSVs were prepared, which are schematically shown in Fig. 2.6. The difference between samples A and B is the structure of the nonmagnetic electrodes: Sample A has the Au(150 nm)/Ta(3 nm)/Al (40 nm) structure; Sample B has the Au(150 nm)/Ta(40 nm) structure. The reason for the difference will be described later. The spin valve structures were fabricated on a silicon-on-insulator substrate with a 100-nm-thick Si(1 0 0) layer/ 200-nm-thick SiO_2/ 625-μm-thick Si(1 0 0) substrate. Phosphorus (P) atoms were doped into the top Si layer by the ion implantation technique to form the n-Si and n^+-Si layers. Then, rapid thermal annealing was carried out for their activation. The dopant concentration in the Si channel was confirmed by secondary ion mass spectrometry, which showed a small distribution perpendicular to the plane in the range of 1×10^{17}

to 2×10^{18} cm^{-3}, indicating nondegenerate Si. The dopant concentration of the 20-nm-thick n$^+$-Si layer was 5×10^{19} cm^{-3}, which was employed to suppress the width of the depletion layer at the ferromagnetic contacts. The ferromagnetic contacts F1 and F2 were fabricated by electron beam evaporation in an ultrahigh vacuum. Electron beam lithography and Ar$^+$-ion milling were carried out to define the F1 and F2 and remove the n$^+$-Si on the channel regions. AlN was deposited on the Si channel as a capping layer. Finally, NM electrodes (N1 and N2) were fabricated by electron beam lithography and ion beam deposition. The samples were fabricated and provided by the TDK corporation and Osaka University.

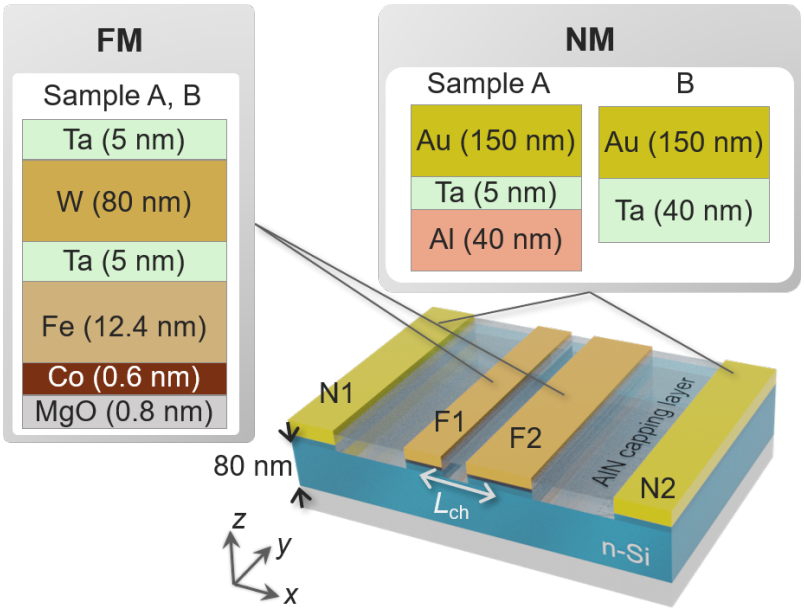

Figure 2.6: Schematic of Si-based lateral spin valves.

2.4 Effects of Thermal Annealing on Spin Signals

2.4.1 Annealing at 300°C

First, to investigate the effect of thermal annealing, sample A was employed in the experiments. NL4T measurements and I-V measurement were carried out. The devices possessing different channel lengths, L, were examined to confirm the exponential decay of the spin signals and estimate the spin

polarization in the Si channel.

I measured the interface resistances of F1 and F2. The voltage drop, V_{3T}, at F1 and F2 as a function of the bias current I is plotted in Figs. 2.7a and 2.7b. The measurement configurations are shown in each inset. Nonlinear I-V_{3T} characteristics were obtained for both electrodes, indicating the contribution of the tunneling current. The interface resistance was slightly increased by thermal annealing, especially for F2. A similar behavior (a slight increment in the interface resistance after annealing) was observed for all devices with different L. Here, I focus on the resistance area products of F1 (RA_1) and F2 (RA_2) at $I = 0$ mA and 0.3 mA, respectively, because they are the same condition as the spin transport experiments, which will be discussed below. While RA_1 at $I = 0$ mA did not change after annealing, as shown in the inset of Fig. 2.7a, RA_2 at $I = 0.3$ mA slightly increased from 17 kΩμm^2 to 18 kΩμm^2 as shown in the inset of Fig. 2.7b.

Nonlocal four terminals measurement was performed. A direct current of 0.3 mA is applied on F2 (used as a spin injector), and the spin accumulation voltage V_{nl} was measured at F1 (used as a spin detector) because no significant difference in spin signals is generally obtained even for the F1 spin injector and F2 spin detector. An external magnetic field was applied along the y-direction, which was used to switch the magnetization configurations of F1 and F2. The spin accumulation signals before the annealing are shown as the black dots in Fig. 2.8a. The center-to-center distance between two FMs, L, was 1.6 μm. A clear rectangular hysteresis signal with steep voltage changes corresponding to magnetization reversal was obtained. The magnitude of the spin accumulation signal, ΔV_{nl}, was 12 μV. Clear spin signals were also observed after the annealing at 300°C as shown in red plots in Fig. 2.8a. The spin signals were increased after the annealing by a factor of 2: from 12 μV to 24 μV.

This significant enhancement of the spin signal in the Si-based lateral spin valve is found for the first time. Because the annealing temperature is much less than the melting point of the metallic films nor the Si, the enhancement is attributable to the interfaces of the Si channel and ferromagnetic electrodes. I obtained the enhancement in ΔV_{nl} for devices on another Si substrate, the thermal annealing of which was carried out on different occasions to check the repeatability of the annealing effect. The enhancement of ΔV_{nl} is a general feature for these Si-based spin devices.

From the L dependence of the spin signal shown in Fig. 2.8b, the spin polarization and spin diffusion length in the Si channel were estimated. Using a one-dimensional model and assuming the spin polarization of tunneling junction is dominant, the spin polarization, β, and spin diffusion

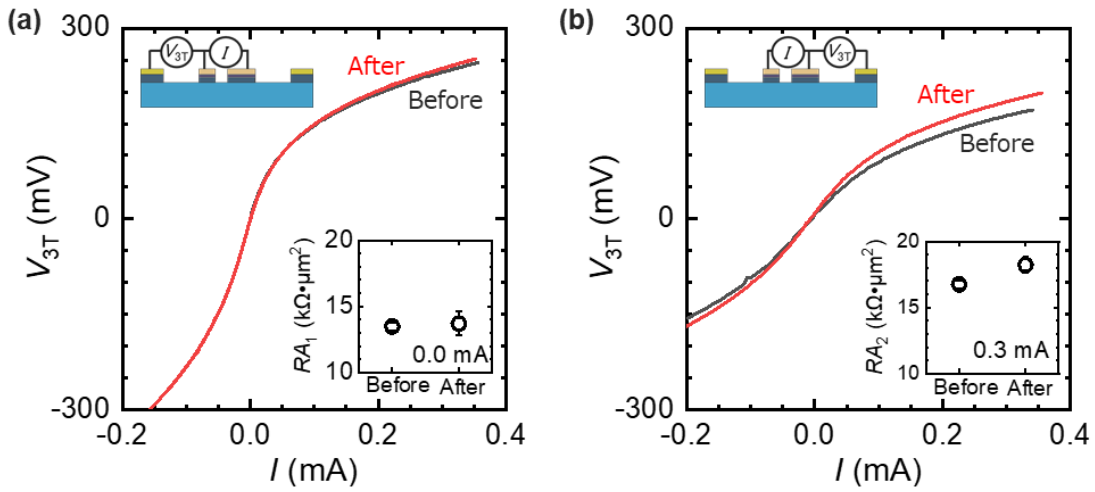

Figure 2.7: Voltage drop the ferromagnetic electrodes, V_{3T}.

I-V curves measured at **(a)** F1 and **(b)** F2. Black (red) solid line shows the measured $I - V_{3T}$ curves before(after) annealing at 300°C. This fiture is quoted from [55].

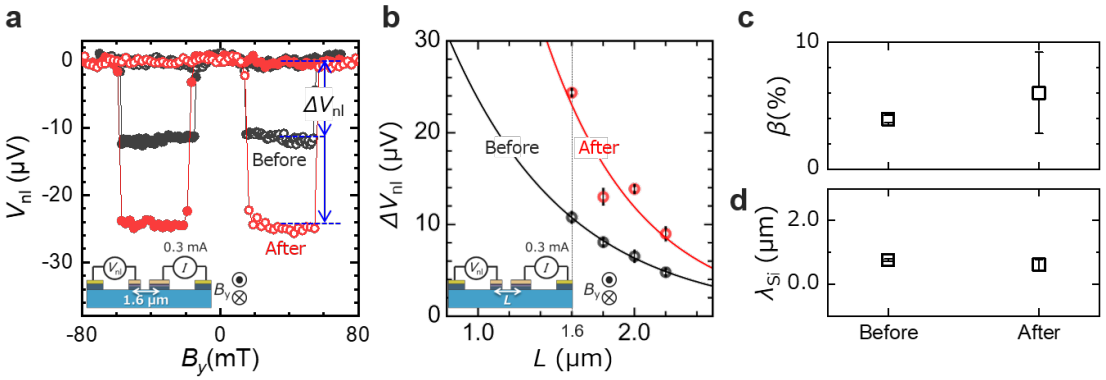

Figure 2.8: Spin signals detected by non-local four terminals (NL4T) method before/after annealing at 300°C and the results of the analysis.

(a) Result of NL4T measurement under a bias current of 0.3 mA. The black and red plots show the measured V_{nl} before and after annealing at 300°C, respectively. The filled and open dots represent the V_{nl} in down and up sweep of B_y. The spin signal ΔV_{nl} got twice after the annealing. The inset shows the configuration of NL4T. **(b)** The channel length L dependence of V_{nl}. The open circles represent the value of ΔV_{nl}, and the solid lines are the fitting lines by Eq. 2.26. The fitting lines nicely reproduced the experiments. **(c)** Obtained spin polarization β by the fitting, which increased from 4 to 6 after the annealing. **(d)** Obtained spin diffusion length f λ_{N} by the fitting, which remains after the annealing. The values were 0.7 and 0.6 μm before and after the annealing, respectively. This figure is quoted from [55].

length, λ_{N}, were estimated by fitting with Eq.(2.26). The experimentally obtained values of RA_1, RA_2 shown in Fig. 2.7 were used for the analysis. The fitting, shown by the black and red lines, yields $\beta = 4.0 \pm 0.3\%$ and $\lambda_{\mathrm{Si}} = \lambda_{\mathrm{Si}} = 0.76 \pm 0.03\,\mu\mathrm{m}$ before annealing and $\beta = 6.0 \pm 3.1\%$ and $\lambda_{\mathrm{Si}} = 0.61 \pm 0.17\,\mu\mathrm{m}$ after annealing, respectively, which are summarized in Figs. 2.8c and 2.8d. These values are consistent with the previous study [34]. Although the error bar of β after annealing was relatively large because of an outlier for $L = 1.8\,\mu\mathrm{m}$, the enhancement of β was confirmed for several sets of devices. Therefore, the enhancement in spin signal is attributable to spin polarization.

2.4.2 Hanle Effect

The Hanle effect measurement was carried out to investigate the spin lifetime τ, in the Si channel. Whereas the current-voltage configuration was the same as that of the NL-4T method, the applied magnetic field was along the z-direction, as shown in the inset of Fig. 2.9a. Three samples with different L (1.8, 2.0, and 2.2 µm) were measured. Figure 2.9a shows the typical Hanle signals before (black dots) and after (red dots) the thermal annealing. I showed a difference in the non-local voltages, $V_{\mathrm{nl}}^{\mathrm{P}} - V_{\mathrm{nl}}^{\mathrm{AP}}$, between the parallel and antiparallel magnetic configurations. The magnitude of $V_{\mathrm{nl}}^{\mathrm{P}} - V_{\mathrm{nl}}^{\mathrm{AP}}$ is confirmed to be consistent with ΔV_{nl} in Fig. 2.8b and to be enhanced by the thermal annealing. The solid lines show the curve fitting of the one-dimensional model by using the following equation [16]:

$$\frac{V_{\mathrm{nl}}^{\mathrm{P}}(B_z) - V_{\mathrm{nl}}^{\mathrm{AP}(B_z)}}{I} = \pm S_0 \int_0^\infty \sqrt{\frac{1}{4\pi D t}} \cos(\omega t) \exp\left(-\frac{t}{\tau}\right) \exp\left(-\frac{L^2}{4Dt}\right) dt, \tag{2.27}$$

where B_z is the magnetic flux density along the z-direction, S_0 is the constant that determines the signal amplitude, $\omega = g\mu_B B_z/\hbar$ is the Larmor frequency, $g = 2$ is the g factor for the electrons, μ_B is the Bohr magneton, and $\hbar$ is the Dirac constant. Here, the effect of the conductivity mismatch is included in S_0. Therefore, the analyses by the Eqs. (2.26) and (2.27) are consistent. The fitting curves obtained by using Eq. (2.27) well reproduced the experimental results. Figures 2.9b and 2.9c show τ and $\lambda_{\mathrm{N}} = \sqrt{D\tau}$ (here Si is used for the material N), respectively, obtained from the fitting of Eq. (2.27). These obtained values are consistent with previous studies [38,53,56], and no significant changes in τ and λ_{N} were observed after the annealing.

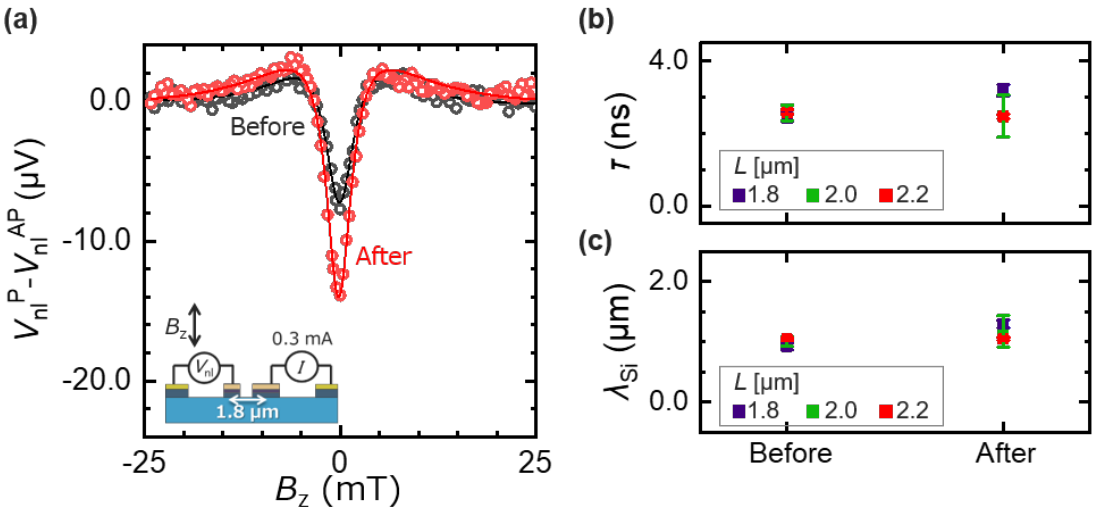

Figure 2.9: Hanle signals and results of the analysis

(a) Hanle spin precession signals, i.e., the difference in V_{nl} between parallel and antiparallel configurations as a function of B_z before and after thermal annealing. The circles represent the measured values, and the solid lines represent the curves fitted by Eq. (2). **(b, c)** Comparison of **(b)** the spin lifetime, τ, and **(c)**λ_{Si} before and after annealing estimated from the curve fitting of Eq. (2) for several devices with different L. This figure is quoted from [55].

2.4.3 The Origin of the Enhancement of the Spin Signals

I consider the origin of the enhancement of β. The spin polarization is related to the contribution of the coherent tunneling. If the texture of the Fe/Co/MgO layer was improved, the contribution of the Δ_1 state to the total spin current increased. To confirm the change in the layer, X-ray diffraction (XRD) measurements were carried out using a plane sample with the same structure as the ferromagnetic electrodes consisting of Au(3 nm)/Fe(13 nm)/Co(0.6 nm)/MgO(0.8 nm) grown on the SOI substrate in the same way as the FM electrodes. A piece of the plane sample was annealed at the same condition (300°C for 1 hour in a vacuum). The XRD spectrum was compared in Fig. 2.10. The gray and the red plots represent the XRD spectra of the plane samples before and after annealing, respectively. Two peaks from MgO and Fe layers were detected in both samples. Clear enhancement of the peak heights was observed after the annealing, which supports the assumption that the annealing improves the texture of the Fe/Co/MgO layer, which enhances the contribution of the coherent tunneling via the Δ_1 state. Thus, I confirmed that thermal annealing enhances the spin polarization of the metal/Si interface resulting in the enhancement of the spin signal by a factor of 2.

2.4.4 Thermal Tolerance of Si-based Spin Devices

Additional annealing at 350°C was also carried out. Any spin signals, however, were not observed after the annealing. The interface resistance was drastically decreased and almost linear I-$V_{3\mathrm{T}}$ characteristics were observed, whilst the thermal tolerance of the Si-based lateral spin valves was reported as ca. 400°C[51,52,57]. The microscopic images of sample A before and after the annealing are shown in Fig. 2.11a and Fig. 2.11b, respectively. At the NM electrodes, a smooth gold surface was confirmed before annealing, but a patchy pattern in gray and blue appeared after the annealing. In contrast, no significant changes were observed on the surface of FM electrodes. To understand the deviation in the thermal tolerance from that of the previous studies and clarify the mechanism of the degradation, I performed nanoanalysis using transmission electron microscopy (TEM) and energy-dispersive x-ray spectroscopy (EDS). The cross-section of the FM electrodes indicated by the purple square in Fig. 2.11c. While Au was not used in FM electrodes (Fig. 2.11d), Au atoms were detected from the FM/Si interface as shown in blue, which was attributable to the migration from the NM electrode (Fig. 2.11e). However, NM electrodes were placed 7 µm away from the FM electrodes, and Au dif-

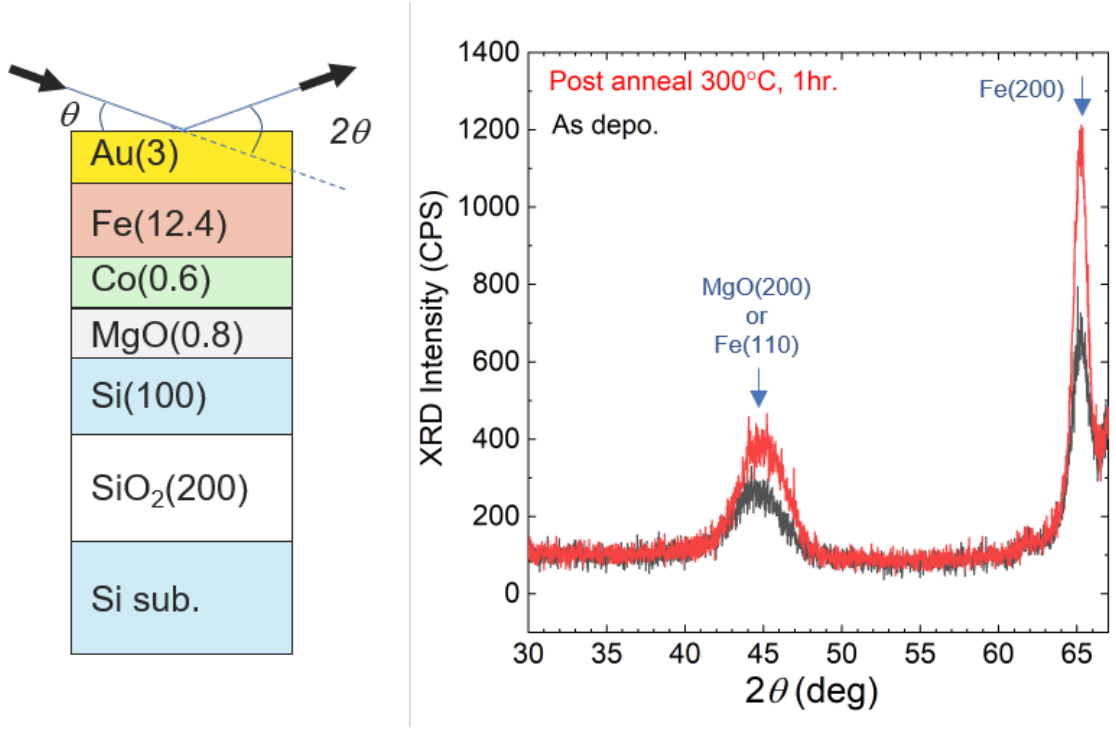

Figure 2.10: Comparison of the XRD spectra before and after annealing at 300°C.

The gray (red) solid line shows the XRD spectrum of the sample before(after) annealing at 300°C. The intensity of Fe (200) spectrum was enhanced by the annealing.

fusion in the Si channel was improbable because the annealing was carried out at lower temperature than the melting points of Au nor Si. The NM electrodes consisting of Au/Ta/Al (the design is shown in Fig. 2.11f) were examined by using EDS as shown in Figs. 2.11g and 2.11h. The Au atoms diffused in the Al layer and reached the Al/Si interface. TEM observation shown in Figs. 2.12b disclosed the path of Au diffusion. At the area indicated in Fig. 2.12a, intermixing of Si channels and Au atoms was recognized beneath the NM electrodes (Fig. 2.12b) and limited to only 200 nm apart from the NM electrode. Figures. 2.12c and 2.12d show atomic-resolution TEM image and the Fourier transform obtained at a part of the [1 1 0] surface of the Si channel ca. 0.4 µm away from the NM electrodes. The Fourier transform shows hexagonal spot patterns, which is evident in the clear periodicity of the diamond structure, indicating no significant structural damage to the Si channel itself. On the contrary, the Au diffusing area along the AlN/Si interface shows a halo feature (Fig. 2.12e), indicating significant damage to the crystal structure. Since the Au-Si system forms a eutectic with a considerably low solubility limit of Au atoms in the Si phase, segregation of Au atoms was unexpected if the Si channel dominantly contributes to the Au diffusion. Because no Au particles were confirmed near the bottom side of the Si layer, the Si channel is not a probable diffusion path for the Au atoms.

The Al-Si binary system forms eutectic, but the temperature of the eutectic point is above 570°C, indicating that the Al-Si liquid phase is not formed at the Al/Si interface during the annealing process. In contrast, the temperature of the eutectic point of the Au-Si system is approximately 350°C. Therefore, a possible mechanism of Au atom diffusion is as follows: starting from the designed structure (Fig. 2.12f), the intermixing of Al and Au atoms takes place below 300°C (Fig. 2.12g), which is confirmed by EDS (Figs. 2.11g and 2.11h). The interdiffusion length l of Au and Al atoms, estimated from $l = 5.56 \times 10^{-10} t$ m[59] at 350°C, is 2 µm after $t = 1$ hour. Therefore, Au atoms easily diffuse whole the Al layer, which is only 40 nm in thickness, and reach the Si channel. The melting point of Au_8Si_2 is approximately 350°C, so Au-Si and/or Au-Al-Si liquid phases are formed at the Au-Si interface (Fig. 2.12h). Because Au_8Si_2 is a eutectic point, more Au and Si atoms rapidly increase the melting point, so most of the Si channel is not involved in the reaction. The Au-Si and/or Au-Al-Si liquid phases diffuse mainly along with the AlN/Si interface (Fig. 2.12i) due to the strong tensile strain[22], and the interface is more susceptible to break than the other areas. Finally, Au reaches the FM electrodes and invades the MgO tunneling barrier. To confirm the mechanism,

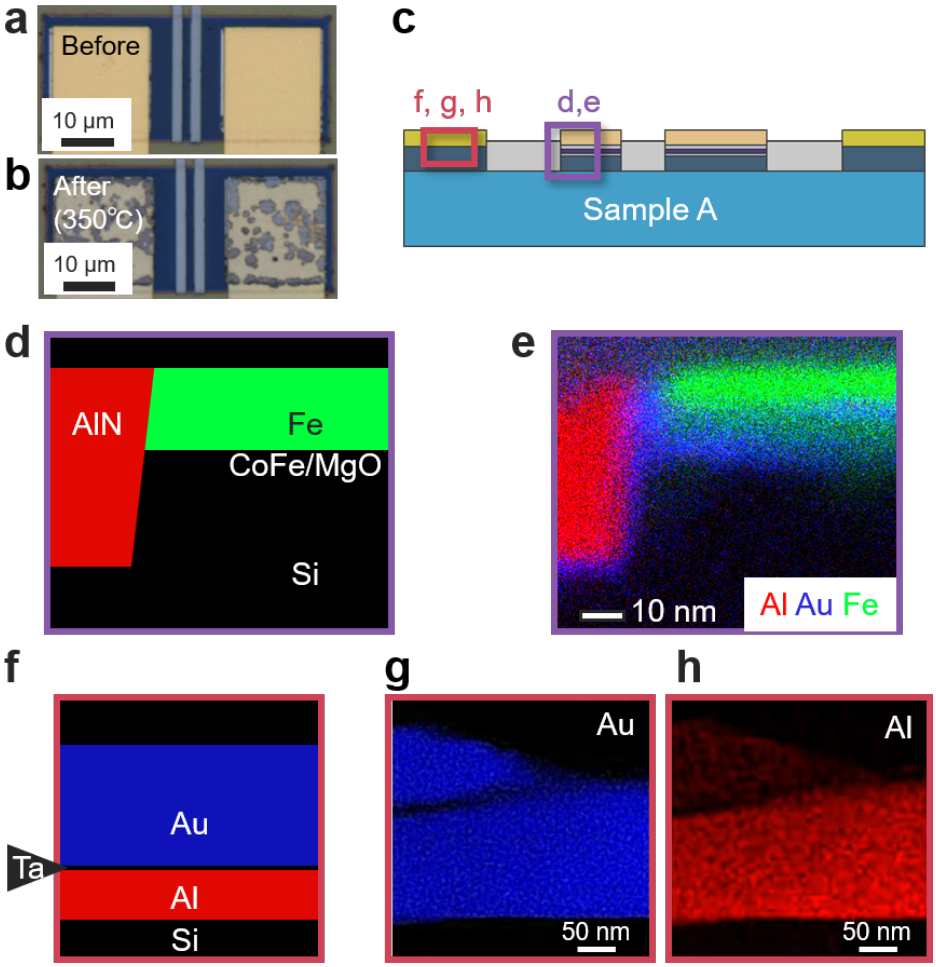

Figure 2.11: Microscopic image of sample A afeter annealing at 350°C.

(a, b) Optical microscopic image **(a)** before and **(b)** after annealing at 350°C. **(c)** A schematic cross-section of sample A. The areas of EDS observations are roughly indicated by purple and red squares. **(d)** A designed structure and **(e)** an elemental mapping image near the FM electrode indicated by the purple rectangle in **(c)**, where Au, Al and Fe are shown in blue, red and green, respectively. **(f)** Designed structure and elemental mapping images of **(g)** Au and **(h)** Al near the NM electrode indicated by the red rectangle in **(c)**. This figure is quoted from [58].

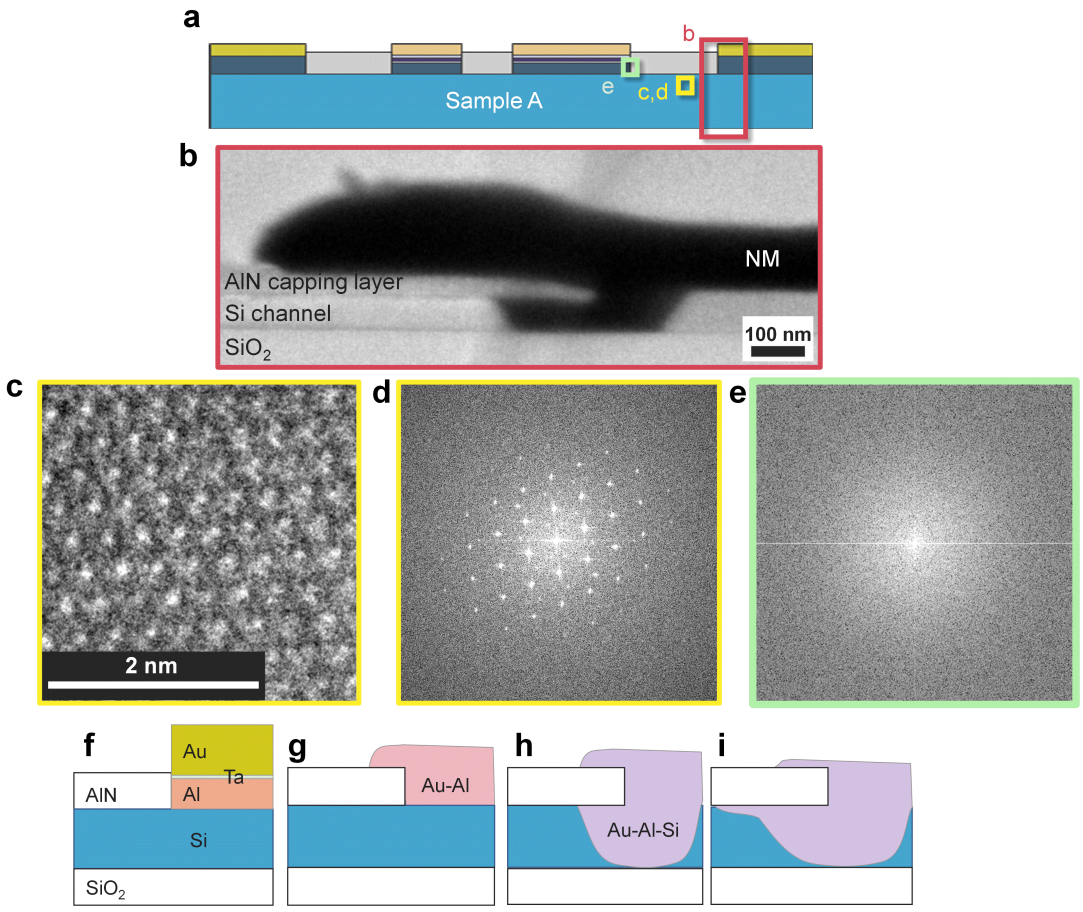

Figure 2.12: Crystallographic analyses of the Si channel after annealing and a possible degradation mechanism by annealing

(a) A schematic cross-section of sample A. The areas of TEM observations are roughly indicated by red and yellow squares. **(b)** A cross-sectional TEM image of the NM electrode obtained at the red square shown in **(a)**. **(c)** An atomic-resolution TEM image obtained at the Si channel indicated by the yellow rectangle in **(a)** and **(d)** the Fourier transform of the area. **(e)** A Fourier transform of the area of Au diffusing along AlN/Si interface. **(f-i)** Schematic images of the possible mechanism of diffusion of the Au atoms during annealing. **(f)** the fabricated structure. **(g)** Au-Al intermetallics were formed, and Au reached Si. **(h)** The intermetal of Au-Al-Si was formed, including the liquid phase. **(i)** The liquid phase diffused through the interface of AlN/Si. This figure is quoted from [58].

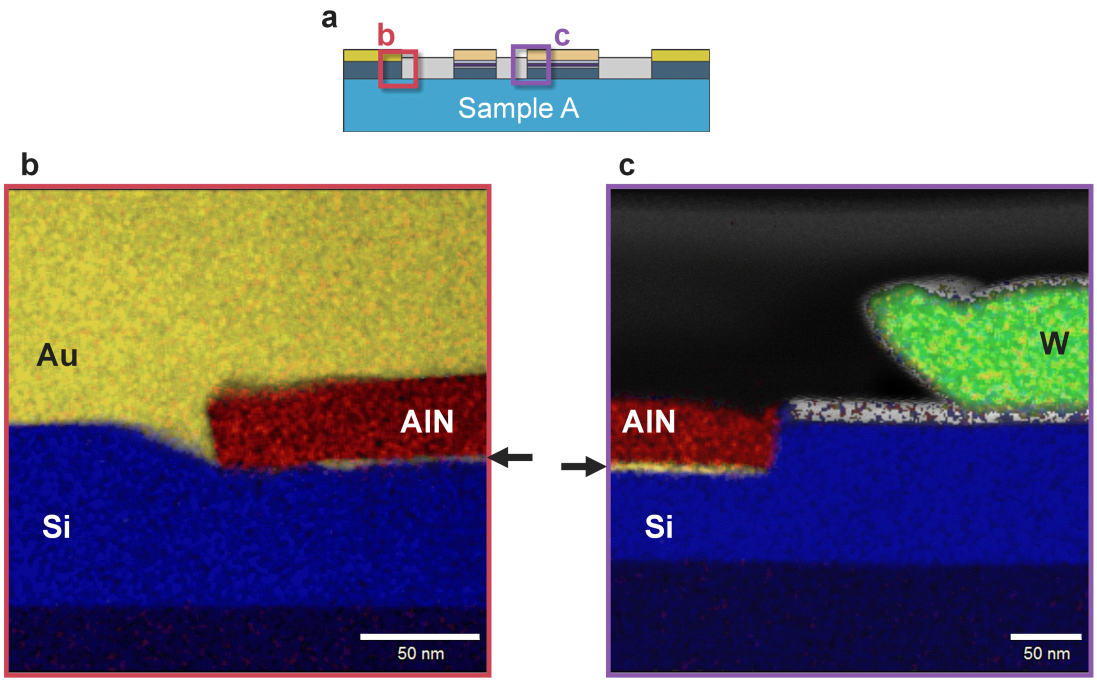

Figure 2.13: Elemental mapping images of other parts of sample A.

(a) A schematic cross-section of sample A. The examined ares are indicated by the red **(b)** and the purple **(c)** rectangles. **(b)** The overlay of the elemental mapping around N1. The blue, yellow, and red area indicate Si, Au, and N atoms near the NM electrode, respectively. Au was detected from the AlN/Si interface, which is indicated by the arrow. **(c)** The overlay of the elemental mapping around F2. The blue, yellow, red, and green areas indicate Si, Au, N, and W atoms near the FM electrode, respectively. Au was detected from the AlN/Si interface, which is indicated by the arrow. This figure is quoted from [58].

elemental mapping images of other parts at the AlN/Si interface of sample A were also obtained around the NM and FM electrodes as shown in Fig. 2.13. Au was detected at the AlN/Si interface even between the F1 and F2, i.e., a part of the spin transport channel as indicated by the arrows in Figs. 2.13b and 2.13c. Therefore, not only FM contacts but also the spin transport channel was damaged by the Au atoms.

A control experiment was carried out to verify the hypothesis of the thermal degradation mechanism. To avoid the interdiffusion of Al and Au, we excluded Al from the NM electrodes and employed a thick Ta layer for sample B: Au(150 nm)/Ta(40 nm), since Ta is often applied to a barrier metal for Si against conductive metals such as Cu: Ta layer is maintained even after annealing at 630°C, which is high enough for any thermal treatments applied to electronic devices [60]. Thermal annealing at 300°C, 350°C, and 400°C was carried out. The optical microscopic images showed no salient changes on the surface of the Au/Ta electrode even after the annealing at 400°C (see Figs. 2.14a and 2.14b), on the contrary to the Au/Ta/Al structure in sample A. Cross-sectional elemental mapping images were also obtained around the parts indicated by the purple and red rectangles shown in Fig. 2.14c. No signals from Au atoms were detected at the AlN/Si interface or around FM even after annealing at 400°C (see Fig. 2.14d). Furthermore, the NM electrodes clearly maintain the Au/Ta bilayer structure (Figs. 2.14e and 2.14f). These results are obviously different from those of sample A, which directly supports the assumed mechanism of the thermal degradation.

To confirm the thermal tolerance of the FM/Si interfaces, NL4T measurement was carried out at RT. The results were shown in Fig. 2.15. Similar to sample A, the magnitude of the spin signal increased from 9 µV to 18 µV after annealing at 300°C. In contrast to sample A, the spin signal did not decrease after annealing at 350°C, and clear spin signals were detected even after annealing at 400°C (see Fig. 2.15a). To corroborate the tolerance of the spin diffusion length, Hanle signals were also measured in the NL4T method using sample B before and after annealing at 300°C and 350°C as shown in Fig. 2.15b. The difference in V_{nl} between the parallel and antiparallel magnetic configurations, $V_{\mathrm{nl}}^{\mathrm{P}} - V_{\mathrm{nl}}^{\mathrm{P}}$ was employed for the analysis to eliminate the spurious effects. The theoretical curve nicely reproduced the results of Hanle measurement, providing the spin diffusion length before and after annealing at 300°C and 350°C being equal to 1.6 ± 0.1 µm, 1.7 ± 0.1 µm and 1.8 ± 0.1 µm, respectively. Therefore, no significant changes in spin diffusion length in the Si channel were confirmed after annealing up to 350°C, as expected. After the annealing at 400°C, because of the small magnitude

of the spin signals, precise estimation of λ_N from the Hanle effect was difficult. A possible origin of the small spin signals is degradation in the FM electrode. Because after annealing at 400°C, the I-V curve of the FM electrodes apparently different (Fig. 2.15c), and current increased from that before annealing at 400°C. The inset of Fig. 2.15c shows the resistance area products RA normalized by the value before annealing. RA decreased slightly after annealing at 350°C and steeply to 0.85 after annealing at 400°C similar to the previous study [57]. According to the nonlinear I-V characteristics after annealing at 400°C, sample B is expected to degrade in a different mechanism from sample A reflecting an inherent tolerance of the Fe/Co/MgO electrode. Thus, I disclosed a mechanism of the thermal degradation of sample A and improved the tolerance up to 400°C.

2.5 Summary

In summary, I studied the effect of thermal annealing on the metal/Si interfaces in Si-based lateral spin valves. The magnitude of NL4T spin signals at room temperature was found to increase by a factor of 2 after the thermal annealing at 300°C in a vacuum for an hour because the spin polarization β increased, whilst the spin diffusion length and spin lifetime in the Si channel remains unchanged. Thus, FM/MgO/Si interface is attributable to the enhancement because they get a better texture, which was confirmed by XRD spectroscopy. The mechanism is similar to the case of the MTJ structure [31].

I also examined the degradation mechanism of the metal/Si interfaces in Si-based spin devices by thermal annealing: Au invades from the NM electrodes to the FM electrodes and breaks the MgO tunnel barriers. In the metal/Si interface of NM electrodes, Au diffuses in Al, forms alloys with Si around 350°C, the liquid phase mainly diffuses the AlN/Si interface and invaded the metal/Si interface of FM electrodes. By substituting Au/Ta with thick Ta for Au/Ta/Al with thin Ta, the thermal tolerance improved and I detected spin signal even after annealing at 400°C. The combination of Au/Ta and Fe/Co/MgO shows the thermal tolerance of 400°C, which is sufficiently high for the post-fabrication process of electronic devices. The thermally tolerant Si-based spin devices certified the compatibility of the spin devices with the electronics industry.

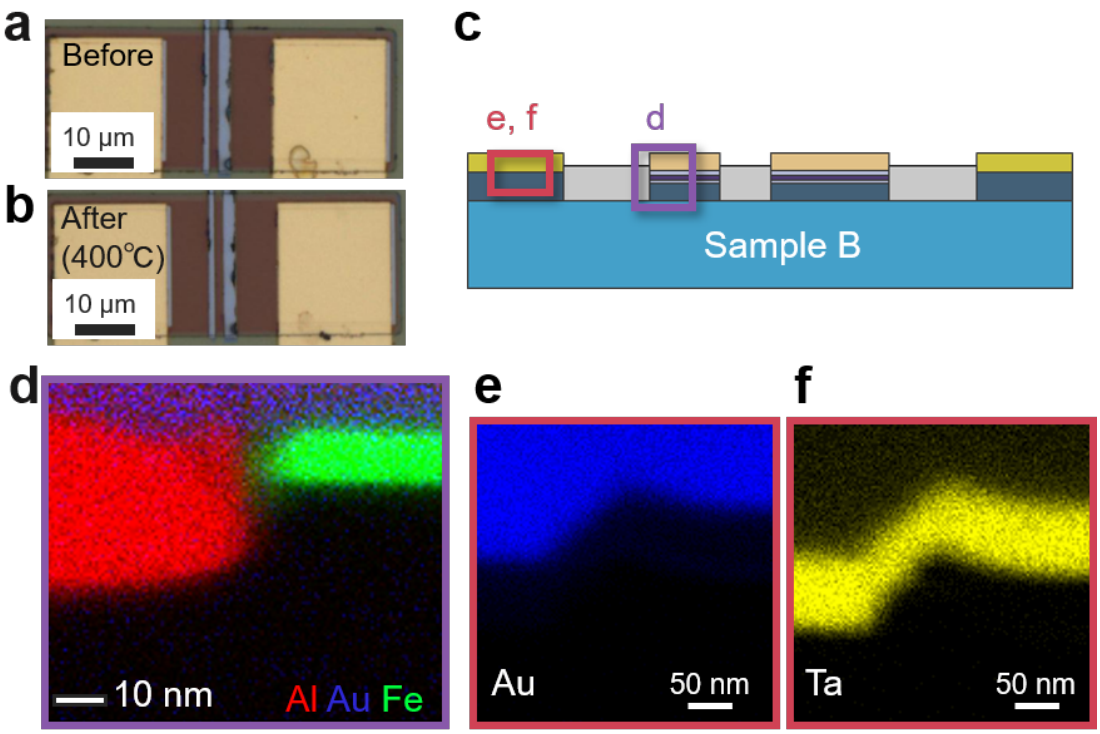

Figure 2.14: Microscopic image of Si-based spin device afeter annealing at 400°C.

(a,b) Optical microscopic image **(a)** before and **(b)** after annealing at 400°C. **(c)** A schematic cross-section of sample B. The areas of EDS observations are roughly indicated by purple and red squares. **(d)** Elemental mapping image near the FM electrode indicated by the purple rectangle in **(c)**. **(e, f)** Elemental mapping images of **(e)** Au and **(f)** Ta near the NM electrode indicated by the red rectangle in **(c)**. This figure is quoted from [58].

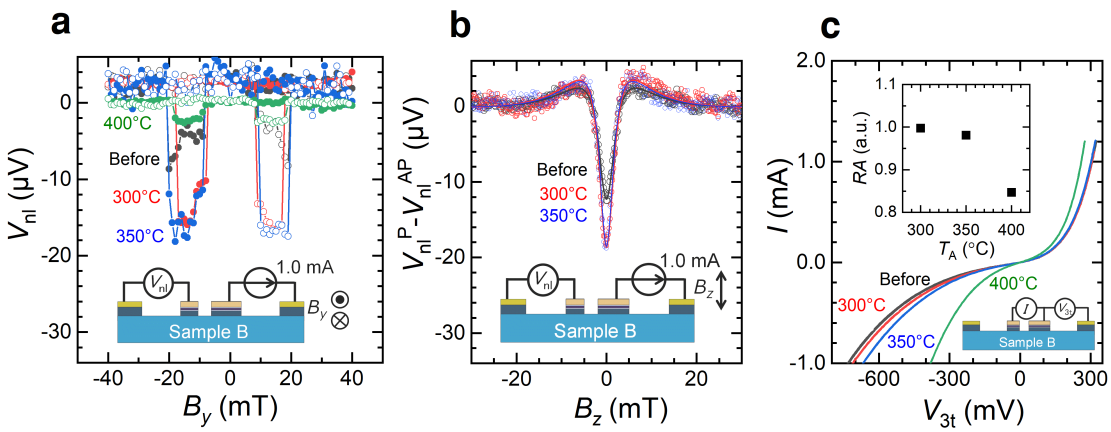

Figure 2.15: Results of the control experiments with sample B including NM electrodes of Au/Ta.

(a) The spin accumulation signals of sample B measured by the NL4T method. The black, the red, the blue and the green plots show V_{nl}s measaured before annealing, after annealing at 300°C, 350°C, and 400°C, respectively. The inset shows the result of the L3T measurement after annealing at 400°C, respectively. **(b)** Results of the Hanle measruements of sample B. The black, the red and the blue plots show V_{nl}s measaured before annealing, after annealing at 300°C and 350°C, respectively. **(c)** I-V characteristics of sample B. Black, red, blue, and green plots show the results measrued before annealing, after annealing at 300°C, 350°C, and 400°C, respectively. The inset shows the RA product normalized by the value before annealing measured at 1.0 mA. This figure is quoted from [58].

Chapter 3

Spin-dependent Seebeck Effect at Metal/Si Interfaces

In this chapter, I report the first demonstration, among all semiconductors, of the spin-dependent Seebeck effect and generation of a spin current using Joule heating, which allows making additional spin current in Si. The spin-dependent Seebeck effect is a spin caloritronic phenomenon at a ferromagnet/nonmagnet interface that makes a spin current by using a heat current at the interface. I establish a new method to separate spin signals originating from the spin-dependent Seebeck effect from that to the conventional electrical spin injection. From a theoretical model that includes a temperature gradient and an electric field, I estimated the thermal spin signal at the Fe/MgO/Si interface as 8 μV with a realistic temperature gradient of 200 mK/nm. The spin-dependent Seebeck effect is suggested as a new method to enhance the spin signal in a Si-based spin device.

Results presented in this chapter were published in the papers:

1. **Naoto Yamashita**, Yuichiro Ando, Hayato Koike, Shinji Miwa, Yoshishige Suzuki, and Masashi Shiraishi, "Thermally Generated Spin Signals in a Nondegenerate Silicon Spin Valve", *Physical Review Applied* **9**, 054002 (2018). Published by American Physical Society.

3.1 Introduction and Motivation

There are four methods to make spin current in a nonmagnetic material: electrical [61], dynamical [62], optical [63], and thermal methods [64]. Considering the application for integrated circuits, where the scalability of devices is indispensable, the electrical and the thermal methods are essential. To make spin current in Si, the electrical methods have been demonstrated and clarified the different mechanism in spin transport from a metallic material such as Cu [16,32], whilst the thermal method is yet to be demonstrated in any semiconductors including Si. The thermal method has a possibility to add spin current and enhance MR ratio in spin devices based on Si because the method enables to generate spin currents by using Joule heating brought by charge currents in semiconductor devices.

3.1.1 Spin Caloritronics

Coupling of spin current and heat current leads novel physical phenomena, with many attractive caloritronic effects [64–72] such as the spin Seebeck effect [67,68], the spin-dependent Seebeck effect [64,71,72], and the spin Pertier effect [65,69]. These effects have been limited to metals and insulators and have yet been extended to semiconductors.

One example of the spin caloritronic effects in a semiconductor is the Seebeck spin tunneling [73], where they claimed thermal spin accumulation by using the controversial three-terminal method. The spin signals are suspicious associated with the broad Hanle signals because it detected the spins accumulated at only the metal/Si interfaces [74–80]. The spin injection into Si by caloritronic effect has not been reported yet. Here, by using the spin-dependent Seebeck effect (SDSE), I attempt to make spin current in Si.

3.1.2 Spin Seebeck Effect and Spin-dependent Seebeck Effect

It should be noted that the spin-dependent Seebeck effect is different from the spin Seebeck effect although both spin caloritronic effects convert heat currents to spin currents, and the origins of both effects are the same: the different Seebeck coefficient, S, of each spins in the ferromagnet. Schematic images of these effects are shown in Fig. 3.1. The spin Seebeck effect occurs in a ferromagnetic material (see Fig. 3.1a). The spin-dependent Seebeck effect occurs at a ferromagnet/nonmagnet interface (see Fig. 3.1b). The spin-dependent Seebeck effect converts the heat current at the interface

into the spin current in the nonmagnetic material. In a metallic magnet, spin-up and spin-down conduction electrons have different Seebeck coefficients, as if two conductors with different S were inherently present in the magnet. When a temperature gradient is applied to the magnet, the difference in S makes a different amount of flows for each spin; the spin current can be extracted to the adjacent nonmagnet. The temperature gradient of the ferromagnet/nonmagnet interface drives the spin injection into the nonmagnet.

The proof of the concept of the SDSE was reported in 2010 [64]. They fabricated a lateral spin valve structure with Cu and NiFe and detected spin signals associated with Joule heating by measuring the 2nd harmonic component of the spin accumulation voltage signal using a lock-in amplifier [64]. The spin-dependent Seebeck coefficient – the magnitude of the voltage made by the temperature gradient – is $-3.8\,\mu\mathrm{V/K}$ for the NiFe alloy and expressed as the product of the spin polarization of the conductivity and the conventional Seebeck coefficient. Because the conductivity spin polarization of Fe is 0.4 [81], Fe/MgO/Si structure is also expected to show the SDSE.

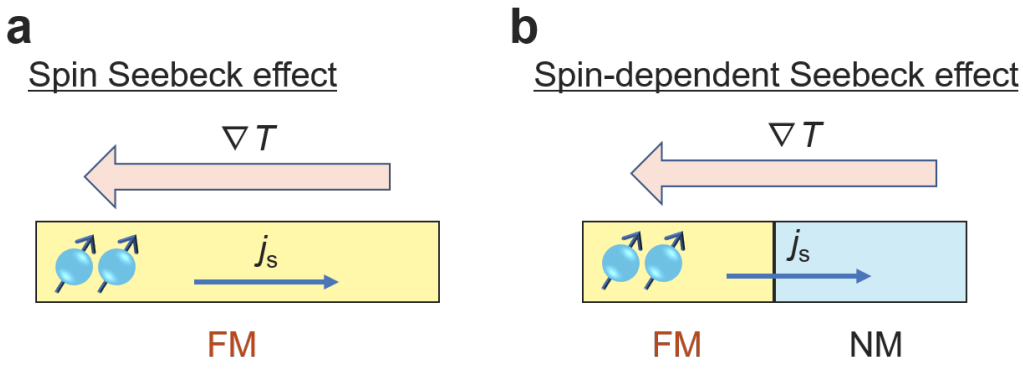

Figure 3.1: Conceptual images of spin caloritronic effects
The concepts of **(a)** the spin Seebeck effect and **(b)** the spin-dependent Seebeck effect.

3.2 Theory of Thermal Spin Signals

3.2.1 One-dimentional Model Including Spin-dependent Seebeck Effect

The magnitude of the spin current in Si and the spin signals in a Si-based spin device is generally described by using spin drift-diffusion equation [7,8]:

$$\nabla^2(n_\uparrow - n_\downarrow) + \frac{e\boldsymbol{E}}{k_\mathrm{B}T}\nabla(n_\uparrow - n_\downarrow) - \frac{(n_\uparrow - n_\downarrow)}{\lambda_\mathrm{N}^2} = 0, \tag{3.1}$$

where, $n_{\uparrow(\downarrow)}$ is the spin up(down) electron density, e is the elemental charge, $\boldsymbol{E}$ is the electric field in the Si channel, λ_N is the spin diffusion length of the Si channel, T is the absolute temperature, and k_B is the Boltzmann constant. The theoretical analysis of the SDSE requires another term: a heat current. I add the term of $S_s\nabla T$, where S_S is the spin Seebeck coefficient and ∇T is a temperature gradient, and solve the equations analytically with assuming one dimensional model of lateral spin valve as shown in Fig. 3.2 under the local-three terminal (L3T) configuration (to includes spindrift effect as same as spin MOSFETs). The temperature gradient at $x = 0, L$, and $0 < x < L$ are difined as $\nabla T_0, \nabla T_\mathrm{L}$ and ∇T_N, respecrively.

- F1 ($x_\mathrm{F} < 0$)

$$V_{1\uparrow} = -\frac{J}{\sigma_\mathrm{F1}}x_\mathrm{F} + V_1^- \frac{\sigma_{1\downarrow}}{\sigma_\mathrm{F1}} e^{\frac{x_\mathrm{F}}{\lambda_\mathrm{F1}}} + D, \tag{3.2}$$

$$V_{1\downarrow} = -\frac{J}{\sigma_\mathrm{F1}}x_\mathrm{F} + V_1^- \frac{\sigma_{1\uparrow}}{\sigma_\mathrm{F1}} e^{\frac{x_\mathrm{F}}{\lambda_\mathrm{F1}}} + D, \tag{3.3}$$

$$J_{1\uparrow} = \frac{\sigma_{\uparrow 1}}{\sigma_\mathrm{F1}}J - \frac{1}{R_\mathrm{F1}} e^{\frac{x_\mathrm{F}}{\lambda_\mathrm{F1}}} V_1^- - \sigma_{\uparrow 1}S_{\uparrow 1}\nabla T_0, \tag{3.4}$$

$$J_{1\downarrow} = \frac{\sigma_{\downarrow 1}}{\sigma_\mathrm{F1}}J + \frac{1}{R_\mathrm{F1}} e^{\frac{x_\mathrm{F}}{\lambda_\mathrm{F1}}} V_1^- - \sigma_{\downarrow 1}S_{\downarrow 1}\nabla T_0, \tag{3.5}$$

- F2 ($x_\mathrm{F} > L$)

$$V_{2\uparrow} = -\frac{J}{\sigma_\mathrm{F2}}(x_\mathrm{F} - L) - \frac{J}{\sigma_\mathrm{N}}L + V_2^+ \frac{\sigma_{2\downarrow}}{\sigma_\mathrm{F2}} e^{-\frac{x_\mathrm{F}-L}{\lambda_\mathrm{F2}}} - E, \tag{3.6}$$

$$V_{2\downarrow} = -\frac{J}{\sigma_\mathrm{F2}}(x_\mathrm{F} - L) - \frac{J}{\sigma_\mathrm{N}}L - V_2^+ \frac{\sigma_{2\uparrow}}{\sigma_\mathrm{F2}} e^{-\frac{x_\mathrm{F}-L}{\lambda_\mathrm{F2}}} - E, \tag{3.7}$$

$$J_{2\uparrow} = \frac{\sigma_{\uparrow 2}}{\sigma_\mathrm{F2}}J + \frac{1}{R_\mathrm{F2}} e^{-\frac{x_\mathrm{F}-L}{\lambda_\mathrm{F2}}} V_2^+ - \sigma_{\uparrow 2}S_{\uparrow 2}\nabla T_\mathrm{L}, \tag{3.8}$$

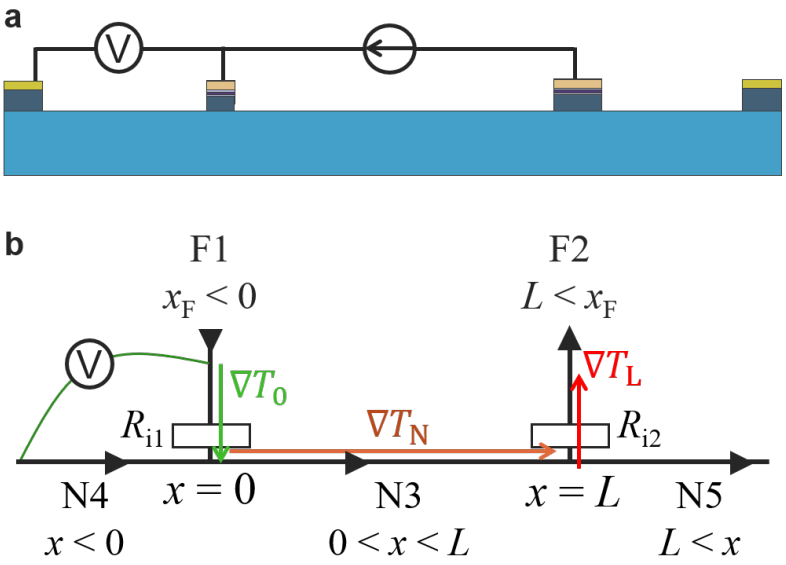

Figure 3.2: One-dimensional model of a lateral spin valve considering spin-dependent Seebeck effect

(a) The schematic side view of the local-three terminal measurement using a Si-based lateral spin valve. **(b)** One-dimentional model of the Si-based lateral spin valve.

$$J_{2\downarrow} = \frac{\sigma_{\downarrow 2}}{\sigma_{\mathrm{F2}}} J - \frac{1}{R_{\mathrm{F2}}} e^{-\frac{x_{\mathrm{F}}-L}{\lambda_{\mathrm{F2}}}} V_2^+ - \sigma_{\downarrow 2} S_{\downarrow 2} \nabla T_{\mathrm{L}}, \tag{3.9}$$

- N3 ($0 < x < L$)

$$V_{3\uparrow} = \frac{V_3^+}{2} e^{-\frac{x}{\lambda_{\mathrm{u}}}} + \frac{V_3^-}{2} e^{\frac{x-L}{\lambda_{\mathrm{d}}}} - \frac{J}{\sigma_{\mathrm{N}}} x, \tag{3.10}$$

$$V_{3\downarrow} = -\frac{V_3^+}{2} e^{-\frac{x}{\lambda_{\mathrm{u}}}} - \frac{V_3^-}{2} e^{\frac{x-L}{\lambda_{\mathrm{d}}}} - \frac{J}{\sigma_{\mathrm{N}}} x, \tag{3.11}$$

$$J_{3\uparrow} = \frac{1}{R_{\mathrm{u}}} e^{-\frac{x}{\lambda_{\mathrm{u}}}} V_3^+ - \frac{1}{R_{\mathrm{d}}} e^{-\frac{x}{\lambda_{\mathrm{d}}}} V_3^- + \frac{J}{2} - \frac{1}{2} \sigma_{\mathrm{N}} S_{\mathrm{N}} \nabla T_{\mathrm{N}}, \tag{3.12}$$

$$J_{3\uparrow} = -\frac{1}{R_{\mathrm{u}}} e^{-\frac{x}{\lambda_{\mathrm{u}}}} V_3^+ + \frac{1}{R_{\mathrm{d}}} e^{-\frac{x}{\lambda_{\mathrm{d}}}} V_3^- + \frac{J}{2} - \frac{1}{2} \sigma_{\mathrm{N}} S_{\mathrm{N}} \nabla T_{\mathrm{N}}, \tag{3.13}$$

- N4 ($x < 0$)

$$V_{4\uparrow} = \frac{V_4^-}{2} e^{\frac{x}{\lambda_{\mathrm{N}}}}, \tag{3.14}$$

$$V_{4\downarrow} = -\frac{V_4^-}{2} e^{\frac{x}{\lambda_{\mathrm{N}}}}, \tag{3.15}$$

$$J_{4\uparrow} = -\frac{1}{R_{\mathrm{N}}} e^{\frac{x}{\lambda_{\mathrm{N}}}} V_4^- - \frac{1}{2} \sigma_{\mathrm{N}} S_{\mathrm{N}} \nabla T_{\mathrm{N}}, \tag{3.16}$$

$$J_{4\uparrow} = \frac{1}{R_{\mathrm{N}}} e^{\frac{x}{\lambda_{\mathrm{N}}}} V_4^- - \frac{1}{2} \sigma_{\mathrm{N}} S_{\mathrm{N}} \nabla T_{\mathrm{N}}, \tag{3.17}$$

- N5 ($x > L$)

$$V_{5\uparrow} = -\frac{J}{\sigma_{\mathrm{N}}} L + \frac{V_5^+}{2} e^{-\frac{x-L}{\lambda_{\mathrm{N}}}}, \tag{3.18}$$

$$V_{5\downarrow} = -\frac{J}{\sigma_{\mathrm{N}}} L - \frac{V_5^+}{2} e^{-\frac{x-L}{\lambda_{\mathrm{N}}}}, \tag{3.19}$$

$$J_{5\uparrow} = \frac{1}{R_{\mathrm{N}}} e^{-\frac{x-L}{\lambda_{\mathrm{N}}}} V_5^+ - \frac{1}{2} \sigma_{\mathrm{N}} S_{\mathrm{N}} \nabla T_{\mathrm{N}}, \tag{3.20}$$

$$J_{5\uparrow} = -\frac{1}{R_{\mathrm{N}}} e^{-\frac{x-L}{\lambda_{\mathrm{N}}}} V_5^+ - \frac{1}{2} \sigma_{\mathrm{N}} S_{\mathrm{N}} \nabla T_{\mathrm{N}}, \tag{3.21}$$

where, $R_{\mathrm{F1(2)}} = \left(\frac{1}{\sigma_{\mathrm{F1(2)}\uparrow}} + \frac{1}{\sigma_{\mathrm{F1(2)}\downarrow}} \right) \lambda_{\mathrm{F}}$ and $R_{\mathrm{N}} = 2\lambda_{\mathrm{N}}/\sigma_{\mathrm{N}}$. The spin-dependent conductivities are described with the spin polarizations of F1(α_{F1}) and F2(α_{F2}) as $\sigma_{\mathrm{F1}\uparrow(\downarrow)} = \frac{1+(-)\alpha_{\mathrm{F1}}}{2} \sigma_{\mathrm{F1}}$ and $\sigma_{\mathrm{F2}\uparrow(\downarrow)} = \frac{1+(-)\alpha_{\mathrm{F2}}}{2} \sigma_{\mathrm{F2}}$, respectively. λ_{FM} is the spin diffusion length of the FM material, L is the center-to-center distance between F1 and F2, σ_{N} is the conductivity of the channel, $\sigma_{\mathrm{F1(2)}}$ is the conductivity

of the FM materials of F1(2), and J is the current density. $V_1^-, V_2^+, V_3^\pm, V_4^-$, and V_5^+ are constant values. The boundary conditions of the spin-dependent voltages and the currents at $x = x_\mathrm{F} = 0$ and $x = x_\mathrm{F} = L$ are given by Kirchhoff's laws as follows:

- $x = 0$

$$V_{1\uparrow} - R_{\mathrm{i}1\uparrow} J^0_{1\uparrow} = V_{3\uparrow} = V_{4\uparrow}, \tag{3.22}$$

$$V_{1\downarrow} - R_{\mathrm{i}1\downarrow} J^0_{1\downarrow} = V_{3\downarrow} = V_{4\downarrow}, \tag{3.23}$$

$$J^0_{1\uparrow} = J_{1\uparrow} = J_{3\uparrow} - J_{4\uparrow}, \tag{3.24}$$

$$J^0_{1\downarrow} = J_{1\downarrow} = J_{3\downarrow} - J_{4\downarrow}, \tag{3.25}$$

- $x = L$

$$V_{2\uparrow} + R_{\mathrm{i}2\uparrow} J^L_{2\uparrow} = V_{3\uparrow} = V_{5\uparrow}, \tag{3.26}$$

$$V_{2\downarrow} + R_{\mathrm{i}2\downarrow} J^L_{2\downarrow} = V_{3\downarrow} = V_{5\downarrow}, \tag{3.27}$$

$$J^L_{2\uparrow} = J_{2\uparrow} = J_{3\uparrow} - J_{5\uparrow}, \tag{3.28}$$

$$J^L_{2\downarrow} = J_{2\downarrow} = J_{3\downarrow} - J_{5\downarrow}, \tag{3.29}$$

By solving these equations analytically, I obtain the expression of the spin signal, V_S, as expressed as:

$$V_\mathrm{S} = D^\mathrm{P} - D^\mathrm{AP} = \left[\frac{\eta_\mathrm{d} \left(\frac{1}{R_\mathrm{d}} + \frac{1}{R_\mathrm{u}} \right) \left\{ \frac{1}{2} \alpha_{\mathrm{F}1} \left(R_{\mathrm{F}1} + R_{\mathrm{i}1} \right) - \frac{\left(\sigma_{\uparrow 1} R_{\mathrm{i}1\uparrow} - \sigma_{\downarrow 1} R_{\mathrm{i}1\downarrow} \right)}{\sigma_{\mathrm{F}1}} \right\}}{-\left(Q_\mathrm{d} + 1 \right) \left(Q_\mathrm{u} + 1 \right) + \left(U_\mathrm{u} - 1 \right) \left(U_\mathrm{d} - 1 \right) \eta_\mathrm{u} \eta_\mathrm{d}} \right] \times \left\{ \left(R_{\mathrm{F}2} \alpha_{\mathrm{F}2} - R_{\mathrm{i}2\uparrow} + R_{\mathrm{i}2\downarrow} \right) J - R_{\mathrm{F}2} \left(\sigma_{\uparrow 2} S_{\uparrow 2} - \sigma_{\downarrow 2} S_{\downarrow 2} \right) \nabla T_\mathrm{L} \right\}, \tag{3.30}$$

where, $\eta_\xi = e^{-\frac{L}{\lambda_\xi}}$ $(\xi = \mathrm{d}, \mathrm{u}, \mathrm{or\,N})$, $Q_{\mathrm{d(u)}} = \left(R_{\mathrm{F}1(2)} + R_{\mathrm{i}1(2)\uparrow} + R_{\mathrm{F}1(2)\downarrow} \right) \left(\frac{R_\mathrm{N} + R_{\mathrm{d(u)}}}{R_\mathrm{N} R_{\mathrm{d(u)}}} \right)$, and $U_{\mathrm{d(u)}} = \left(R_{\mathrm{F}1(2)} + R_{\mathrm{i}1(2)\uparrow} + R_{\mathrm{F}1(2)\downarrow} \right) \left(\frac{R_\mathrm{N} - R_{\mathrm{d(u)}}}{R_\mathrm{N} R_{\mathrm{d(u)}}} \right)$. D^P and D^AP are the voltages at the parallel (P) and antiparallel (AP) configuration of the spins, respectively, which are generated by the spin accumulation at $x = 0$. The interface resistances depending on the spin are described as $R_{\mathrm{i}1\uparrow(\downarrow)} = \frac{2}{1-(+)\beta_1} R_{\mathrm{i}1}$ and

$R_{\mathrm{i}2\uparrow(\downarrow)} = \frac{2}{1-(+)\beta_2} R_{\mathrm{i}2}$ by using the spin polarization of each interface β_1 and β_2. The spin signal V_{S} consists of the terms of the electrical spin signal that is proportional to J and the thermal spin signal that is proportional to ∇T_{L}. I use the subscript of "S" of V_{S} to represent the voltage is the spin signal voltage – the difference of the measured voltage at the P and AP states.

The thermal spin signal caused by spin-dependent Seebeck effect V^{therm} is expressed as:

$$V_{\mathrm{S}}^{\mathrm{therm}} = \left[\frac{\eta_{\mathrm{d}} \left(\frac{1}{R_{\mathrm{d}}} + \frac{1}{R_{\mathrm{u}}} \right) \left\{ \frac{1}{2} \alpha_{\mathrm{F}1} \left(R_{\mathrm{F}1} + R_{\mathrm{i}1} \right) - \frac{\left(\sigma_{\uparrow 1} R_{\mathrm{i}1\uparrow} - \sigma_{\downarrow 1} R_{\mathrm{i}1\downarrow} \right)}{\sigma_{\mathrm{F}1}} \right\}}{-\left(Q_{\mathrm{d}} + 1 \right) \left(Q_{\mathrm{u}} + 1 \right) + \left(U_{\mathrm{u}} - 1 \right) \left(U_{\mathrm{d}} - 1 \right) \eta_{\mathrm{u}} \eta_{\mathrm{d}}} \right] \times \left\{ -R_{\mathrm{F}2} \left(\sigma_{\uparrow 2} S_{\uparrow 2} - \sigma_{\downarrow 2} S_{\downarrow 2} \right) \nabla T_{\mathrm{L}} \right\}. \tag{3.31}$$

Using the values from the literature, I set $\alpha_1 (= \alpha_2) = 0.4$[81], $S = 15$ μV/K[82], and $\lambda_{\mathrm{F}} = 9$ nm[83] for Fe. The spin Seebeck coefficient, which is defined as $S_{\mathrm{S}} = S_{\uparrow} - S_{\downarrow}$ is theoretically expressed as $S_{\mathrm{S}} = \alpha S$[64,84]. The value for Fe is calculated as 6 μV/K. The conductiviteis of Fe and Si are measrued to be $\sigma_{\mathrm{F}} = 8.3 \times 10^6$ S/m and $\sigma_{\mathrm{N}} = 2.21 \times 10^3$ S/m, and the interface RA is measured to be $R_{\mathrm{i}1} = 2.56 \times 10^{-9}$ Ωm^2, and $R_{\mathrm{i}2} = 4.66 \times 10^{-9}$ Ωm^2 (the structure of the dedicated sample is described later). In the calculation, other parameters including the thermal gradient ∇T_{L} are assumed to be as same as those of the Si spin device. The calculated thermal spin signals are shown in Fig. 3.3. The horizontal and the vertical axes indicate typical properties of the ferromagnetic metals: the spin Seebeck coefficient and the spin polarization. The density of states at the Fermi level in the FM defines the spin polarization of the conductivity α_1 and α_2; their energy derivative defines S_{S}. The thermal spin signal in Si depends on these properties and a larger S_{S} provides a larger $V_{\mathrm{S}}^{\mathrm{therm}}$ as shown in Fig. 3.3. Thus, a FM with large α, such as CoFeAl[71] generates a large $V_{\mathrm{S}}^{\mathrm{therm}}$.

Figure 3.4 shows the calculated thermal spin signal depending on the properties of the nonmagnetic channel: σ_{N} and λ_{N}. The thermal spin signal depends on these parameters because the spin current generated by the SDSE propagates in the nonmagnetic channel. The optimum values of σ_{N} arises also in the case of the thermal spin signals similar to that of the electrical spin signal. The conductance mismatch issue appears[64], which makes the peak in σ_{N} same as the case of the electrical spin injection to semiconductors[85]. It is notable that material with metal-like conductivity (the order of 10^6 S/m) generates much smaller thermal spin signals than a lower conductivity (the order of 10^3 S/m). I compared Cu, the material used in the previous studies[64,71], and Si, the target of this study, and

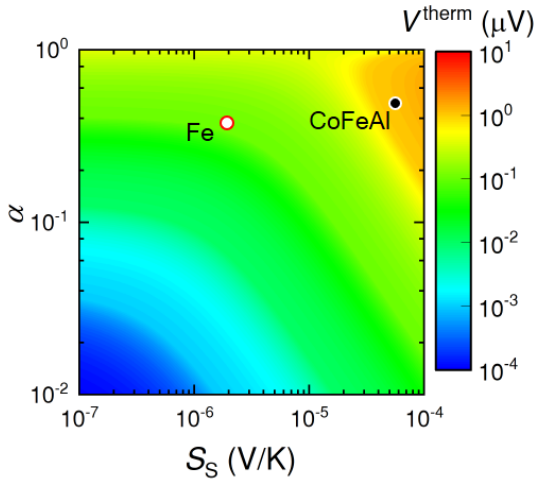

Figure 3.3: The dependence on the ferromagnetic materials of the thermal spin signal.

found Si provides 400 times larger spin signal than Cu (97 nV for Si and 0.2 nV for Cu) thanks to its low conductivity and large spin diffusion length (see Fig. 3.4).

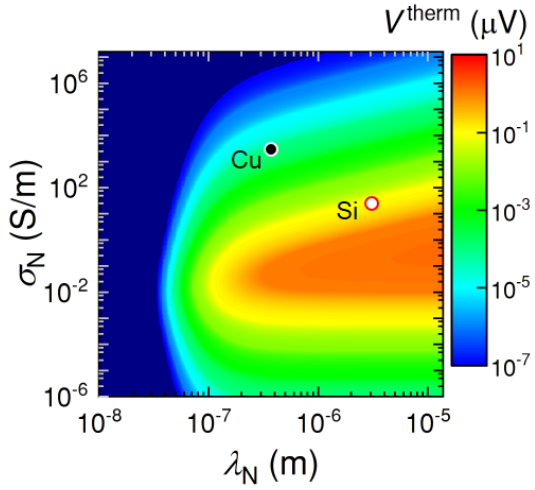

Figure 3.4: The dependence on the nonmagnetic materials of the thermal spin signal.

3.3 Experimental Details

To demonstrate the SDSE in Si-based spin device, I establish a new way to discriminate the thermally generated spin signal, i.e., the thermal spin signal, from spurious signals such as electrically generated spin signals, i.e., the electrical spin signal. In the previous study, a simple lock-in technique enabled to extract thermal spin signals that assuming the electrical spin signal linearly depends on the electrical current [64]; however, the technique is unsuitable for Si-based spin devices because of the nonlinearity in the current-voltage (I-V) curve, which must appear in the device including a MgO tunneling barrier. I establish a new experimental technique to investigate the magnitude of the thermal spin signal in a Si-based spin device. The establishment is also significant to solve the problem of nonlinearity in the bias voltage dependence of the spin signals including both the thermal and the electrical spin signal, which appears in most spin devices because of the band structure of ferromagnetic metals [86,87].

3.3.1 Lock-in Technique

The lock-in technique has been already established to measure the thermal spin signal in metal-based spin devices. In the previous studies [64,87], an alternating voltage with frequency f, $V_{\mathrm{ac}}(f)$, was applied to the FM electrodes, and an alternating voltage, $V^{\mathrm{ac}}(1f)$, and the 2nd harmonic voltage,

$V^{\mathrm{ac}}(2f)$, was measured by using a lock-in amplifier with sweeping an external magnetic field to swich the magnetization configurations: parallel (P) and antiparallel (AP). Please note that the voltage symbols with the superscript (subscript) characters represent that the voltage is the measured (applied) voltage, and "dc" and "ac" mean the direct and alternating voltage, respectively. Since the Joule heating is proportional to I^2, the thermal spin signal, $V_{\mathrm{S}}^{\mathrm{therm}}$, originating to ∇T caused by the heat is also proportional to I^2. The linear I-V character of metal/metal interface enables the technique to extract $V_{\mathrm{S}}^{\mathrm{therm}}$ from V_{S}. The frequency of the applied voltage was less than 20 Hz [64] because such a low frequency does not affect the spin relaxation time because the time scales are different by several orders. As a function of the injected current, I, the detected spin signal, V_{S}, including both electrically and thermally generated spin signals, which is identical to that expressed in Eq.(3.30), is given by the following:

$$V_{\mathrm{S}} = R_1 I + R_2 I^2 + \cdots ,$$

where R_1 and R_2 are parameters pertaining to the electrical spin signal and the thermal spin signal, respectively. By applying alternating voltage and measure the 2nd harmonic voltage, the thermal spin signal can be detected because the Joule heating and the thermal spin signal (included the term of $R_2 I^2$) has the frequency of $2f$. Thus, the thermal spin signal $V_{\mathrm{S}}^{\mathrm{therm}}$ can be separated from the spurious signals $V_{\mathrm{S}}^{\mathrm{spurious}}$.

In the case of the Si-based spin devices, quantitative measurements of the thermal spin signal, $V_{\mathrm{S}}^{\mathrm{therm}}$, by this method may be impossible because of nonlinear factors of the electrical spin signal, which is treated as a spurious spin signal, $V_{\mathrm{S}}^{\mathrm{spurious}}$, in the measurement of the thermal spin signal. The MgO tunneling barrier induces nonlinearity in the I-V characteristics, which generates spurious spin signals in the $2f$ spin signals. The spin polarization of FM also shows nonlinear dependence on the applied voltage [87], which is ascribed to the current dependence of the spin polarization (including the density of states of ferromagnets, heating effects magnon excitation, and so on) and generates spurious spin signals. Bias dependence of the spin signals also impedes the simple detection of the thermal spin signal by the lock-in technique, which has not been considered in the previous studies [64,71], although the bias dependence itself is observed in both metal and semiconductor spin valves [88,89]. To measure the thermal spin signal quantitatively, another scheme to eliminate the spurious signals is needed.

3.3.2 Outline of the New Analysis

In the Si-based spin device, two nonlinear properties impede the conventional lock-in technique to measure the thermal spin signal: the *I*-*V* characteristics and the bias dependence of the spin signal [87]. I constructed a new scheme to eliminate the spurious signals due to them and successfully detected the thermal spin signal in a Si-based spin device. Figure 3.5 shows the thermal spin signals obtained by using the new analysis, which depends quadratically on the applied alternating voltage $V_{\rm ac}$. The black squares represent the magnitude of thermal spin signal, $V_{\rm S}^{\rm therm}(2f)$, and the red line represents the fitting of a quadratic function. As predicted by the theory, my result exhibit clear I^2 dependence. This provides evidence of the spin-dependent Seebeck effect at the interface of Fe and Si via MgO driven by the Joule heating. The details of the experimants, the analysis, and the fitting will be described in the rest of this chapter.

The extracted thermal spin signal, $V_{\rm S}^{\rm therm}(2f)$, which is shown in Fig. 3.5, is the difference of the 2nd harmonic component of spin signals, $V_{\rm S}^{\rm ac}(2f)$, measured by the lock-in technique and the spurious signals, $V_{\rm S}^{\rm spurious}(2f)$, including the nonlinear *I*-*V* and the bias dependence of the spin signals, which is expressed as:

$$V_{\rm S}^{\rm therm}(2f) = V_{\rm S}^{\rm ac}(2f) - V_{\rm S}^{\rm spurious}(2f), \tag{3.32}$$

where f is the frequency of the applied alternating voltage, $V_{\rm ac}$. $V_{\rm S}^{\rm ac}(2f)$ is the spin signal in the 2nd harmonic voltage measured by using the lock-in technique. $V_{\rm S}^{\rm spurious}(2f)$ is the spin signal in the 2nd harmonic voltage obtained by the new analysis combining the dc voltage-current dependence and the dc bias dependence of the electrical spin signal. Note that $V_{\rm S}^{\rm therm}(2f)$ is a part of the thermal spin signal generated by the transient Joule heating generated by an alternating current, since $V_{\rm S}^{\rm spurious}(2f)$ also includes the thermal spin signal due to the Joule heating generated by a direct current.

To eliminate $V_{\rm S}^{\rm spurious}(2f)$, I developed a new analytical method, whose procedure is shown in Fig. 3.6. When an alternating voltage $V_{\rm ac}(t)$ is applied on the two FM electrodes with a bias voltage $V_{\rm dc}$, the current flowing the sample $I(t)$ is calculated by using the *I*-*V* characteristics $G(V)$. $I(t)$ generates electrical spin signals, $V_{\rm S}^{\rm spurious}(t)$, which involves the 2nd harmonic component due to even-order terms in the $G(V)$. I also measured the dc dependence of the spin signal, $R_{\rm S}(I)$. Then, the wave form of $V_{\rm S}^{\rm spurious}(t)$ including nonlinearities to the applied voltage by the combination of G

and R_S is estimated by the following equation:

$$V_S^{spurious}(t) = \{R_S[G[V(t)]\}. \tag{3.33}$$

Finally, I obtained the form in the frequency domain, $V_S^{spurious}(f)$, by performing Fourier transform on $V_S^{spurious}(t)$:

$$V_S^{spurious}(f) = \mathcal{F}\{R_S[G[V(t)]]\}. \tag{3.34}$$

Thus, I evaluated the spurious spin signal in the 2nd harmonic voltage, $V_S^{spurious}(2f)$, due to the nonlinear electrical spin signals.

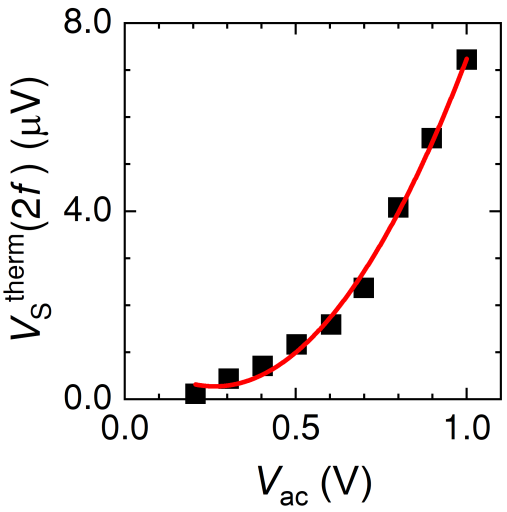

Figure 3.5: V_{ac} dependence of the thermal spin signal.
The detail of discriminating the thermal spin signals and spurious signals is described in the main text. The black closed squares are experimental results and the red solid line shows the fitting line. The quadratic function nicely reproduce the experimental result.

Here, I provide an additional explanation of the meaning of the "transient" Joule heating. When a charge current occurs in a device, the Joule heating occurs at the part that the current flows. The other part of the device remains cool at the beginning because the surface of the device and the substrate is cooled by the air and the stage, respectively, so there is a temperature gradient in the device that transfers the heat. The heat spread to the cooler parts and the distribution of the temperature changes gradually because the time scale of the thermal conduction is much larger than

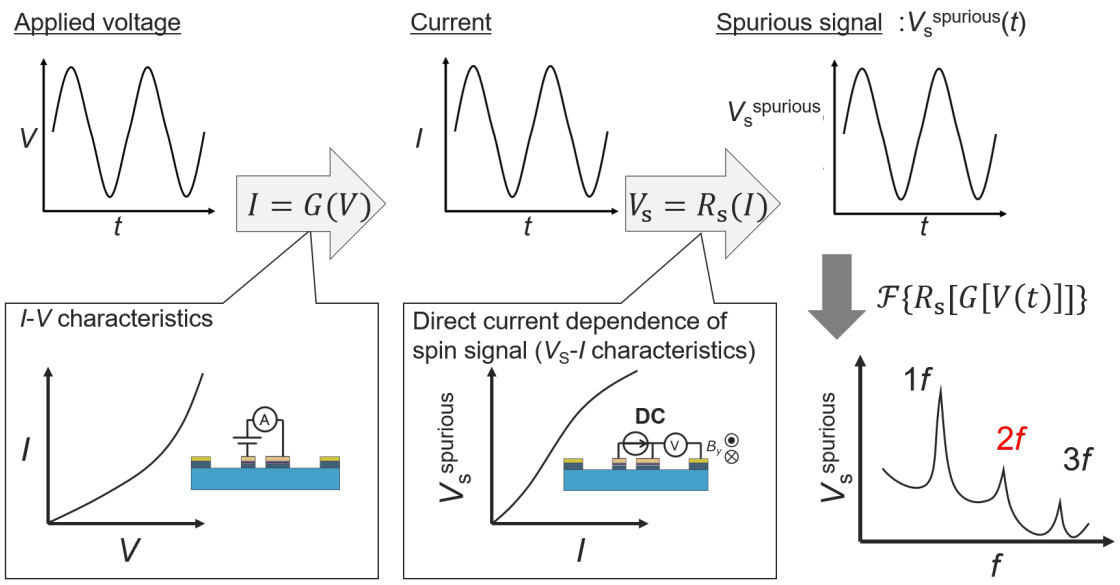

Figure 3.6: Procedure of the Fourier analysis to estimate the spurious spin signal.

that of the electrical conduction. Eventually, the heat spread whole the device, and the distribution of the temperature gradient reaches a steady state. If the distribution of the temperature gradient did not reach the steady state within the time constant of the lock-in amplifier, the distribution of the temperature gradient is referred to as the transient state. The transient Joule heating is the Joule heating in the transient state of the distribution of the temperature gradient in the device.

3.3.3 Sample Structure

A nondegenerate phosphorus (P)-doped ($n \approx 2 \times 10^{18}$ cm^{-3}) silicon lateral spin valve was fabricated on a silicon-on-insulator (SOI) substrate with the structure of Si(100 nm)/SiO_2/bulk Si (see Fig. 3.7), which is the same as the structure of a lateral spin MOSFET. The conductivity of the Si channel was measured by using a four-probe method. The phosphorus was doped to the upper Si by ion implantation. Ferromagnetic tunnel junctions were formed on Si with a higher doping level (n^+-Si, $t = 20$ nm, $n \approx 5 \times 10^{-19}$ cm^{-3}) by using an 0.8-nm-thick MgO tunnel barrier and 17-nm-thick Fe thin film. After the native oxide layer on the Si channel was removed using an HF solution, Pd(3

nm)/Fe(17 nm)/MgO(0.8 nm) is grown on the etched surface by molecular beam epitaxy. The role of the MgO tunneling barrier is to avoid the conductance mismatch problem, which becomes obvious also in thermal spin injection into semiconductors, in addition to electric spin injection [85]; the barrier is indispensable in this experiment. Pd(3 nm)/Fe(4 nm) layers were etched, and Ta (3 nm) was grown on the remaining Fe layer. The sizes of two electrodes F1 and F2 were $0.5 \times 21 \mu m^2$ and 2.0×21 μm^2, respectively. The center-to-center distance between the F1 and F2 (L) was set to 1.75 μm, which were defined by using electron-beam lithography and Ar^+-ion miling. The Si channel surface and sidewalls at the ferromagnetic contacts are buried under the deposited SiO_2 layer. The nonmagnetic electrodes (21×21 μm^2) were made of Al and determined by ion milling. The sample was provided by TDK corporation and Osaka University.

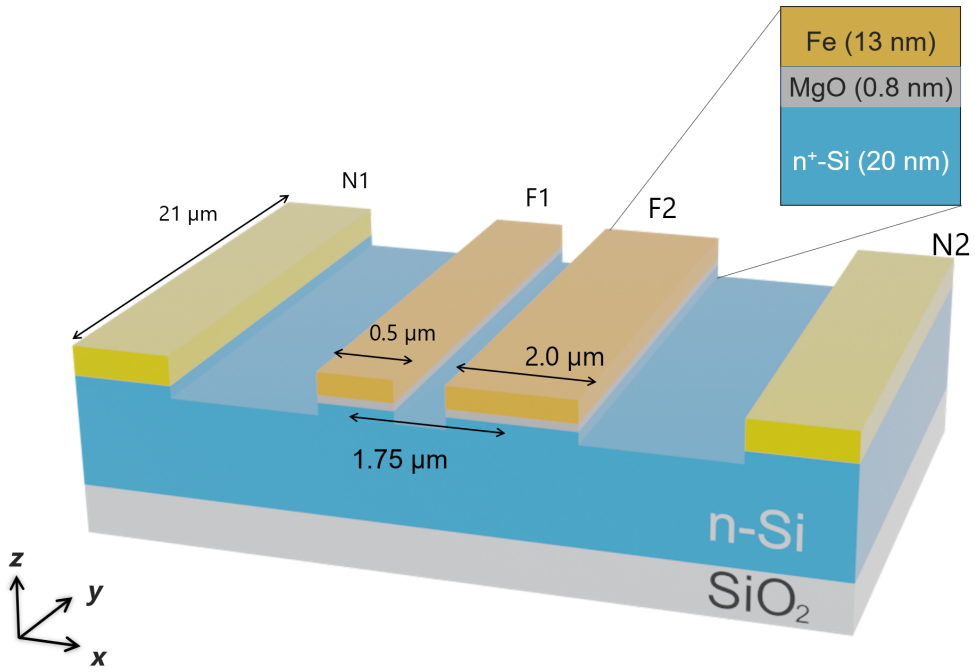

Figure 3.7: Schematic image of the dedicated sample.

3.3.4 Properties of the Sample Related to Spin Transport

The spin signals were measured using a probing station (Janis Research Company Inc., ST-500), source meters (Keithley Instruments, 2400 and 2401), and a digital multimeter (Keithley Instruments, 2010). Thermal spin signals were detected through the ac lock-in technique, in which the alternating voltage was applied using a lock-in amplifier (NF Corporation, LI5654). Biasing direct voltage was also applied to the sample using a homemade bias circuit, and the shape of the applied voltage was monitored by using an oscilloscope. To detect thermal and electrical spin signals in Si, the local-three-terminal (L3T) method was employed [26,42]: Two ferromagnetic electrodes were used and the spin signals were measured in both of the alternating voltages with frequencies of $1f$ and $2f$ as shown in Figs. 3.8. Clear spin signals were observed in the measured voltage at the both frequency, $V^{\rm ac}(1f)$ and $V^{\rm ac}(2f)$, which are shown in Figs. 3.8b and 3.8c, respectively. I confirmed the same amount of the spin signals in two frequencies of applied voltage (17 Hz and 34 Hz), which implies the spin relaxation time and the polarization are independent of the frequency. I also measured the Hanle spin-precession signals that appeared in the 2nd harmonic component of the spin signal (Fig. 3.9). All the signals were detected using the same sample that provides strong evidence for spin injection and transport in Si [26,42]. The other advantage of the L3T method is that, owing to spindrift, it yields larger spin signals than the nonlocal four-terminal (NL4T) method, where only spin diffusion contributes to spin transport [26]. All measurements were performed at room temperature (RT).

The conductivities of Fe and Si at RT were measured to be $\sigma_{\rm F} = 8.3 \times 10^6$ S/m and $\sigma_{\rm N} = 2.12 \times 10^3$ S/m, and the interface RA was measured to be $2.56 \times 10^{-9}\,\Omega{\rm m}^2$ (the spin injection side, F2) and $4.66 \times 10^{-9}\,\Omega{\rm m}^2$ (the spin extraction side, F1). During the measurement, the electric field in the Si spin channel was set to 1.71×10^6 V/m and $L = 1.75$ µm. The parameters of a spin relaxation time and spin diffusion length enabling the numerical calculation of thermal spin signals described above. The measured Hanle spin precession signal is shown in the black plot of Fig. 3.9, which was nicely reproduced by the red fitting line expressing the following function [90]:

$$(1+\omega^2\tau'^2)^{-0.25}\exp\left[\frac{L}{2\lambda_{\rm N}}v\tau' - \frac{L}{\lambda_{\rm N}}\sqrt{\frac{1+\sqrt{1+\omega^2\tau'^2}}{2}}\left\{\cos\frac{\arctan(\omega\tau')}{2} + \frac{L}{\lambda_{\rm N}}\sqrt{\frac{-1+\sqrt{1+\omega^2\tau'^2}}{2}}\right\}\right], \tag{3.35}$$

where, D is the spin-diffusion constant, τ is the spin life time, $\omega = g\mu_B B/\hbar$ is the Larmor frequency,

g is the g factor for the electrons ($g = 2$ in this study), μ_B is Bohr magneton, $\hbar$ is the Dirac constant, v is the spin-drift velocity, and $\tau' = (v^2/4D) + (1/\tau)$ is modified spin lifetime by the spindrift. I obtained the spin lifetime of 6.4 ns and spin diffusion length of 5.0 µm from the fitting.

3.4 Results and Discussion

3.4.1 Discriminating Thermal Spin Signal and Spurious Spin Signal

The spurious contributions are due to the nonlinearity of the I-V curves and the bias dependence of the electric spin signals, as described above. In this measurement, a root-mean-square alternating voltage of 1.0 V was applied to the device in addition to a constant bias voltage (3.0 V), and the nonlinearities around the bias voltage are superposed on the spin signals. I estimated the influence on the basis of experimental data, taking into account the spurious contribution at 17 Hz.

To estimate the spurious signal, I measured the electrical current as a function of the dc voltage applied in the L3T setup and fit the results to a fifth-order polynomial function:

$$I = G(V) = G_1 V_{\mathrm{inj}} + G_2 V_{\mathrm{inj}}^2 + G_3 V_{\mathrm{inj}}^3 + G_4 V_{\mathrm{inj}}^4 + G_5 V_{\mathrm{inj}}^5, \tag{3.36}$$

where G_i ($i = 1 - 5$) is the i th order conductance and V_{inj} is the injection voltage. The fitting curve is represented by the red solid line in Fig. 3.10a, and G_i were obtained as shown in Table3.1.

In the same setup, I also measured the electrical spin signal in a dc configuration as a function of the applied electric current (see Fig. 3.10b). To minimize errors in the fitting and avoid a discrepancy in the fitting curve and the experimental data, wide-range fitting is necessary to corroborate the analysis. If the signals and fittings are limited within a small bias region, it is difficult to check whether the obtained fitting function can sufficiently reproduce the experimental results. Thus, these measurements were implemented at the bias voltage of 3.0 ± 1.5 V. I associated this spin signal, $V_{\mathrm{S}}^{\mathrm{dc}}$, to electrical spin injection and the spurious effects for measurement of the SDSE. I fit these results to a fifth-order polynomial function:

$$V_{\mathrm{S}}^{\mathrm{dc}} = R_{\mathrm{S}}(I) = R_{\mathrm{S1}} I + R_{\mathrm{S2}} I^2 + R_{\mathrm{S3}} I^3 + R_{\mathrm{S4}} I^4 + R_{\mathrm{S5}} I^5, \tag{3.37}$$

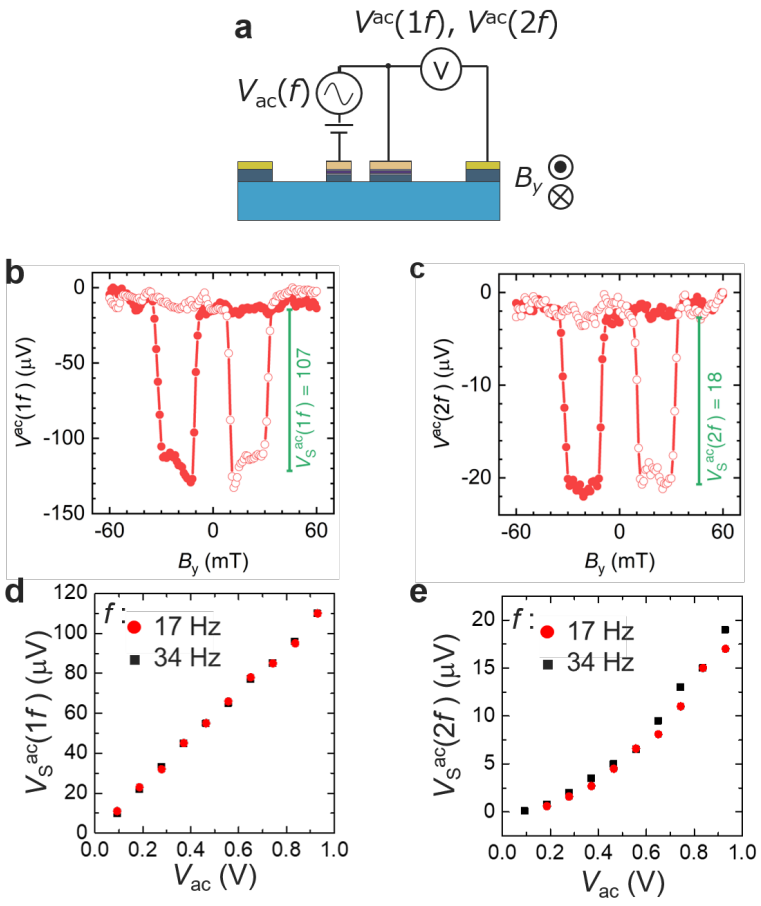

Figure 3.8: Lock in technique measuring thermal spin signal in lateral spin valves.

(a) A schematic image of the lock-in measurement in the L3T configuration. An alternating voltage of frequency f, $V_{ac}(f)$ is applied with a bias voltage and the spin accumulation voltage of frequency $1f$ and $2f$ are measrued at the same time, which is denoted by $V^{ac}(1f)$ and $V^{ac}(2f)$, respectively. A series of measurements were performed with different f (17 Hz and 34 Hz) to confirm the repeatability. The external magnetic field along the y direction switches the spin states P and AP to extract the spin signals. **(b)** An example of the spin signal in the frequency $1f$ measured by the lock-in technique, which is denoted by $V^{ac}(1f)$. The gray and the red plots represent the down sweep and up sweep, respectively. The difference in P and AP states is the spin signal, $V_S^{ac}(1f)$, which is represented by the green bar. **(c)**An example of the spin signal in the frequency $2f$ measured by the lock-in technique, which is denoted by $V^{ac}(2f)$. The gray and the red plots represent the down sweep and up sweep, respectively. The difference in P and AP states is the spin signal, $V_S^{ac}(2f)$, which is represented by the green bar. **(d)** V^{ac} dependence of $V_S^{ac}(1f)$ measrued at f =17 and 34 Hz. The same results were observed in both frequencies. **(e)**V^{ac} dependence of $V_S^{ac}(2f)$ measrued at f =17 and 34 Hz. The same results were observed in both frequencies.

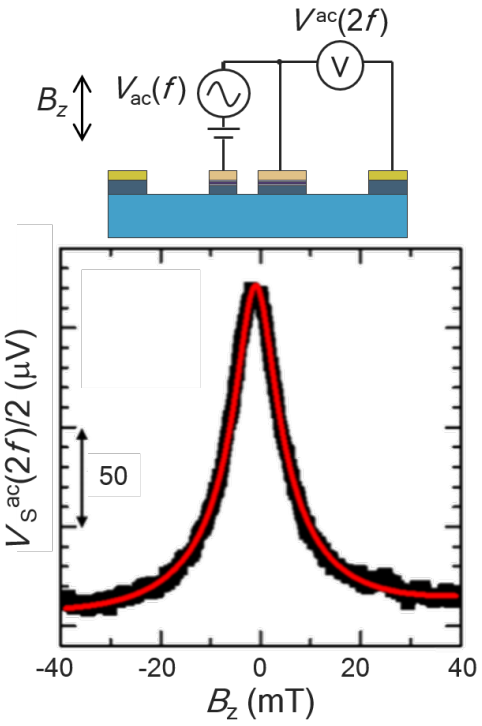

Figure 3.9: Result of Hanle measurements.

An external magnetic field along z direction was swept to measure the Hanle signal using the lock-in technique. The black plot is the experimental result, and the red line is the fitting line.

where $R_{\mathrm{S},i}(i = 1-5)$ is the ith-order resistance under ac and dc excitation. As shown in Fig. 3.10b, the fitting line (red) nicely reproduce the experimental results (black). The obtained values of $R_{\mathrm{S},i}$ $(i = 1-5)$ were shown in Table 3.2.

By substituting Eq.(3.36) for I in Eq.(3.37), I obtained the time-domain spurious signal:

$$V_{\mathrm{S}}^{\mathrm{spurious}}(t) = V_{\mathrm{S}}^{\mathrm{dc}}(t) = \sum_{i=1}^{5} R_{\mathrm{S},i} \left\{ \sum_{k=1}^{5} G_k \left[V_{\mathrm{inj}}(t)^k \right] \right\}. \tag{3.38}$$

I estimated the wave form by setting $V_{\mathrm{inj}}(t) = V_{\mathrm{dc}} + V_0 \sin(2\pi f t)$, where f is the ac frequency (17 Hz), V^{dc} =3.0 V, and V_0 =1.0 Vrms, as shown in Fig. 3.11a. Through Fourier transform, the 2nd harmonic component, $V_{\mathrm{S}}^{\mathrm{spurious}}(2f)$, was calculated. The spurious spin signal in a frequency-domain, $V_{\mathrm{S}}^{\mathrm{spurious}}(f)$, are calculated as shown in Fig. 3.11b. The blue and the red allows indicate the $1f$ and $2f$ components: $V_{\mathrm{S}}^{\mathrm{spurious}}(1f)$ and $V_{\mathrm{S}}^{\mathrm{spurious}}(2f)$, respectively. The value of $V_{\mathrm{S}}^{\mathrm{spurious}}(1f)$ is 106 μV(the blue bar in Fig. 3.11c), which is consistent with the result of the lock-in measurement, $V_{\mathrm{S}}^{\mathrm{ac}}(1f)$ (the green bar in Fig. 3.11c). On the contrary, the value of $V_{\mathrm{S}}^{\mathrm{spurious}}(2f)$ was 11 μV(the red bar in Fig. 3.11d), which is inconsistent with the result of the lock-in measurement, $V_{\mathrm{S}}^{\mathrm{ac}}(2f)$ (ca. 18 μV: the green bar in Fig. 3.11d). Note that the calculated $2f$ signal, $V_{\mathrm{S}}^{\mathrm{spurious}}(2f)$, is not the thermal spin signal due to SDSE but the spurious signal due to electrical spin injection attributed to the nonlinearity of the I-V and the bias current dependence of the electrical spin signal. The difference of the $V_{\mathrm{S}}^{\mathrm{spurious}}(2f)$ and $V_{\mathrm{S}}^{\mathrm{ac}}(2f)$ is the actual thermal spin signal due to transient Joule heating, $V_{\mathrm{S}}^{\mathrm{therm}}(2f)$.

I compared the applied alternating voltage (V_{ac}) dependence of $V_{\mathrm{S}}^{\mathrm{spurious}}(1f)$ [$V_{\mathrm{S}}^{\mathrm{spurious}}(2f)$] to that of $V_{\mathrm{S}}^{\mathrm{ac}}(1f)$ [$V_{\mathrm{S}}^{\mathrm{ac}}(2f)$] as shown in Fig. 3.12. Regarding $1f$ component of the spin signals, $V_{\mathrm{S}}^{\mathrm{spurious}}(1f)$ nicely reproduces $V_{\mathrm{S}}^{\mathrm{ac}}(1f)$, which supports the validity of the analysis (Fig. 3.12a). On the other hand, there was a clear difference between $V_{\mathrm{S}}^{\mathrm{spurious}}(2f)$ and $V_{\mathrm{S}}^{\mathrm{ac}}(2f)$ (Fig. 3.12b), which implies the appearance of the thermal spin signal due to transient Joule heating.

The new analysis now enabled the extraction of the thermal spin signals by eliminating the exact magnitude of the spurious signals. In consequence, the net thermal spin signals, $V_{\mathrm{S}}^{\mathrm{therm}}(2f)$, are obtained by subtracting $V_{\mathrm{S}}^{\mathrm{spurious}}(2f)$ from $V_{\mathrm{S}}^{\mathrm{ac}}(2f)$ [see Eq.(3.32)], and they exhibit a quadratic dependence on the applied alternating voltage, V_{ac} – the evidence for successful thermal spin-signal detection from a Si-based spin valve (Fig. 3.5). The red line represents the fitting curve of $V_{\mathrm{S}}^{\mathrm{therm}}(2f) = 12.8(V_{\mathrm{ac}} - 0.27)^2 + 1.1$ μV. The slight shift of the bottom of the quadratic function from the origin

is attributable to the undetectably small thermal spin signal: when the amplitude of V_{ac} is small, the thermal distribution reaches the steady-state within a shorter time than the time constant of the lock-in amplifier (300 ms). To note is that the magnitude of $V_{\mathrm{S}}^{\mathrm{spurious}}(1f)$ in this estimation is in good agreement with the magnitude of $V_{\mathrm{S}}^{\mathrm{ac}}(1f)$ (Fig. 3.11c) and the result of the fifth-order fitting shows the coefficients of the higher-order term becomes monotonically and sufficiently smaller as the order becomes higher (Tables 3.1 and 3.2). Both results show the validity of the new analysis to distinguish the thermal spin signal.

The spin-dependent Seebeck coefficient of Fe is calculated to be 6 µV/K, based on the deffinition $S_S \equiv S_\uparrow - S_\downarrow = \alpha S$[64,84], so the temperature gradient between Fe and Si is estimated to be about 200 mK for a thermal spin signal of 7 µV, which are the reasonable values.

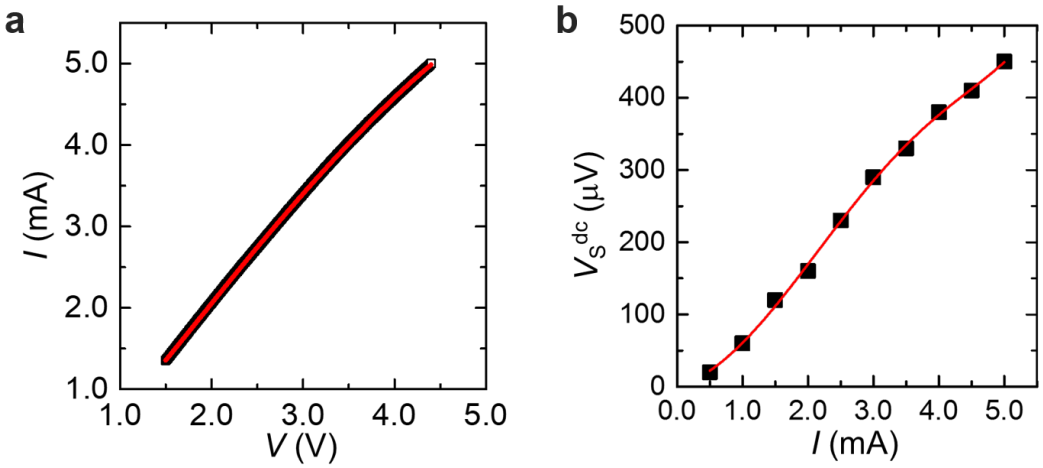

Figure 3.10: Results of the measurements and analysis

(a) *I-V* characteristics at the voltage around 3.0 V–the dc offset voltage in the experiment. The black plots are experimental results and the red solid line is the fitting curve [the fifth-order polynomial function Eq.(3.36)]. The fitting results are shown in table 3.1. **(b)** A direct current dependence of the electrical spin signal. The black closed squares are experimental results and the red solid line is the fitting curve [the fifth-order polynomial function Eq.(3.37)]. The fitting results are shown in table 3.2.

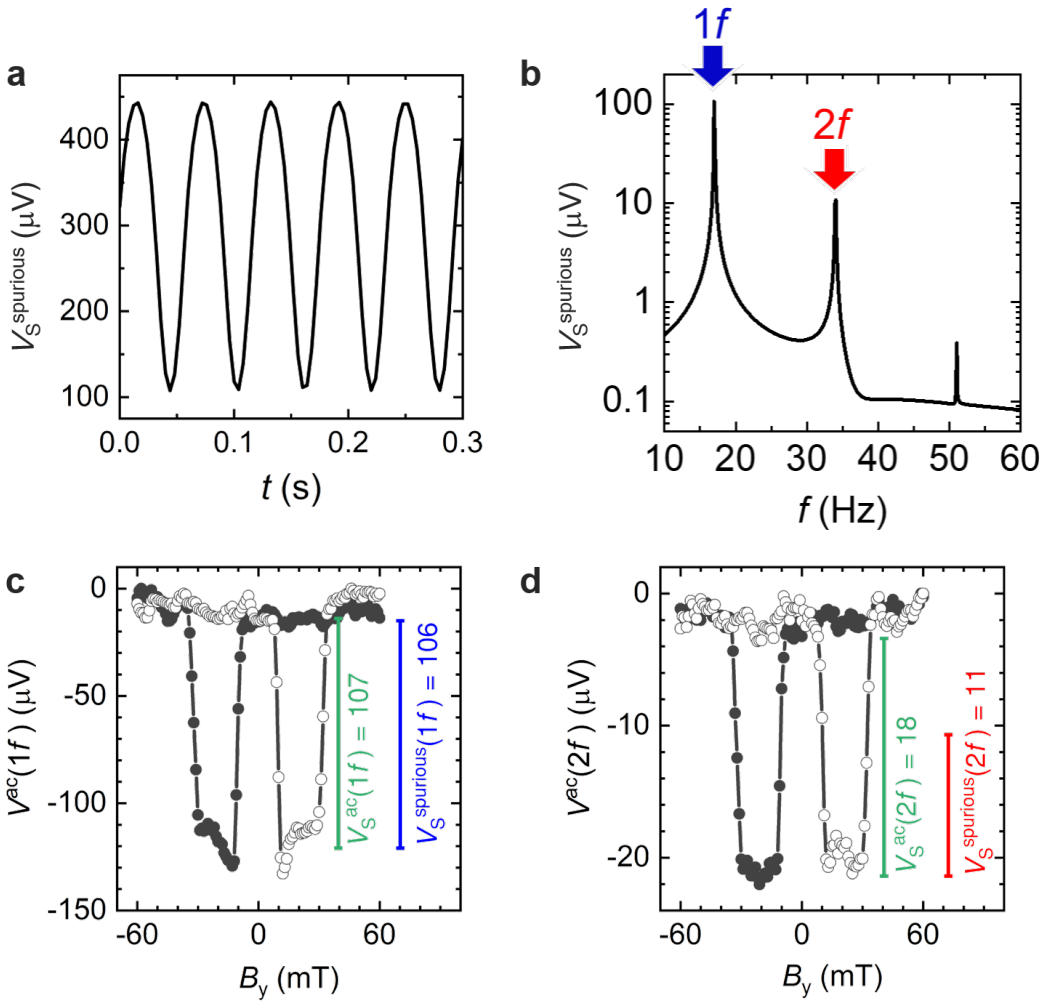

Figure 3.11: Fourier analysis of the electrical spin signal.

(a) Time-domein spectrum of the electric spin signal under the ac (17 Hz) electric current application. **(b)** A Fourier transform spectrum of the electric spin signal. **(c)** Comparison of $V_S^{ac}(1f)$ (the gray plot and the green bar) and $V_S^{spurious}(1f)$ (the blue bar) at dc voltage of 3.0 V, ac voltage of 1.0 V, and the ac frequency of 17 Hz. **(d)** Comparison of $V_S^{ac}(2f)$ (the gray plot and the green bar) and $V_S^{spurious}(2f)$ (the red bar) at dc voltage of 3.0 V, ac voltage of 1.0 V, and the ac frequency of 17 Hz.

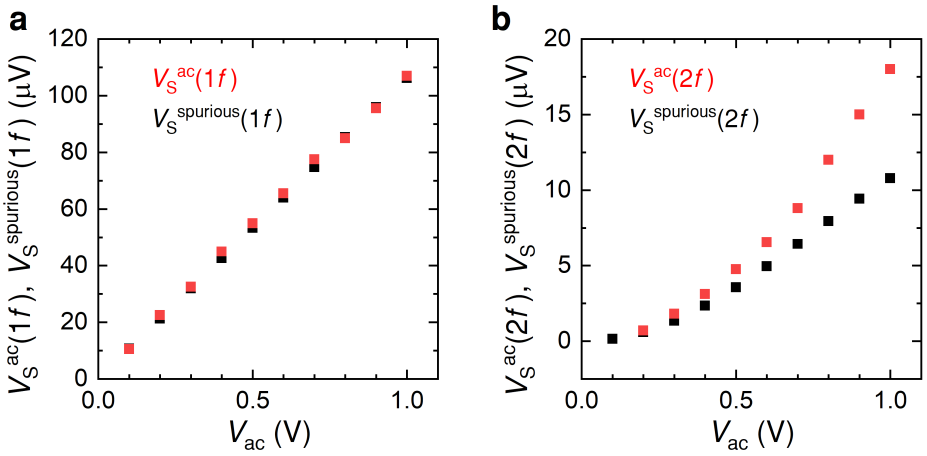

Figure 3.12: Results of the measurements and analysis

(a) Comparison of the measured $1f$ spin signal $V_S^{ac}(1f)$ to the estimated spurious spin signal $V_S^{spurious}(1f)$ by Fourier analysis. The black and the red plots indicate $V_S^{spurious}(1f)$ and $V_S^{ac}(1f)$, respectively. **(b)** Comparison of the measured $2f$ spin signal $V_S^{ac}(2f)$ and the spurious signal $V_S^{spurious}(2f)$ that is due to the nonlinearity of the I-V curve (Fig. 3.10a) and the bias current dependence of the electric spin signal (Fig. 3.10b). The procedure of estimating the spurious signal $V_S^{spurious}(2f)$ is described in the main text. The black and the red plots indicate $V_S^{spurious}(2f)$ and $V_S^{ac}(2f)$, respectively. The transient thermal spin signal is obtained by subtracting the spurious signals from the measured $2f$ spin signal $V_S^{ac}(2f) - V_S^{spurious}(2f)$, which is shown in Fig. 3.5.

Table 3.1: Coefficients of each order of the I-V characteristics.

Label	Value
G_1 (A/V)	-2.95×10^{-5}
G_2 (A/V^2)	1.04×10^{-6}
G_3 (A/V^3)	-3.58×10^{-10}
G_4 (A/V^4)	5.80×10^{-14}
G_5 (A/V^5)	-3.84×10^{-18}

Table 3.2: Coefficients of each order of the $V_{\mathrm{S}}^{\mathrm{dc}}$-$I$ characteristics.

Label	Value
R_{S1} (μV/mA)	26.4
R_{S2} (μV/mA^2)	36.6
R_{S3} (μV/mA^3)	−0.626
R_{S4} (μV/mA^4)	−2.05
R_{S5} (μV/mA^5)	0.244

3.4.2 Spin Currents Added by Thermal Current

This chapter aims to enhance the spin signal in a Si-based spin device, so I estimated how much the SDSE enhances the spin signal. The spin signal measured at 1.25 V was 60 μV as shown in Fig. 3.13a. Considering the case of $V_{\mathrm{dc}} = 1.25$ V, the power consumption is ca. 1.8 W in this device because the resistance of the device is 0.86 Ω. Since the thermal spin signal depends on V_{dc}^2 as described above, the thermal spin signal is estimated to be 12 μV by the extrapolation of the quadratic function as shown in Fig. 3.13b. Thus, the thermal spin signal occupies 20% of $V_{\mathrm{S}}^{\mathrm{dc}}$, which means SDSE is not trivial in the devices. Since the power consumption in conventional electronic devices is wasted as heat and the amount is comparable to the device, the heat assists the spin signal in spin MOSFETs by transfer the heat on the array of the spin MOSFETs.

3.5 Summary

I developed a new method to extract the thermal spin signal in a semiconductor-based spin valve, and achieved thermal spin-signal generation in nondegenerate Si by exploiting the spin-dependent Seebeck

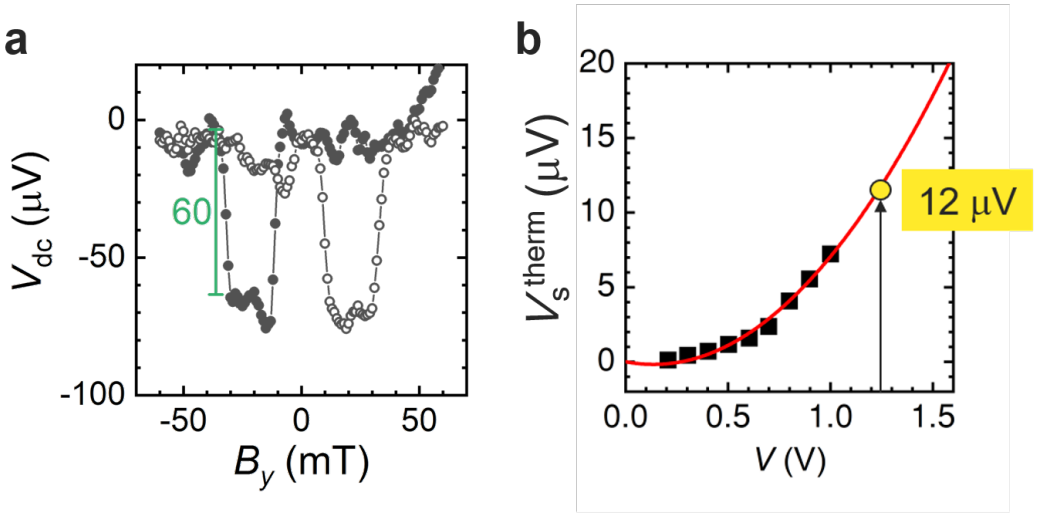

Figure 3.13: Contribution of spin-dependent Seebeck effect to the spin signal.

(a) A spin signal of 60 μV measured in the L3T configuration with applied voltage of dc 1.25 V. **(b)** The estimated thermal spin signal is 12 μV by the extrapolation to 1.25 V.

effect– making a spin current from the temperature gradient at the metal/Si interface. This is the first demonstration of the spin-dependent Seebeck effect not only in Si but in all of the semiconductors. The thermal gradient at the interface between Fe and Si generates a spin current in the Si, which is detected as a 2nd harmonic component of the spin signal at the detector ferromagnet. A simple expansion of the conventional spin drift-diffusion model that takes into account the spin-dependent Seebeck contribution reproduces the experimental result and indicates that semiconductor materials are more efficient for heat recycling compared to metallic materials. The present approach is applicable to heat recycling in Si-based devices, including spin MOSFETs. The spin-dependent Seebeck effect adds 20% of the spin signal if a dc voltage of 1.25 V is applied on the sample in the Si-based spin devices. Thus, the fruits of this chapter is that the thermal assist of spin current is possible and occupies 20%.

Chapter 4

Ohmic Contacts on n-type Si with a Ferrimagnetic Metal

In this chapter, for the first time, an ohmic contact of a ferrimagnetic metal on a nondegenerate n-type Si is demonstrated, which paves a new way to enhance MR ratio by reducing the spin-independent parasitic resistance. I use FeGd alloy belonging to the rare earth-transition metal alloys, which are known to have a finite magnetization above 300K and are expected to have a low work function; these two features satisfy the requirements for ferromagnetic electrodes of the Si-based spin devices. Surprisingly, just 20% of Gd doped in Fe reduces the averaged resistance two orders from $25\,\Omega\mathrm{cm}^2$ to $0.21\,\Omega\mathrm{cm}^2$ at a bias of $\pm 1.0\,\mathrm{V}$. I also find that the work function decreases largely (from 4.9 eV to 3.0 eV) when Gd is added to Fe by 20% – the largest dependence of the work function to the composition among binary alloys.

4.1 Introduction and Motivation

Improvement of the magnetoresistance (MR) ratio involves a smaller interfacial resistance of a ferromagnetic electrode and a Si channel. Figure 4.1 shows my strategy to reduce the interface resistance, R_i. To reduce R_i, the resistances, r, of the Schottky barrier and the MgO tunnel barrier should be reduced. Thinner tunnel barrier will decrease R_i, but the barrier is already atomically thin (0.8 nm) in our devices, and making it thinner is ineffective. This chapter focus on the r of the Schottky barrier. The next alternatives are reducing the height or the thickness of the Schottky barrier. In conventional semiconductor-based electronic devices, a highly doped area is formed to make a thinner Schottky barrier, but this methodology is unsuitable for spin devices because the highly doped impurities disperse the electrons' spin injected to Si [15,91]; the spin devices require another technology without highly doped region. Schottky barrier height (SBH), which strongly affects the resistance, depends on the work function (WF) of the metal [92]. The dependence (S-parameter) of Si is 0.2 [93], which allows reducing SBH by using small WF metal. Two methodologies allow reducing the SBH by combining a ferromagnetic metal (FM) with a low WF metal: bilayer and alloy. The bilayer has been already examined and revealed to be unsuitable because it sacrifices the spin polarization [94]. Thus, I focus on the alloy.

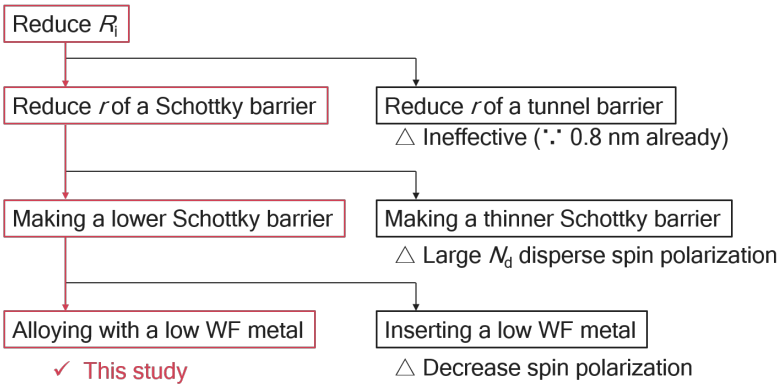

Figure 4.1: Strategy to reduce the resistance of metal/Si interfaces R_i.

In the previous study, they examined NiFe/Gd, using NiFe for a ferromagnet and Gd for a low WF metal [94]. The effect of a low WF layer is clear as shown in Fig. 4.2a. Without Gd (the brown plot

in Fig. 4.2a), the current rectifying effect due to the Schottky barrier is significant. The inserted Gd layer increases the current in the spin injection side (positive bias voltage). The thickness dependence of RA is shown in Fig. 4.2b. The low WF of Gd reduces the SBH and the resistance of the interface. The thicker the Gd layer is deposited, the less RA appears; just 1 nm is enough to eliminate the Schottky barrier. The problem is the spin polarization; the 1 nm-thick Gd layer neutralizes the spin polarization ratio at 300K because the paramagnetic Gd reduces the spin polarization of the injected electrons (see the purple plot in Fig. 4.2c).

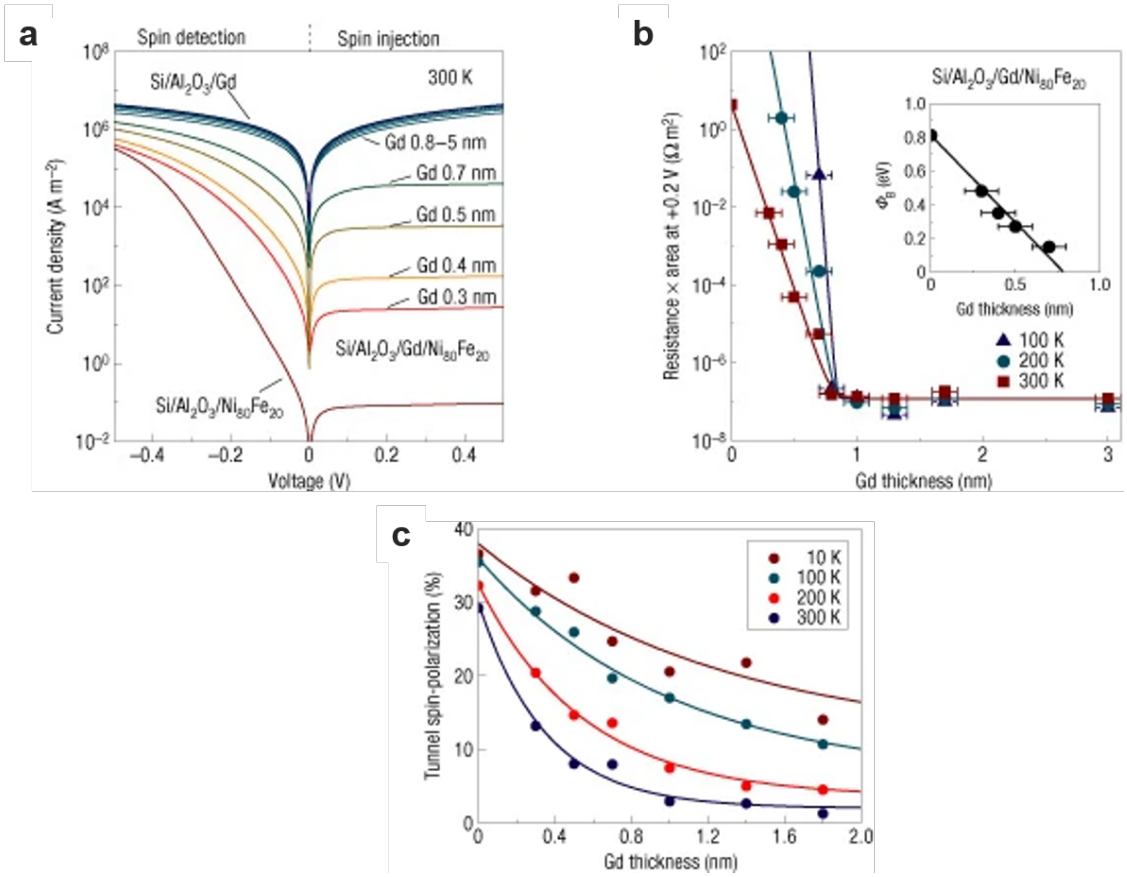

Figure 4.2: Effects of low work funciton metal on the interface resisntance and spin polarization.

(a) The I-V characteristics measured at 300K. The resistance was reduced by inserting Gd into the Ferromagnet ($Ni_{80}Fe_{20}/Al_2O_3$ interface), and the thicker Gd reduce the resistance more. **(b)** The Gd thickness dependence of the resistance area product and the SBH of the $Si/Al_2O_3/Gd/Ni_{80}Fe_{20}$ structure. **(c)** Gd thickness dependence of the spin polarization. The figure is quarted from [94].

Controlling WF by alloying, which is called work function engineering, has attracted attention from the electronics researchers[95,96], but few reports use FMs[97]. By using noble metals (Cu, Ag, and Au), linear composition dependence of SBH was reported as shown in Figs. 4.3 and 4.4[98,99]. The results imply the possibility to reduce the SBH at the interface of the ferromagnetic electrodes by alloying a ferromagnet and a low WF metal. To overcome the bottleneck of Si-based spin devices, the technique is efficient if the spin polarization at E_{F} is saved.

Table 4.1 shows band diagrams of the metal/Si interface, which compares the aim of this chapter with conventional FM (Fe) and a low WF metal (Gd). Usually, 3*d*-transition metals such as Fe are used as the FM electrodes. Stoner criterion provides the Curie temperatures higher than 300K to only three elements[100]: Co, Ni, and Fe. The variation of their WFs is only 0.7 eV (from 4.5 to 5.2 eV[101]), and all of them are higher than the electron affinity, χ, of Si (4.05 eV[92]). The correlation arises Schottky barrier inevitably. The spin-polarized electrons in the FMs are hardly injected into the Si channel because of the large resistance of the inversely biased Schottky barrier. Low WF metal including Gd has a possibility to make an ohmic contact on Si because the WF is 3.1 eV[101], which is less than the χ of Si, but such paramagnetic metals have no spin-polarization. FeGd alloy has spin polarization at 300K (due to the ferrimagnetic nature) and is expected to show a large variation of WF due to the large difference in WF of Fe and Gd, whilst the WF of the alloy is still an open question. Here, I examine both features of the FeGd alloy.

4.2 Theory of Work Function

Work function is a fundamental property of the metallic surface and important for the research fields of material science[93]: It predicts Young ' s modules[102,103], the efficiency of catalysis[104], and the Schottky barrier height in metal/semiconductor interfaces[92] that is the main issue of this chapter. Because of the importance, WF has been discussed since the 1920 ' s[105,106], and many researchers tried to predict that of elemental metals by using computational technology[107,108]. Although the sophisticated computational method provides the accurate values of the WFs[107,109–111], the physical picture was unclear, especially for amorphous alloys. The FeGd alloy has an amorphous structure generally, which hampers the prediction by the first principle calculation. Only a recent paper provides the clue – the image force model[112–114]. The work functions calculated based on the image force

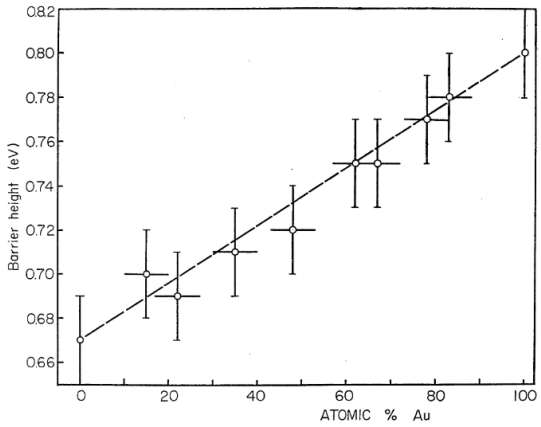

Figure 4.3: Composition dependence of the Schottky barrier height formed by Au-Ag alloy on n-Si. The figure is quoted from [98].

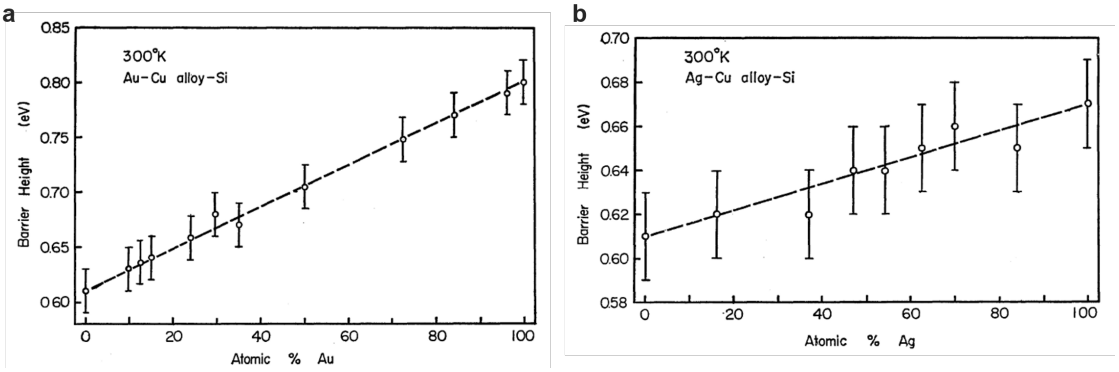

Figure 4.4: Composition dependence of the Schottky barrier height formed by alloys on n-Si. **(a)** Composition dependece of the Au_xCu_{100-x} alloy. **(b)** Composition dependece of Ag_xCu_{100-x} alloy. The figure is quoted from [99].

Table 4.1: Strategy to reduce the height of the Schottky barrier formed at the interface of ferromagnetic metal and n-type Si

Label	**Material**	M **at 300K**	**WF** (ϕ)	**Band diagram at the Metal/Si Interface**
Aim	FeGd	✓	$< \chi$ ($=4.0$ eV[92])	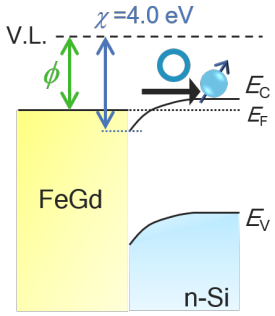
Conventional FM	Fe	✓	4.5 eV[101]	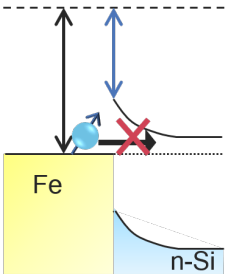
Low WF metal	Gd	–	3.1 eV[101]	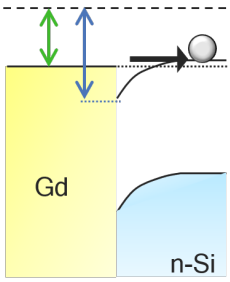

model are compared with the accepted values as shown in Fig. 4.5 [113]. The results of the calculation well agree with the accepted values. The relative difference between the calculated and accepted values rarely exceeds 5%. Another advantage of the model is the wide scope, which predicts WFs of alloys including polycrystals, surface segregation, and amorphous structures [113], so I explain the model.

4.2.1 Image Force Model with Debye Length

I assume the surface of a metal as illustrated in Fig. 4.6. The surface of the metal is a plan wide enough to be assumed infinity and connected to the earth. Consider an electron possessing a charge of $-e$ is extracted from the surface of the metal and placed at a distance x from the surface. The electron receives the image force F: a Coulomb force from its image charge shown in the open circle. I obtain the magnitude as:

$$F = \frac{e^2}{4\pi\epsilon_0(2x)^2}, \tag{4.1}$$

where ϵ_0 is the permittivity of a vacuum. The WF ϕ is defined as the work that is required to move the electron against the image force from the point $x = d_0$ to infinity, expressed as:

$$\phi \equiv W_{\text{image}} = \int_{d_0}^{\infty} F dx = \frac{e^2}{16\pi\epsilon_0 d_0}. \tag{4.2}$$

The minimum distance d_0 means the critical distance at which the image force begins to act on the electron. The d_0 affects significantly on the evaluation of WF because F depends on d_0^{-1} as Eq.(4.2). Brodie assumed the d_0 at first based on the uncertainty principle [112]:

$$d_0 = \frac{\hbar}{\sqrt{2m^* E_{\text{F}}}}, \tag{4.3}$$

where $\hbar$ is Plank's constant, m^* is the effective mass, and E_{F} is the Fermi energy. Halas and Durakiewicz redefined d_0 by using an analogy from the plasma physics— the Debye length: the length scale of the spontaneous polarization and the shielding [113]. They modified the model by applying 'plasma' constituted of free electrons and ions to the surface of the metal [113]. Plasma spontaneously polarizes because the electrons are shifted against ions when an electric charge is placed in it; the polarization depends on the kinetic energy of the electrons. In gaseous plasma, thermal energy ($\frac{1}{2}k_{\text{B}}T$)

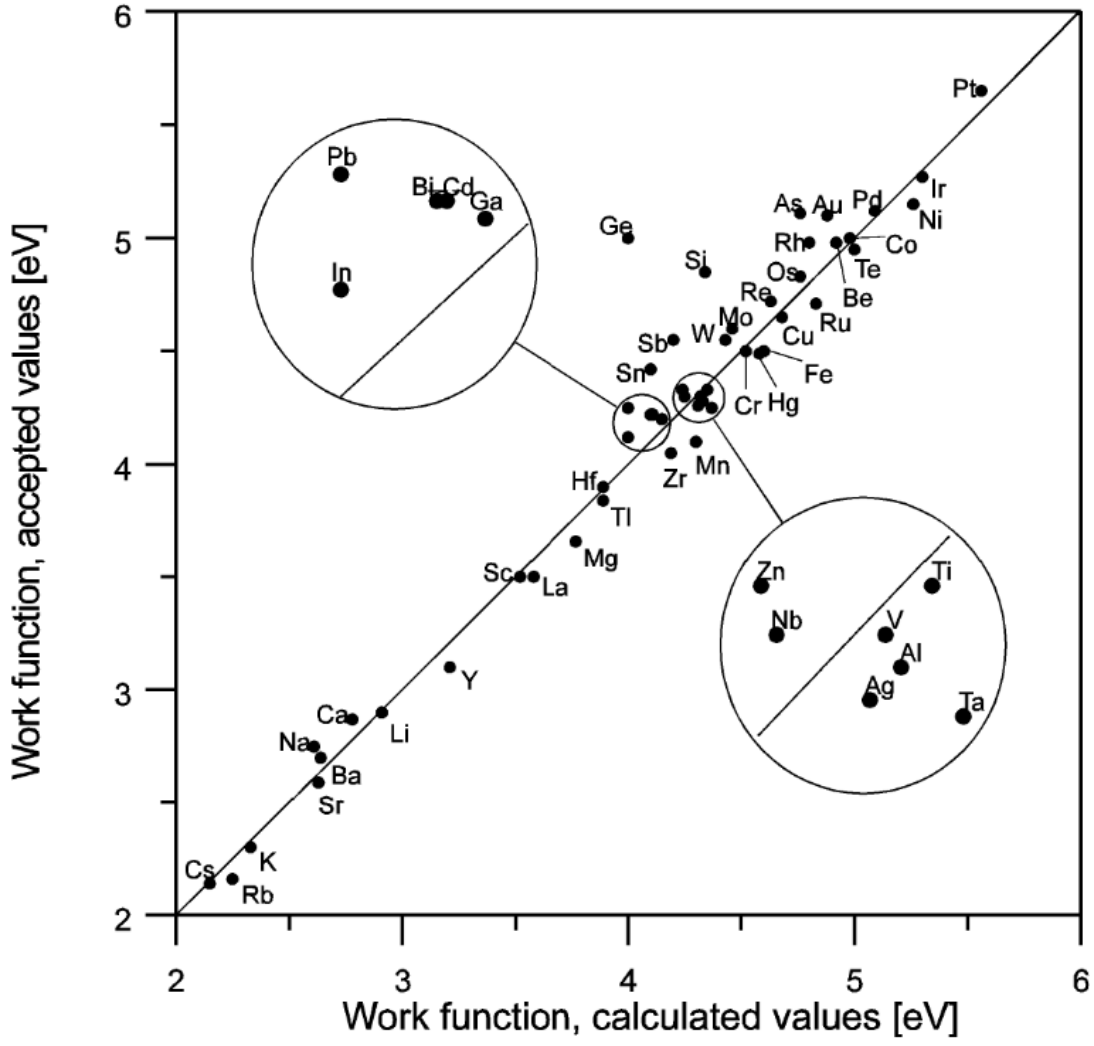

Figure 4.5: Comparison of calculated and accepted work functions of the elements for which data on the Fermi energy.

This figure is quoted from [113].

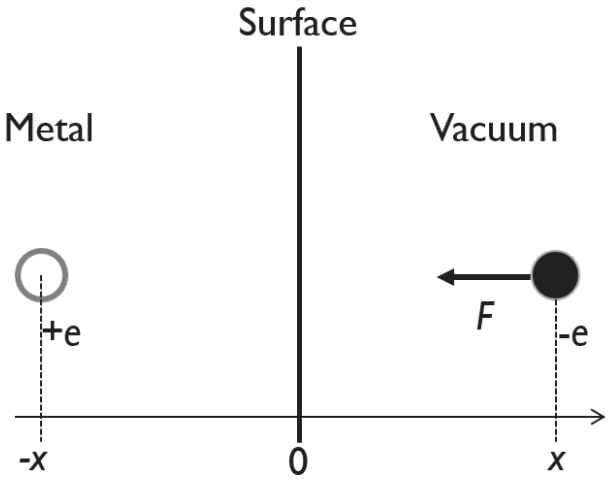

Figure 4.6: Schematic image of the image force acting on an electron at the position x near the metal surface.

supplies the kinetic energy. In the metals, the Fermi energy (E_{F}) supplies the kinetic energy. Then, the polarization length is obtained by substituting E_{F} for $\frac{1}{2}k_{\mathrm{B}}T$, which is expressed as:

$$d = \sqrt{\frac{2\epsilon_0 E_{\mathrm{F}}}{ne^2}}, \tag{4.4}$$

where n is the average density of free electrons in a metal lattice. The metal surface, however, is not a gaseous plasma, so a scaling factor U is needed. In the original paper [113], α is defined as the scaling factor, but in this thesis α was already used as a symbol for a spin polarization, so I use another symbol U for the scaling factor. The value of U is a constant of the order of unity. The displacement of the electrons from their average position induces both the ion screening and the image force. When an electron moves by the distance of d_0 from the metal surface, the mother ion is completely screened, and the image force starts to act on the electron, which is expressed as:

$$d_0 = d/U \tag{4.5}$$

Thus, Eq. (4.2) is modified to as:

$$\phi = W_{\text{image}} = \int_{d/U}^{\infty} F dx, \tag{4.6}$$

where d is the Debye length difined by Eq.(4.4). The integration of Eq.(4.6) brings the scaling factor U to the expression of WF. Thus, ϕ is obtains a convinient form :

$$\phi = \frac{U}{2}\frac{e^2}{8\pi\epsilon_0 a_0}\frac{a_0}{d} = \frac{1}{2}E_0/\left(\frac{d}{a_0}\right) \tag{4.7}$$

where, $a_0 = 0.052918$ nm is the Bohr radius, and E_0= 1 Ryd = 13.6058 eV is the atomic unit of energy. By using the density parameter, r_s, the n is calculated as:

$$\frac{1}{n} = \frac{4}{3}\pi r_s^3. \tag{4.8}$$

Equation(4.4) can be rewritten as:

$$d = \sqrt{\frac{2\epsilon_0 E_{\text{F}}\frac{4}{3}\pi r_s^3}{e^2}} = \sqrt{\frac{E_{\text{F}}}{\frac{1}{2}(e^2/4\pi\epsilon_0 a_0)}\frac{r_s^3}{3a_0}} = \frac{a_0}{\sqrt{3}}\left(\frac{E_{\text{F}}}{E_0}\right)^{1/2}\left(\frac{r_s}{a_0}\right)^{3/2} \tag{4.9}$$

By substituting Eq.(4.9) into Eq.(4.7), a useful form is obtained as:

$$\phi = \frac{U\sqrt{3}}{2}E_0\left(\frac{E_{\text{F}}}{E_0}\right)^{-1/2}\left(\frac{r_s}{a_0}\right)^{-3/2},$$

$$\phi/\text{eV} = \frac{11.783U}{r_s^{3/2}(E_{\text{F}}/E_0)^{1/2}} = \frac{43.46U}{r_s^{3/2}(E_F/\text{eV})^{1/2}} \tag{4.10}$$

where r_s is in atomic units (Bohr radii). ϕ is expressed by using the density parameter r_s and Fermi energy E_{F}. The scaling factor U is equal to unity for most elements; U becomes less than the unity and is equal to 0.86 for alkali metals, Ca, Sr, Ba, Ra, Tl, and rare-earth metals because the lack of surface relaxation decreases the electron densities of the surface[113,114]. The r_s is calculated based on the free electron model by the following formula[115]:

$$r_s = 1.3882 a_0 n^{1/3}, \tag{4.11}$$

$$n = \left(\frac{A}{z\rho}\right), \tag{4.12}$$

where A is the atomic mass given in grams, ρ is the bulk element density at 300K in g/cm^3, and z is the number of free electrons per atom identical to the average ionic valence.

4.2.2 Work Function of Binary Alloy

The image force model also predicts ϕ of an A_xB_{1-x} alloy using the parameters of the constituents. The values of E_F and n are required to calculate the ϕ of an A_xB_{1-x} alloy. The E_F is calculated by the following equation[114]:

$$E_F = xE_{F,A} + (1-x)E_{F,B} + x(1-x)\frac{(E_{F,A} - E_{F,B})(\xi_A/\xi_B - 1)}{x\xi_A/\xi_B + (1-x)} \tag{4.13}$$

where, $E_{F,A(B)}$ are the E_F of the pure constituent A (B), and $\xi_{A(B)}$ is the pure constituent total densities of states that is proportional to the electronic specific heat constant. In the case of an amorphous alloy including FeGd, the n is calculated by the following equation[114]:

$$n_{A-B} = \frac{xz_A + (1-x)zB}{x(M_A/\rho_A) + (1-x)(M_B/\rho_B)}, \tag{4.14}$$

where, $z_{A(B)}$ is the valence, $M_{A(B)}$ is the molar mass, and $\rho_{A(B)}$ is the volumetric mass density of A(B). The predicted values are plotted in black in Fig. 4.7. Here, I used $\xi_{Gd}/\xi_{Fe} = 0.75$[116,117], $E_{F,Gd} = 7.35$ eV, $E_{F,Gd} = 11.81$ eV[113], $z_{Gd} = 3$, $z_{Fe} = 2.5$, $M_{Gd} = 157.25$ mol/cm^3, $M_{Fe} = 55.85$ mol/cm^3, $\rho_{Gd} = 7.9$ g/cm^3, and $\rho_{Fe} = 7.9$ g/cm^3. The WF of FeGd alloy can be less than 4.0 eV that is the electron affinity χ of Si; it has the potential to realize an ohmic contact on n-type Si, when $x > 40\%$ or $U < 0.86$. Because Gd is a rare earth element, the scaling factor U is 0.86, whilst U for Fe is equal to unity[113]. The U of their alloy is unpredictable and will be determined from the experiments.

4.3 Experimental Details

4.3.1 Co-evaporation of Fe and Gd

All FeGd alloys were formed by co-evaporation of Fe and Gd because the composition of the alloy can be controlled by the deposition rate of each source. Fe is evaporated by resistive heating; Gd is

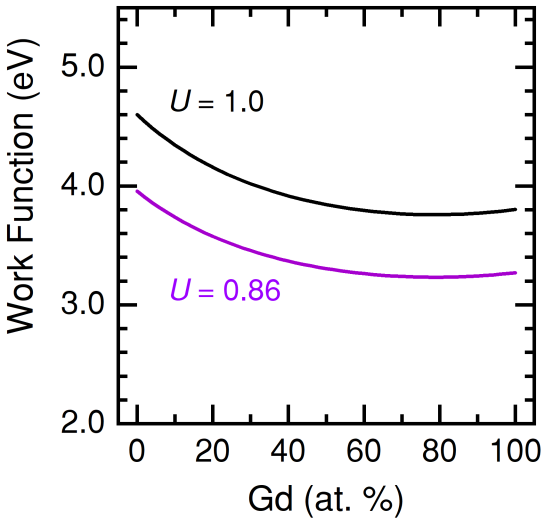

Figure 4.7: Calculated Work functions of the alloys.

The black and the purple lines represent the model of the image force with scaling factor U of 1.0 and 0.86, respectively.

evaporated by an electron beam. The fabrication was carried out using an ultra-high vacuum chamber (the base pressure is less than 4×10^{-6} Pa). To design the composition of FeGd, the deposition rate of each metal was monitored by a thickness meter (ULVAC CRTM-6000G) and corrected with measured thickness by atomic force microscope (HITACHI AFM5000II).

I examined the structure of the co-evaporated film on a piece of Si substrate, the size of which was $10 \times 10\,\mathrm{mm}^2$. The crystalline structure was examined by using X-ray diffraction. Figure 4.8 shows the results of 2θ scans of Fe, Gd and $Fe_{80}Gd_{20}$ alloy. The alloy shows no peaks whilst Fe and Gd show the peaks in 45°and 31°, respectively. The films Fe and Gd have ordered structure, whilst their alloy does not. Therefore, I confirmed these FeGd alloys have amorphous structures.

4.3.2 Magnetization and Spin Polarization of FeGd Alloys

To confirm non-zero magnetization, *M-H* curve was measured at room temperature (nominally 297K) using a vibrating sample magnetometer with an in-plane magnetic field. Figure 4.9a shows the *M-H* curves of Gd, $Fe_{80}Gd_{20}$, and Fe films. Pure Fe and $Fe_{80}Gd_{20}$ showed saturation and hysteresis of the magnetization M; Gd showed no saturation.

To detect spin polarization of electron, anomalous Hall effect was examined by fabricating micro Hall bars ($500 \times 60\,\mu\mathrm{m}^2$). Thermally oxidized Si substrate was prepared and the shapes of the Hall bars were defined by electron-beam lithography (ELIONIX ELS-S50S) with a resist (ZEON ZEP520A). The FeGd films were deposited by the co-evaporation and the lift-off was done. Measurements were carried out using Quantum Design physical property measurement system and the chamber was vacuumed to avoid oxidation during the measurement. The temperature of the chamber was 300K. A schematic image of the measurement is shown in the inset of Fig. 4.9b. Charge current $I = 1.0$ mA was applied in x-direction and the voltage of x (V_{xx}) and y (V_{xy}) direction was measured with sweeping magnetic field along z-direction (B_z). The anomalous Hall effect was detected using $Fe_{80}Gd_{20}$ alloy and Fe: saturation of the Hall resistivity, ρ_{xy}, at a large B_z was observed in the $Fe_{80}Gd_{20}$ alloy at 300 K. The spin-dependent scattering including skew scattering and side jump mostly contributes to the anomalous Hall effect in the sample because of the lack of the intrinsic mechanism due to the amorphous structure. Therefore, we confirmed the non-zero spin polarization at E_F in the $Fe_{80}Gd_{20}$ alloy at 300K.

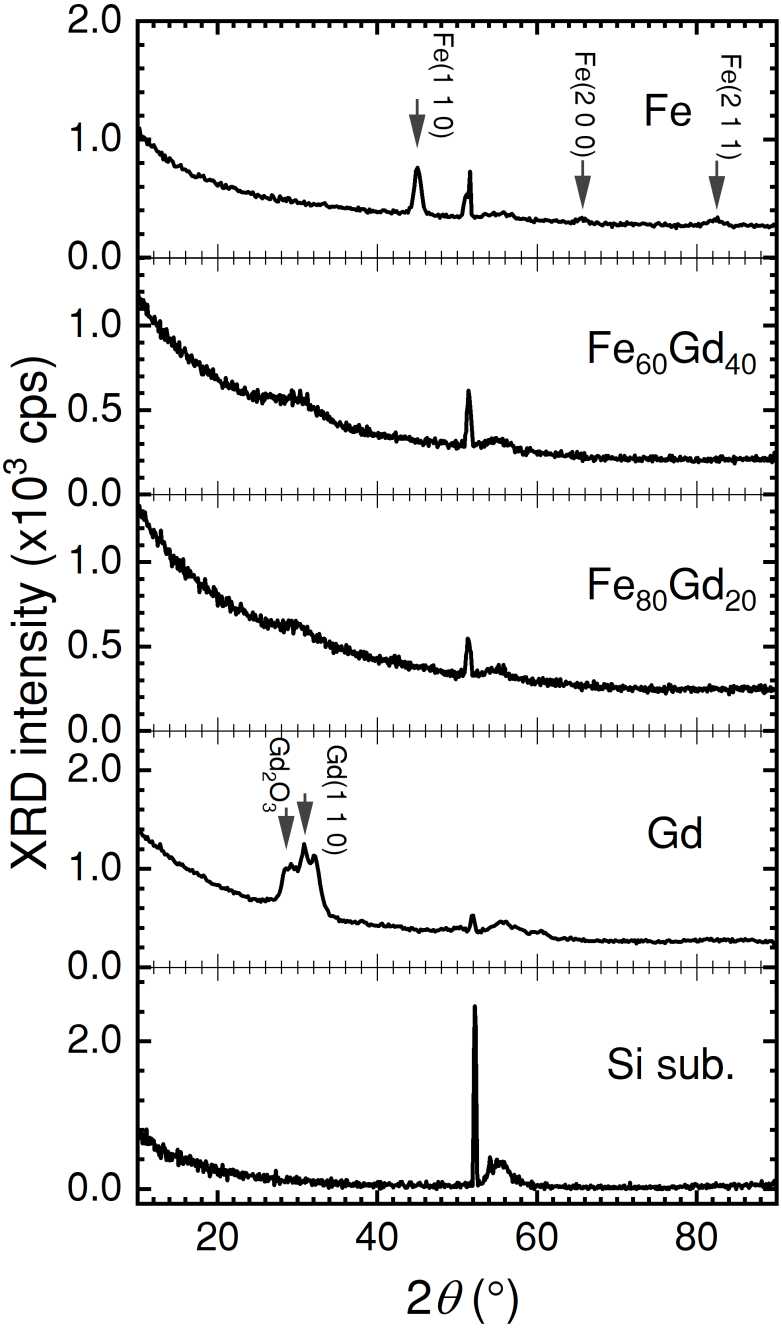

Figure 4.8: XRD patterns of metals and a substrate.

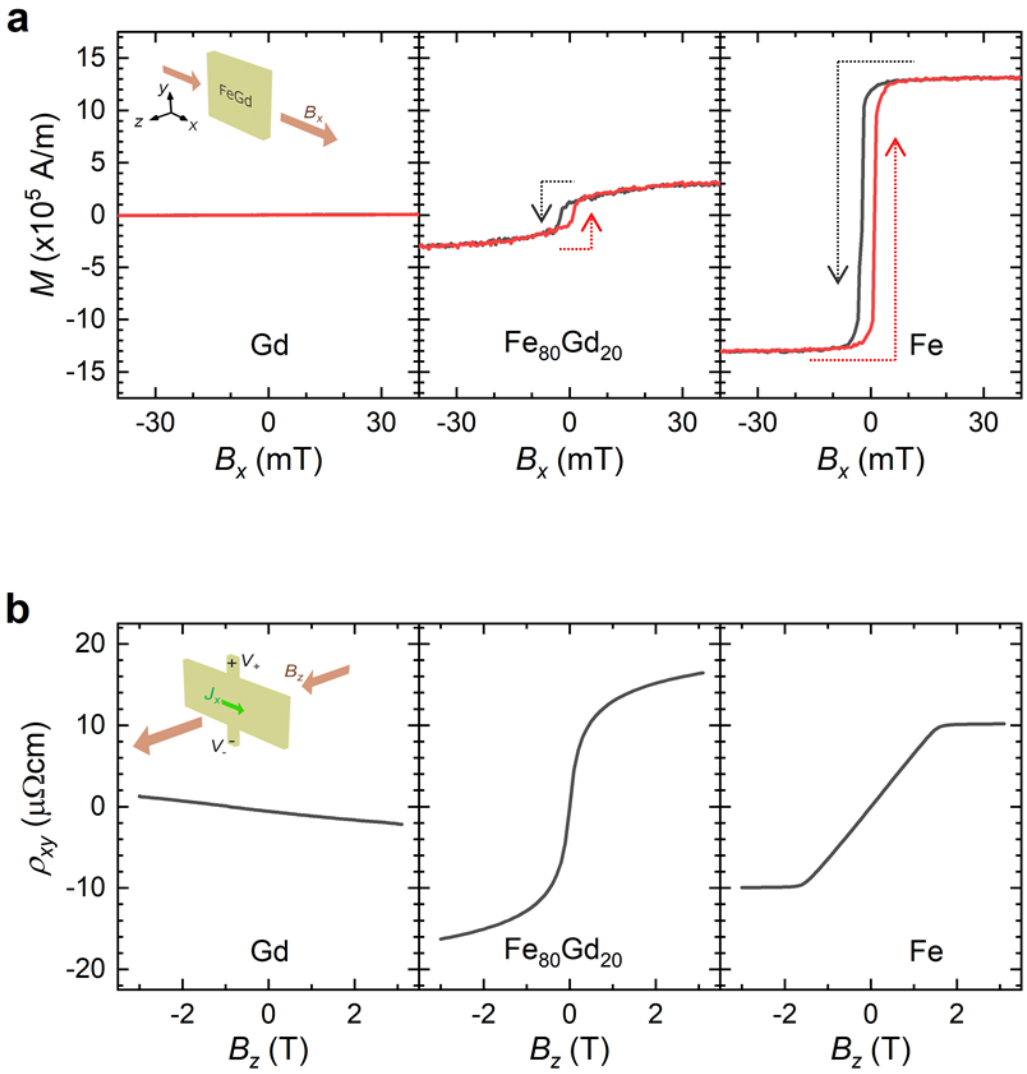

Figure 4.9: *M-H* curves and anomalous Hall effects measrued at a room temperature.

(a) *M-H* curves measured at 297K by VSM. **(b)** Anomalous Hall effect measured with Hall bars at 300K.

4.3.3 Electrical Measurements of the Metal/Si Interface

To measrue I-V characteristics of the metal/Si interfaces, I prepared vertical type Schottky barrier diodes. The structure is, from the bottom of the substrate, AuSb(70 nm)/Si-sub.(500 µm)/FeGd alloys (20 nm)/Cu(10 nm). A piece of n-type Si substrate was cut in the size of $10 \times 10\text{mm}^2$, cleaned by using SEMICO-CLEAN23 with ultrasonic for 3 min, and dipped into HF 2%aq. solution for 30 seconds. On the back of the substrate, ohmic contact of AuSb/n-Si was formed using thermal evaporation in an ultra-high vacuum followed by thermal annealing at 400°C for 1 minute. The surface of the substrate was cleaned by using SEMICO-CLEAN23 with ultrasonic for 3 min and dipped into D. I. water. Circluar patterns were determined on the top surface of the substrate by photolithography using a resist (ZEON ZPN1150). Naturally oxidized layer was removed by dipping HF 2% solution for 30 seconds less than 3 min before being put into a vacuum chamber. Much attention was paid to make the metal/Si interfaces without unintended contermination for I-V measurements because the first layer of the deposition is critical to the I-V characteristics such as Schottky barrier height. C-V measurements were performed to confirm a proper Schottky barrier is formed in the Fe/Si interface using a prober system. The probe frequency was set to 100 kHz. The $1/C^2$-V curve of Fe/n-Si SBD showed linear dependence as shown in Fig. 4.10. The donor density of the Si substrate N_d was estimated by the following equation [118]:

$$N_\mathrm{d} = \left| \frac{e\epsilon_\mathrm{s} A^2}{2} \frac{d(1/C^2)}{dV} \right|^{-1}. \tag{4.15}$$

I obtained the value of $N_\mathrm{d} = 5 \times 10^{15}\ \mathrm{cm}^{-3}$, which means non-degeneragte Si. Then, the built-in potential V_d was extracted from the intercept on the horizontal axis based on the relationship [118]:

$$\frac{1}{C^2} = \frac{2(V_\mathrm{d} - V)}{A^2 e\epsilon_\mathrm{s} N_\mathrm{d}}, \tag{4.16}$$

where $\epsilon_\mathrm{s} = 11.8\epsilon_0$ is the dielectric constant of Si, V is the applied voltage, and A is the area of Fe/n-Si contact, respectively. The Schottky barrier height, Φ_B, was estimated using the follwing equation [118]:

$$\Phi_\mathrm{B} = eV_\mathrm{d} + \Delta E_\mathrm{F} + k_\mathrm{B}T - \Delta\phi, \tag{4.17}$$

where ΔE_{F} is the energy difference between the conduction band bottom and the Fermi level in Si, and $\Delta\phi = 0.03\,\mathrm{eV}$ is the image force lowering[118]. The ΔE_{F} was calculated with the Boltzmann approximation $\Delta E_{\mathrm{F}} = k_{\mathrm{B}}T\ln(N_{\mathrm{C}}/n)$, where n is the density of electrons and $N_{\mathrm{C}} = 2.86 \times 10^{19}\,\mathrm{cm}^{-3}$ is the effective density of states in the conduction band[118]. Thus, I obtained $\Phi_{\mathrm{B}} = 0.61\,\mathrm{eV}$, which is in accordance with a literature[93]. Therefore, the surface of the Si substrate was confirmed to be clean, so the procedure is applicable to the sample preparation for the I-V measurement. In the cases of Gd and $Fe_{80}Gd_{20}$ alloy, the $1/C^2$-V plots were nonlinear and the Φ_{B} was unmeasurable due to a large leakage current (not shown in the figures).

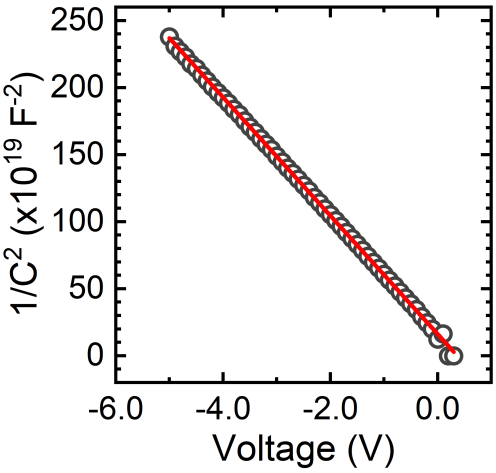

Figure 4.10: $1/C^2$-V plot of Fe/n-Si sample.
The gray circles indicate the experimental result, and the red line indicates the linear fitting.

I-V measurements were carried out at room temperature, and the results are shown in Fig. 4.11. I obtained linear characteristics in $Fe_{80}Gd_{20}$/Si (red line) and Gd/Si (blue line), whilst the current-rectifying characteristics was seen in Fe/Si (gray line). The averaged interface resistance at ± 1.0 V was decreased from $25\,\Omega\mathrm{cm}^2$ to $0.21\,\Omega\mathrm{cm}^2$ by a factor of 100 by adding 20% of Gd to Fe. Thus, I successfully developed a novel material to make ohmic contact to n-Si with finite spin polarization at room temperature.

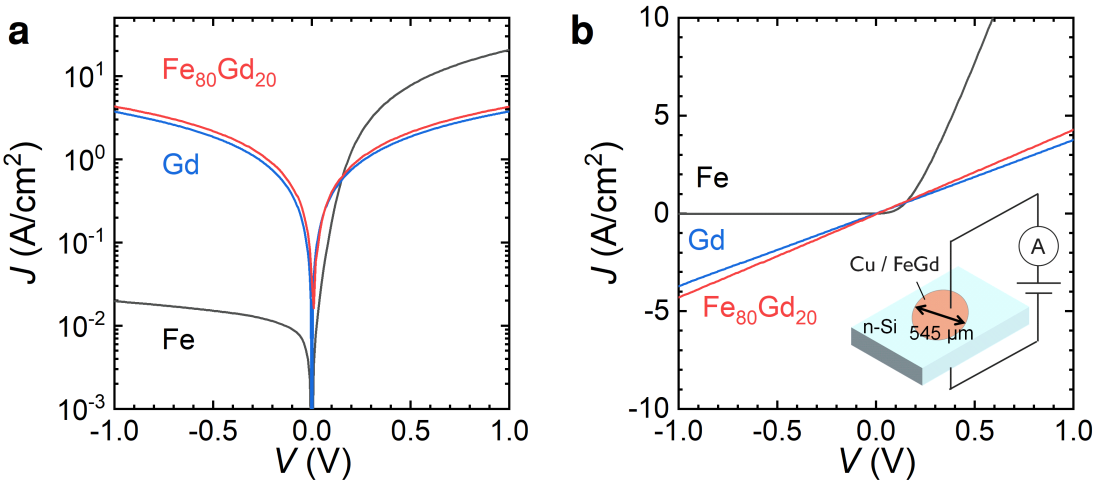

Figure 4.11: I-V charactersistics of the Metal/Si interfaces.

(a) Semilog plot and **(b)** Linear plot. The inset shows schematic image of the measurement. Gray, blue, and red line shows the result of the sample of Fe, Gd and $Fe_{80}Gd_{20}$, respectively. The Schottky barrier in Fe/n-Si interface occurs current rectification character. The SBH was ca 0.6 eV estimated from the C-V measurement as described in the main text. The samples made of Gd and $Fe_{80}Gd_{20}$ on n-Si shows ohmic characteristics; almost same current density was obtained by applying positive and negative voltage**(a)**, and the plots show nice linearlity **(b)**.

4.4 Discussion

I realized ohmic contact on nondegenerate n-type Si by using $Fe_{80}Gd_{20}$ alloy as expected as Fig. 4.1. To confirm the relationship of $\phi < \chi$, the ϕ of $Fe_{100-x}Gd_x$ alloys were investivgated.

4.4.1 Work Function

The work function of an amorphous alloy is predicted by using Eqs.(4.10), (4.13) and (4.14). The validity of the equation is an open question because no experimental evidence was provided so far [114], whilst the WF of an amorphous HfNi alloy was examined using Kervin prove, which is shown by the blue plot in Fig. 4.12 [96]. They claimed the WF of $Hf_{20}Ni_{80}$ is reduced because of the pinning of WF to that of Hf, which is attributable to the surface segregation of Hf [96]; however, the surface composition was unclear because the composition of only the bulk was determined using energy dispersive spectroscopy and time of flight secondary ion mass spectrometry [96]. To discuss WF using the image force model, the surface composition is necessary to eliminate the effect of the pinning by the lower WF element. To measure it, I employed the combination of X-ray photoelectron spectroscopy (XPS) and ultraviolet photoelectron spectroscopy (UPS), which can measure the composition and the WF at exactly the same surface.

I fabricated a sample to measure the composition dependence of WF by co-evaporation of Fe and Gd with changing the rate of each evaporation. First, only Gd was evaporated by 10 nm on a Si substrate. Then the co-evaporation was carried out by reducing the deposition rate of Gd by 30 nm. After the rate of Gd getting to zero, only Fe was evaporated the thickness of 20 nm to circumvent the effect of oxidization. The sample was sent to MST (Foundation for Promotion of Material Science and Technology of Japan) and a series of measurements were carried out using ULVAC-PHI PHI5000 Versa Probe. Both of the measurements of the WF and the surface composition were performed in the same chamber by using UPS and XPS, respectively, following the Ar^+ ion sputtering by a depth of 6 nm. The same cycle was repeated 10 times until the Si substrate appeared.

The compositions of each element measured by XPS and the atomic ratio of Gd (x in $Fe_{100-x}Gd_x$) are shown in Figs. 4.13a and 4.13b, respectively. The horizontal axis shows the total milling depth. Successfully, I obtained a wide variation of Gd concentration at the surface of the FeGd film. The surfaces obtained after the milling depth of 0, 54, and 60 nm contain many atoms other than FeGd

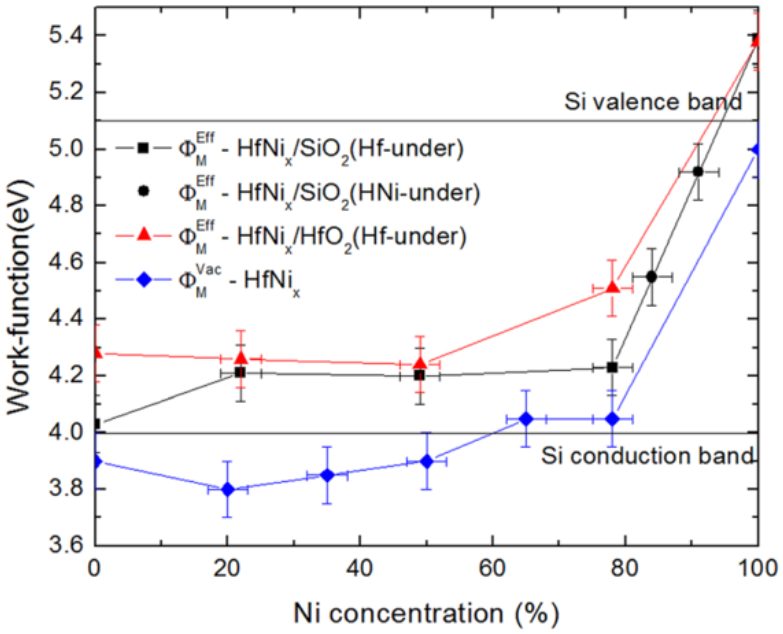

Figure 4.12: WF of amorphous HfNi alloys.

The red and black plots were effective work functions measured by using metal-oxcide-semiconductor strucrutures. The blue plot shows the work function of HfNi alloys measued by Kervin probe method. This figure is adopted from [96].

alloys (O or Si) that hinder the real WF of FeGd alloys. The UPS spectra of these surfaces, therefore, were discarded.

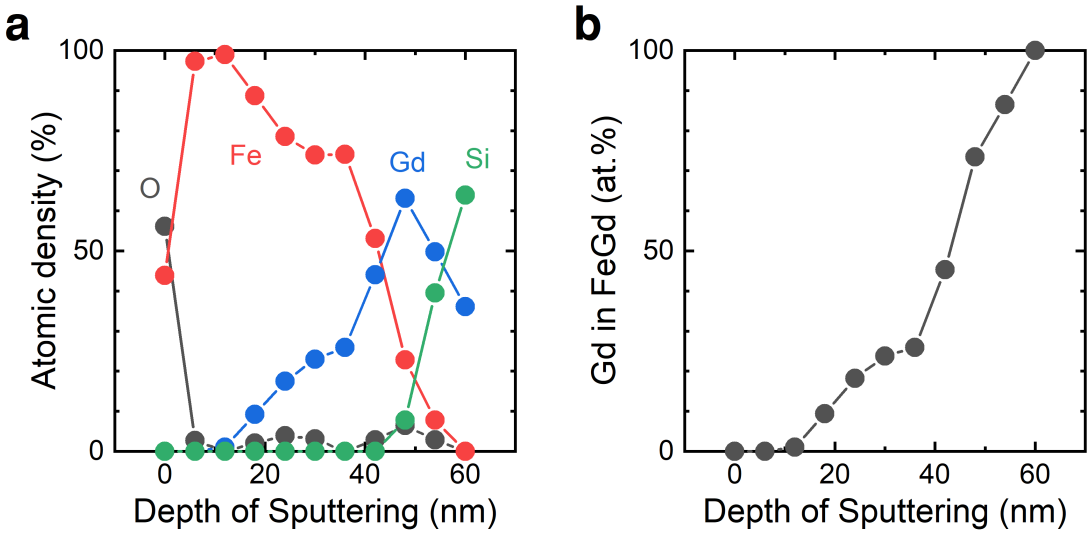

Figure 4.13: Milling depth dependence of atomic compositions measured by XPS.

(a) All the elements measued by XPS. The gray, the red, the blue and the green plots show the atomic densities of O, Fe, Gd and Si, respectively. **(b)** Gd ratio in the FeGd alloy.

A schematic image of the mechanism of UPS measurement is shown in Fig. 4.14. When ultraviolet light is irradiated to a surface of the metal, the energy of the photon, $h\nu$, is transferred to an electron near E_{F} as the kinetic energy. If the energy of the electron gets higher than a vacuum level (V.L.), the electron is emitted from the surface of the metal and the kinetic energy is determined by the detector. Thus, the kinetic energy dependence of the number of detected electrons was obtained as an energy spectrum; the width is defined as W. The maximum kinetic energy is provided by the emitted electrons from the energy level of E_{F}. The minimum kinetic energy is provided by the emitted electrons from the energy level of $E_{\mathrm{F}} - W$ as shown in Fig. 4.14. Therefore, ϕ is obtained by following equation under the irradiation of an ultraviolet (the photon energy is $h\nu = 21.22\,\mathrm{eV}$), since ϕ is the energy difference of E_{F} and the vacuum level:

$$\phi = h\nu - W. \tag{4.18}$$

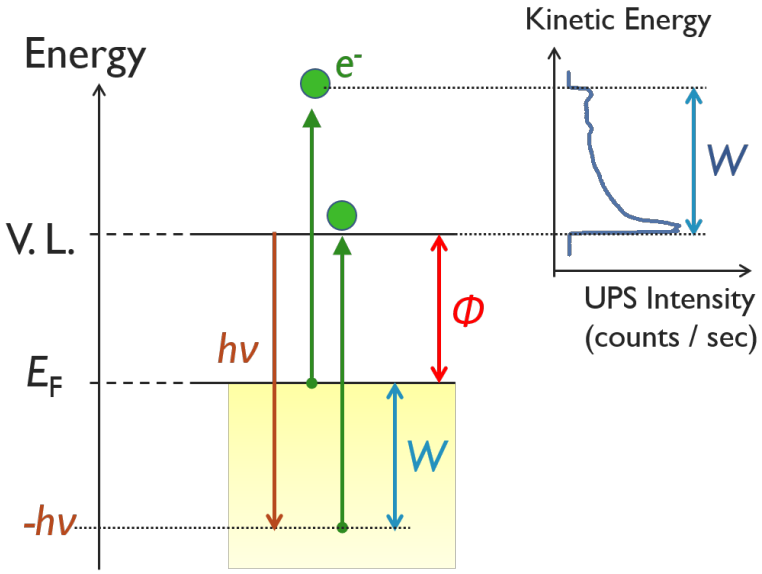

Figure 4.14: Schematic image of UPS measurements to estimate WF.

The obtained UPS spectra were shown in Fig. 4.15. The concentration of Gd is written in each plot. Data of other samples made of uniform films of Fe, Gd, $Fe_{83}Gd_{17}$, and $Fe_{80}Gd_{20}$ were also plotted in the figure. The values of ϕ were evaluated by the fitting of the spectra using a convolution of the Fermi-Dirac function with Gaussian. The positions of E_F as the results of the fitting are shown in the red lines. E_F shifts to higher, and the ϕ decreases when the amount of Gd increases especially in a low Gd range. The central result of this chapter is the large decrease of ϕ at the range of $x < 20\%$, which is unprecedented and noteworthy because the spin polarization of Fe is saved by such a small Gd density.

4.4.2 Comparison with Other Materials

I compared the obtained WFs of FeGd alloys with that of the other ferromagnetic alloys as shown in Fig. 4.16. The green, blue, and pink plots indicate the WFs of NiFe[97], CoFe[101,119], and FeGd, respectively. The pink-filled (open) circles represent the result for the sample with(without) artificially made composition gradient. WFs of FeGd are nearly 1.5 eV lower than that of other ferromagnets in

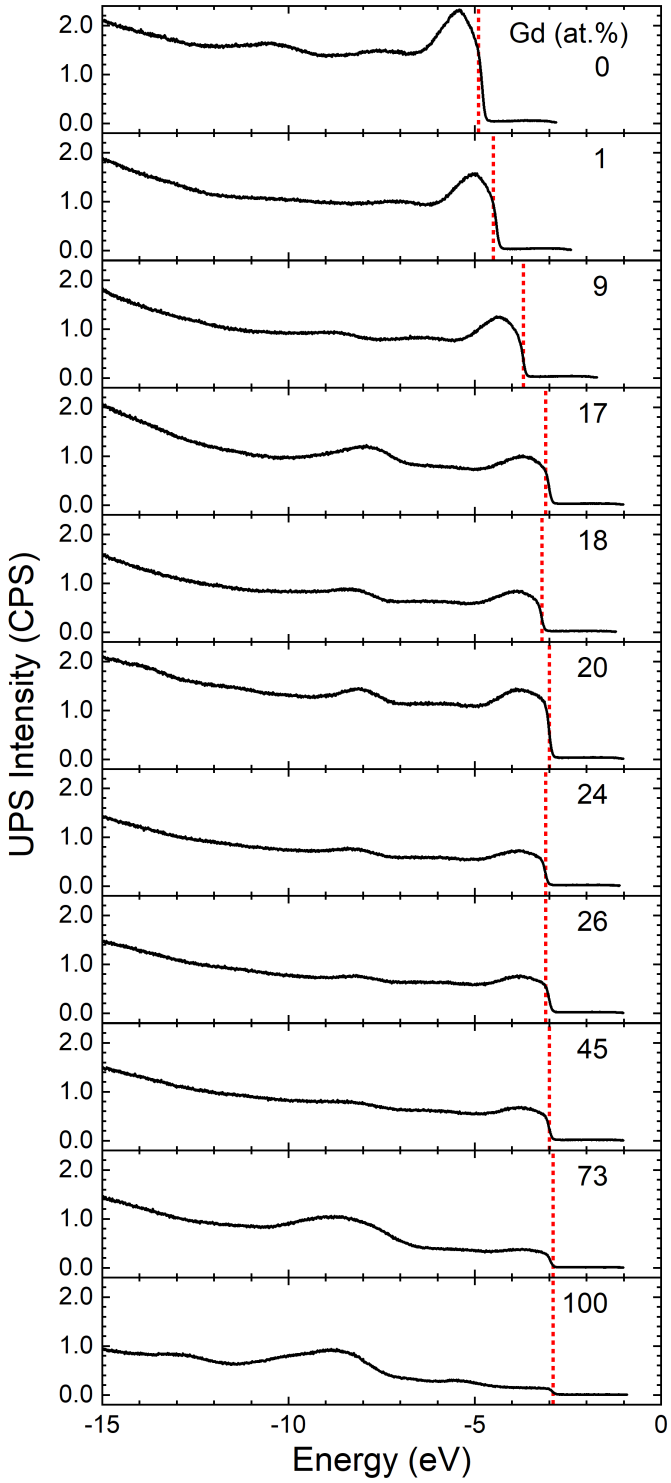

Figure 4.15: UPS spectrum of $Fe_{100-x}Gd_x$ alloys.
The energy $E = 0$ eV indicates the vacuum level. The red dotted lines indicates the Fermi energy.

the range of $x > 20\%$. The drastic change in FeGd in the low Gd concentration range is outstanding because it brings an ohmic contact on n-Si with saving finite spin polarization at room temperature.

For the application for work function engineering, the composition dependence of WF is a key parameter. I define η as the dependence of ϕ on x of $A_{100-x}B_x$ alloy system, where ϕ of A is larger than that of B, by the following equation:

$$\eta \equiv \frac{d\phi}{dx}. \tag{4.19}$$

For a fair comparison among different numbers of the data, I obtained η by a linear fit in the range of $0 < x < 25\%$ because most of the alloys have the maximum η near $x = 0$ as shown in red lines in Fig. 4.17. The threshold is η. FeGd provides the largest η of 88 meV/%: larger than that of the second largest value of HfNi (29 meV/%) almost by a factor of 3 (see Fig. 4.18). The comparison indicates that FeGd is an excellent alloy system for work function engineering.

I discuss the physics behind the large η of $Fe_{100-x}Gd_x$. In the previous study [96], the composition of Hf_xNi_{100-x} was determined only for the bulk. They attributed the change of ϕ to the pinning of by the low ϕ of Hf because the surface composition can differ from that of the bulk [96]. However, my experiments measuring x of the surface excluded the pinning and enabled direct comparison with the image force model by measuring x and ϕ at the same surfaces, which was different from the previous study [96]. The experimental results were compared with the calculated values based on the image force model as shown in Fig. 4.19. Three theoretical predictions based on Eq.(4.10) are represented by the black, the purple, and the blue lines with U =1.00, 0.86, and 0.76, respectively, since U of the alloy is an open question. The nonlinear trend of the theoretical lines in the range of $17\% < \mathrm{Gd} < 100\%$ fits the experimental results well. The drastic change of WF in the range of $0\% < \mathrm{Gd} < 17\%$ is attributable to the change of U, which changes from 1.00 (Gd = 0%) to 0.76 (Gd $\geqq$ 17%). The change in U is possible if the surface recombination vanishes by losing the crystalline structure associating with the amorphous structure because any particular surfaces have the same surface energy [113,114]. In the case of $Fe_{100-x}Gd_x$ alloy, the crystalline structure completely lose the periodicity when $x > 16$ as shown in Fig. 4.20 [124,125]. Their critical composition of 16% is the same as the critical composition of 17% in this study within the accuracy of the XPS measurement, which supports my assumption. The main claim in the discussion is that in the range of the amorphous structure, the image force model is able

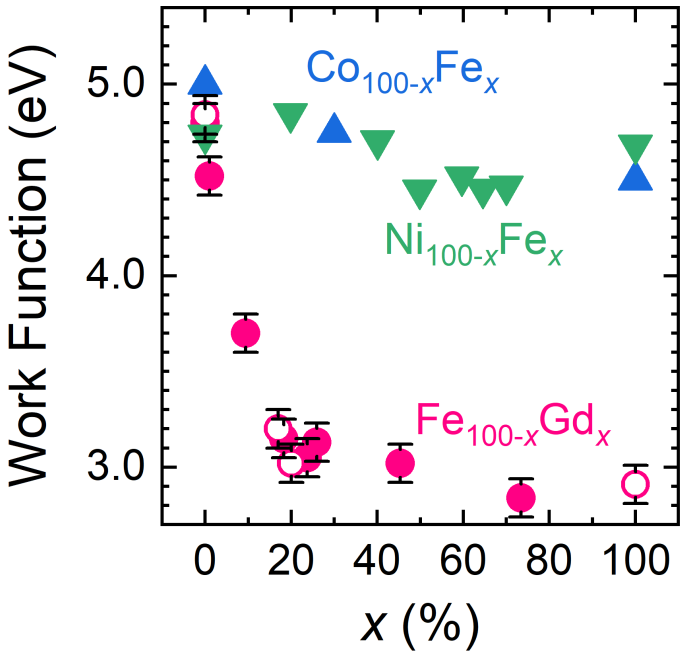

Figure 4.16: Comparison of work functions of ferromagnetic and ferrimagnetic alloys

The pink plots represent the work functions of FeGd alloys measured by this study. The filled and open circles are the results for the sample with artificially distributed composition ($0 < x < 100$) and the uniform samples (x=0, 17, 20, and 100 %), respectively. The blue and green plots represent the work functions of CoFe and NiFe alloys, respectively. The values of CoFe and NiFe alloy are quoted from [97,119], and Co and Fe are from [101].

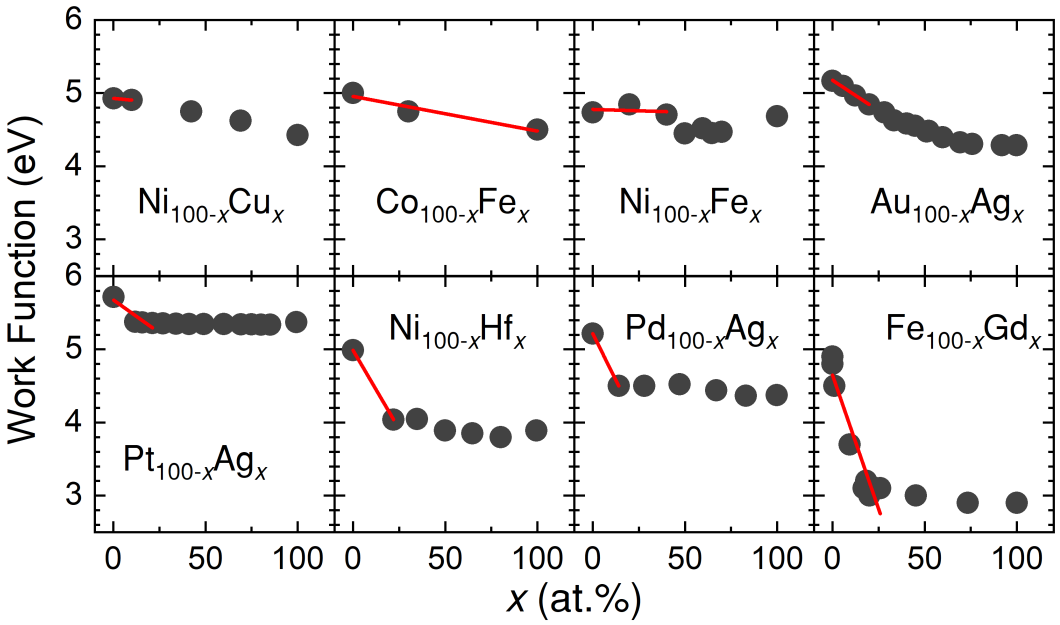

Figure 4.17: Linear fittings of work functions of alloys by their composition

The gray dots shows the reported values from each literatures and my experiment of FeGd. The plots of CoFe[119], NiFe[97], PtAu[120], NiCu[121], HfNi[96], PdAg[122] and AuAg[123] are quoted from the literatures. Red lines are fitting line with linear functions.

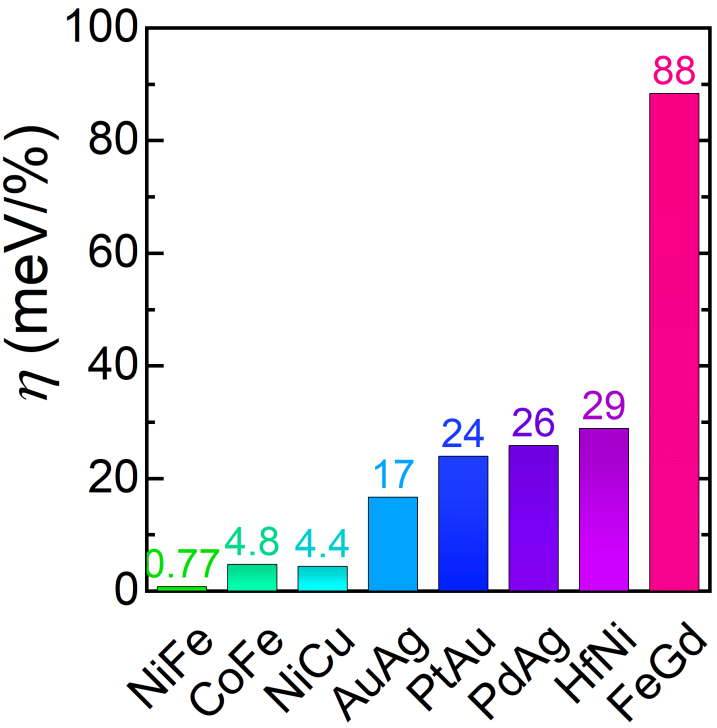

Figure 4.18: Comparison of the η among binary alloys

to predict the ϕ of the FeGd alloy if $U = 0.76$ is accepted, although a better understanding of U dependence on x is necessary.

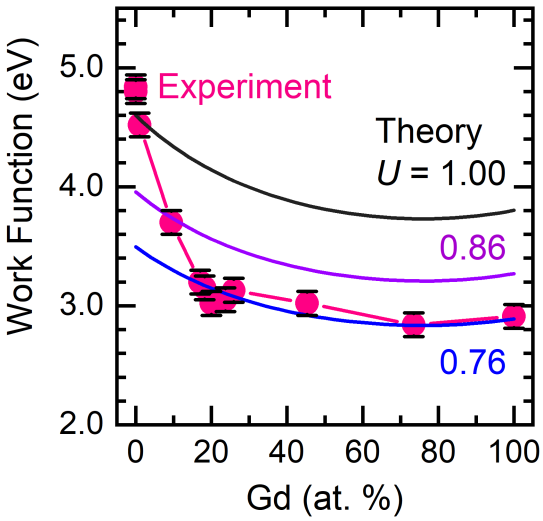

Figure 4.19: Comparison of measured work functions with theoretical models.

The black, purple and blue lines represent theoretical value of WF with U of 1.0, 0.86 and 0.76, respectively. The pink circles indicate the experimental results, and the pink lines are guide to eyes.

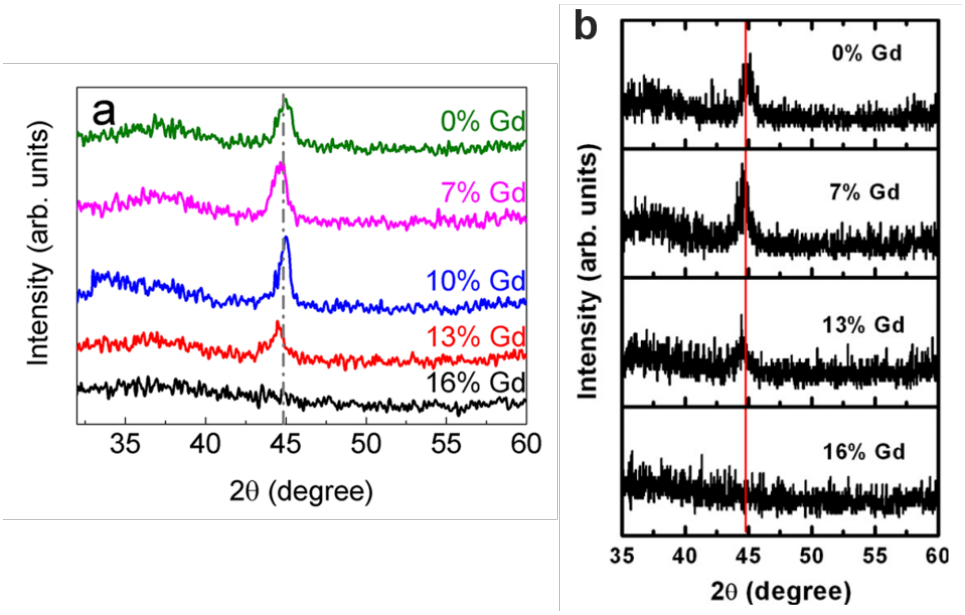

Figure 4.20: XRD spectra of $Fe_{100-x}Gd_x$ alloys.

The same results are reported in the previous studies: The peaks of 44°are detected in the samples of $x \leq 13\%$; No peaks are detected in the sample of $x = 16\%$. **(a)** is quoted from [124]. **(b)** is quoted from [125].

4.5 Summary

I developed a new method to make an ohmic contact on nondegenerate n-type Si with a ferrimagnetic metal. Just 20% of Gd atoms significantly decrease the work function of Fe from 4.9 eV to 3.0 eV, giving rise to an ohmic contact on n-Si with saving the spin polarization and the magnetization at 300K. The ohmic contact presents a small resistance by a factor of 100 comparing with that of Fe/n-Si. I also examined the validity of the image force model. The quantitative analysis of the surface compositions and the work functions supports the validity of the image force model; however, the change of U is possible by alloying, which is suggested by this study for the first time. Further theoretical and experimental studies are needed to understand the physics organizing the work function of amorphous alloy systems.

Chapter 5

Conclusion

The central goal of this project was to develop the technology to enhance the room temperature magnetoresistance ratio of Si-based spin devices to the level of 100%, which is equivalent to the R factor of 1.46 for the spin MOSFET based on Si. I developed three technologies to achieve the purpose: thermal annealing at 300°C, the spin-dependent Seebeck effect, and making an ohmic contact using an FeGd alloy. Their contribution to the enhancement of MR ratio is estimated as $\times 2$, $\times 1.2$, and $\times 100$, respectively. The state-of-the-art of MR ratio is 1.4%[22], so it will reach as much as 336% if these are integrated collectively. Considering the best G_e of 10^6 in Si-based lateral spin MOSFET[46], the R factor will reach 1.61, which satisfies the target of more than 1.46. The central goal was successfully achieved.

The technologies developed in the thesis are generally applicable for semiconductor-based spin devices. Thermal annealing enhances the texture of Fe/MgO structure, the spin-dependent Seebeck effect generates a spin current in nonmagnetic semiconductor, and the low work function of the $Fe_{80}Gd_{20}$ reduces the Schottky barrier or makes ohmic contact to an n-type semiconductor. I believe these findings contribute to the development of spintronic devices based on semiconductors that solve the heat issue in the evolution of electronics devices.

Here, I summarize each section.

Chapter 1. Introduction

I compared the state-of-the-arts of the spin MOSFETs and introduced a new figure of merit – R factor. The comparison proved the advantage of the Si-based lateral spin device quantitatively. I also showed the logical strategy to enhance the MR ratio.

Chapter 2. Effects of Thermal Annealing on Metal/Si Interfaces in Spin Devices

I discovered that the thermal annealing at 300°C increases the spin polarization at the metal/Si interface and the spin signal was enhanced by a factor of two. The enhancement is attributable to the well-textured structure of the ferromagnetic metal/MgO interface, which increases the contribution of the coherent tunneling to the total tunneling current. I also developed a thermally tolerant structure up to 400°C, which satisfies the requirement from the fabrication processes of electronic devices.

Chapter 3. Spin-dependent Seebeck Effect at Metal/Si Interfaces

I demonstrated the spin-dependent Seebeck effect for the first time using a semiconductor. The demonstration implies that Joule heating in the semiconductor can add a spin current in Si. By devising a Fourier analysis that includes the nonlinear I-V characteristics and the bias dependence of the spin polarization, I extracted the contribution of the spin-dependent Seebeck effect to the spin signal. As a result, a spin signal of 8 μV was obtained with Fe, which has the spin Seebeck coefficient of 6 μV/K under a realistic temperature difference of 200 mK at the metal/Si interface via the MgO tunneling barrier. I also found that the signal in the Si-based device was 400 times larger than that based on Cu due to its unique properties: the long spin diffusion length and the low electrical conductivity. Even with the conventional structure, it was estimated that 20% of the signals are caused by the Joule heating. The qualitative analysis exhibits the possibility of additional spin current in Si-based spin devices.

Chapter 4. Ohmic Contact on n-type Si with a Ferrimagnetic Metal

I developed a magnetic material to reduce the interfacial resistance by forming an ohmic contact on an n-type Si. $Fe_{80}Gd_{20}$ alloy was found to be a suitable material for Si-based spin devices. The work function of the alloy is 3.0 eV, which is 1.0 eV less than the electron affinity of Si enabling the ohmic contact without highly doped Si. The discovery shows the possibility of realizing a Si-based spin device by taking advantage of the long spin relaxation time, which is a feature of non-degenerate Si. In addition, ohmic contact reduced parasitic resistance by a factor of 100.

Finally, I consider the next challenge toward the application of Si-based spin devices. Three technologies stated in the thesis will remove the major object in the way to the application when they are combined with the other technologies developed in the previous studies [22,46]. The next challenge is the integration of the five technologies demonstrated separately: (i) the thin Si channel (15 nm) [46], (ii) the improvement of the spin relaxation time by introducing a strain in the Si channel [22], (iii) the coherent tunneling by well-textured ferromagnetic metal/MgO interface (chapter 2), (iv) using the SDSE (chapter 3), and (v) eliminating Schottky barrier using low-work function ferrimagnetic alloy (chapter 5). Most of these technologies may be compatible with each other except for (iii) and (v): a crystalline structure with 4-fold rotational symmetry is necessary to achieve coherent tunneling, whilst the low work function ferrimagnetic metal has an amorphous structure. The possible strategy is forming Laves phase on a MgO tunnel barrier. The C15 Laves phase has the 4-fold rotational symmetry providing the possibility of the spin-polarized Δ_1 band conduction, which is an open question. The computational study will examine the appearance and the spin polarization of the Δ_1 state. The experimental study will examine the feasibility of coherent tunneling.

References

[1] M. Haurylau, *et al.*, *IEEE Journal on Selected Topics in Quantum Electronics* **12**, 1699 (2006).

[2] Y. Shin, J. Seomun, K. M. Choi, T. Sakurai, *ACM Transactions on Design Automation of Electronic Systems* **15**, 28 (2010).

[3] K. Nomura, K. Abe, H. Yoda, S. Fujita, *Journal of Applied Physics* **111**, 07E330 (2012).

[4] S. Sugahara, M. Tanaka, *ACM Transactions on Storage* **2**, 197 (2006).

[5] I. Žutić, J. Fabian, S. Das Sarma, *Reviews of Modern Physics* **76**, 323 (2004).

[6] T. Valet, A. Fert, *Phys. Rev. B* **48**, 7099 (1993).

[7] Z. G. Yu, M. E. Flatté, *Physical Review B* **66**, 235302 (2002).

[8] Z. G. Yu, M. E. Flatté, *Physical Review B* **66**, 201202(R) (2002).

[9] S. O. Valenzuela, *International Journal of Modern Physics B* **23**, 2413 (2009).

[10] H. Idzuchi, Y. Fukuma, L. Wang, Y. Otani, *Applied Physics Letters* **101**, 022415 (2012).

[11] J. T. Batley, *et al.*, *Physical Review B* **92**, 220420(R) (2015).

[12] T. A. Peterson, *et al.*, *Physical Review B* **94**, 235309 (2016).

[13] F. J. Jedema, M. S. Nijboer, A. T. Filip, B. J. van Wees, *Physical Review B* **67**, 085319 (2003).

[14] S. Dushenko, *et al.*, *Physical Review Letters* **114**, 196602 (2015).

[15] S. Lee, *et al.*, *Applied Physics Letters* **110**, 192401 (2017).

[16] T. Sasaki, *et al.*, *Physical Review Applied* **2**, 034005 (2014).

[17] T. Tahara, *et al.*, *Applied Physics Express* **8**, 113004 (2015).

[18] M. N. Baibich, *et al.*, *Physical Review Letters* **61**, 2472 (1988).

[19] M. Julliere, *Physics Letters* **54**, 225 (1975).

[20] T. Miyazaki, N. Tezuka, N. T. T. Miyazaki, *Journal of Magnetism and Magnetic Materials* **139**, L231 (1995).

[21] J. S. Moodera, L. R. Kinder, T. M. Wong, R. Meservey, *Physical Review Letters* **74**, 3273 (1995).

[22] H. Koike, *et al.*, *Applied Physics Express* **13**, 083002 (2020).

[23] G. Schmidt, L. W. Molenkamp, A. T. Filip, B. J. van Wees, *Phys. Rev. B* **62**, R4790 (2000).

[24] R. Ohshima, *et al.*, *Applied Physics Letters* **110**, 182402 (2017).

[25] E. I. Rashba, *Physical Review B* **62**, R16267 (2000).

[26] T. Tahara, *et al.*, *Physical Review B* **93**, 214406 (2016).

[27] J. Mathon, A. Umerski, *Physical Review B* **63**, 220403 (2001).

[28] W. H. Butler, X. G. Zhang, T. C. Schulthess, J. M. MacLaren, *Physical Review B* **63**, 544161 (2001).

[29] S. Yuasa, D. D. Djayaprawira, *Journal of Physics D: Applied Physics* **40**, R337 (2007).

[30] S. Yuasa, T. Nagahama, A. Fukushima, Y. Suzuki, K. Ando, *Nature Materials* **3**, 868 (2004).

[31] S. S. Parkin, *et al.*, *Nature Materials* **3**, 862 (2004).

[32] T. Suzuki, *et al.*, *Applied Physics Express* **4**, 023003 (2011).

[33] T. Sasaki, *et al.*, *Applied Physics Letters* **98**, 262503 (2011).

[34] S. Lee, *et al.*, *Physical Review B* **99**, 064408 (2019).

[35] J. L. Cheng, M. W. Wu, J. Fabian, *Physical Review Letters* **104**, 016601 (2010).

[36] H. Dery, P. Dalal, Cywiński, L. J. Sham, *Nature* **447**, 573 (2007).

[37] S. C. Chang, S. Manipatruni, D. E. Nikonov, I. A. Young, A. Naeemi, *IEEE Transactions on Magnetics* **50**, 3400513 (2014).

[38] R. Ishihara, *et al.*, *Physical Review Applied* **13**, 044010 (2020).

[39] S. Sugahara, M. Tanaka, *Applied Physics Letters* **84**, 2307 (2004).

[40] H. Sugiyama, *et al.*, *Solid State Communications* **190**, 49 (2014).

[41] S. Sato, R. Nakane, T. Hada, M. Tanaka, *Physical Review B* **96**, 235204 (2017).

[42] T. Sasaki, *et al.*, *Applied Physics Letters* **104**, 052404 (2014).

[43] R. Nakane, T. Harada, K. Sugiura, M. Tanaka, *Japanese Journal of Applied Physics* **49**, 113001 (2010).

[44] T. Kanaki, H. Asahara, S. Ohya, M. Tanaka, *Applied Physics Letters* **107**, 242401 (2015).

[45] T. Kanaki, *et al.*, *Applied Physics Express* **12**, 023009 (2019).

[46] S. Sato, M. Ichihara, M. Tanaka, R. Nakane, *Physical Review B* **99**, 165301 (2019).

[47] H. Terada, S. Ohya, L. D. Anh, Y. Iwasa, M. Tanaka, *Scientific Reports* **7**, 5618 (2017).

[48] T. Kanaki, *et al.*, *Scientific Reports* **8**, 7195 (2018).

[49] R. C. Sousa, *et al.*, *Applied Physics Letters* **73**, 3288 (1998).

[50] W. G. Wang, *et al.*, *Physical Review B* **81**, 144406 (2010).

[51] T. Koike, M. Oogane, M. Tsunoda, Y. Ando, *Journal of Applied Physics* **127**, 085306 (2020).

[52] A. Tiwari, *et al.*, *AIP Advances* **6**, 075119 (2016).

[53] S. Lee, *et al.*, *Applied Physics Letters* **116**, 022403 (2020).

[54] F. J. Jedema, A. T. Filip, B. J. van Wees, *Nature* **410**, 345 (2001).

[55] N. Yamashita, *et al.*, *AIP Advances* **10**, 095021 (2020).

[56] T. Sasaki, *et al.*, *Applied Physics Letters* **96**, 122101 (2010).

[57] A. Tiwari, *et al.*, *Japanese Journal of Applied Physics* **56**, 04CD05 (2017).

[58] N. Yamashita, *et al.*, *Scientific Reports* **11**, 10583 (2021).

[59] Minho O, M. Kajihara, *Materials Transactions* **52**, 677 (2011).

[60] K. Holloway, P. M. Fryer, *Applied Physics Letters* **57**, 1736 (1990).

[61] E. Sugawara, H. Nikaido, *Antimicrobial agents and chemotherapy* **58**, 7250 (2014).

[62] Y. Tserkovnyak, A. Brataas, G. E. Bauer, *Physical Review Letters* **88**, 117601 (2002).

[63] S. A. Crooker, *et al.*, *Science* **309**, 2191 (2005).

[64] A. Slachter, F. L. Bakker, J.-P. P. Adam, B. J. van Wees, *Nature Physics* **6**, 879 (2010).

[65] L. Gravier, S. Serrano-Guisan, F. Reuse, J.-P. Ansermet, *Physical Review B* **73**, 052410 (2006).

[66] M. Hatami, G. E. W. Bauer, Q. Zhang, P. J. Kelly, *Physical Review Letters* **99**, 066603 (2007).

[67] K. Uchida, *et al.*, *Nature* **455**, 778 (2008).

[68] K. I. Uchida, *et al.*, *Applied Physics Letters* **97**, 172505 (2010).

[69] J. Flipse, F. L. Bakker, A. Slachter, F. K. Dejene, B. J. van Wees, *Nature Nanotechnology* **7**, 166 (2012).

[70] F. K. Dejene, J. Flipse, G. E. W. Bauer, B. J. van Wees, *Nature Physics* **9**, 636 (2013).

[71] S. Hu, H. Itoh, T. Kimura, *NPG Asia Materials* **6**, e127 (2014).

[72] A. Hojem, D. Wesenberg, B. L. Zink, *Physical Review B* **94**, 024426 (2016).

[73] J.-C. C. Le Breton, S. Sharma, H. Saito, S. Yuasa, R. Jansen, *Nature* **475**, 82 (2011).

[74] Y. Aoki, *et al.*, *Physical Review B* **86**, 081201 (2012).

[75] T. Uemura, K. Kondo, J. Fujisawa, K. I. Matsuda, M. Yamamoto, *Applied Physics Letters* **101**, 132411 (2012).

[76] O. Txoperena, *et al.*, *Applied Physics Letters* **102**, 192406 (2013).

[77] H. N. Tinkey, P. Li, I. Appelbaum, *Applied Physics Letters* **104**, 232410 (2014).

[78] O. Txoperena, *et al.*, *Physical Review Letters* **113**, 146601 (2014).

[79] H. Inoue, *et al.*, *Physical Review X* **5**, 041023 (2015).

[80] I. Appelbaum, H. N. Tinkey, P. Li, *Physical Review B* **90**, 220402(R) (2014).

[81] S. V. Karthik, T. M. Nakatani, A. Rajanikanth, Y. K. Takahashi, K. Hono, *Journal of Applied Physics* **105**, 07C916 (2009).

[82] W. Fulkerson, J. P. Moore, D. L. McElroy, *Journal of Applied Physics* **37**, 2639 (1966).

[83] J. Bass, W. P. Jr, *Journal of Physics: Condensed Matter* **19**, 183201 (2007).

[84] A. A. Tulapurkar, Y. Suzuki, *Solid State Communications* **150**, 466 (2010).

[85] A. Fert, H. Jaffrès, *Physical Review B* **64**, 184420 (2001).

[86] A. N. Chantis, D. L. Smith, *Physical Review B* **78**, 235317 (2008).

[87] X. Lou, *et al.*, *Nature Physics* **3**, 197 (2007).

[88] M. Shiraishi, *et al.*, *Physical Review B* **83**, 241204 (2011).

[89] S. O. Valenzuela, D. J. Monsma, C. M. Marcus, V. Narayanamurti, M. Tinkham, *Physical Review Letters* **94**, 196601 (2005).

[90] M. Kameno, *et al.*, *Applied Physics Letters* **104**, 092409 (2014).

[91] S. Sato, M. Tanaka, R. Nakane, *Physical Review B* **102**, 035305 (2020).

[92] S. Sze, *Semiconductor Devices: Physics and Technology* (John Wiley & Sons Singapore Pte. Limited, 2012).

[93] R. T. Tung, *Applied Physics Reviews* **1**, 011304 (2014).

[94] B. C. Min, K. Motohashi, C. Lodder, R. Jansen, *Nature Materials* **5**, 817 (2006).

[95] N. D. Orf, I. D. Baikie, O. Shapira, Y. Fink, *Applied Physics Letters* **94**, 113504 (2009).

[96] J. A. Rothschild, *et al.*, *Journal of Applied Physics* **112**, 013717 (2012).

[97] S. Saito, T. Maeda, *Vacuum* **24**, 220 (1981).

[98] T. Arizumi, M. Hirose, N. Altaf, *Japanese Journal of Applied Physics* **7**, 870 (1968).

[99] T. Arizumi, M. Hirose, N. Altaf, *Japanese Journal of Applied Physics* **8**, 1310 (1969).

[100] E. Stoner, *Proceedings of the royal society A* **165**, 372 (1938).

[101] H. B. Michaelson, *Journal of Applied Physics* **48**, 4729 (1977).

[102] G. Hua, D. Li, *Applied Physics Letters* **99**, 041907 (2011).

[103] H. Lu, X. Huang, D. Li, *Journal of Applied Physics* **116**, 173506 (2014).

[104] C. G. Vayenas, S. Bebelis, S. Ladas, *Nature* **343**, 625 (1990).

[105] J. Bardeen, *Physical Review* **49**, 653 (1936).

[106] E. Wigner, J. Bardeen, *Physical Review* **48**, 84 (1935).

[107] N. D. Lang, W. Kohn, *Physical Review B* **3**, 1215 (1971).

[108] H. L. Skriver, N. M. Rosengaard, *Physical Review B* **46**, 7157 (1992).

[109] J. R. Smith, *Physical Review* **181**, 522 (1969).

[110] N. D. Lang, W. Kohn, *Physical Review B* **1**, 4555 (1970).

[111] M. Methfessel, D. Hennig, M. Scheffler, *Physical Review B* **46**, 4816 (1992).

[112] I. Brodie, *Physical Review B* **51**, 13660 (1995).

[113] S. Halas, T. Durakiewicz, *Journal of Physics: Condensed Matter* **10**, 10815 (1998).

[114] J. A. Rothschild, M. Eizenberg, *Physical Review B* **81**, 224201 (2010).

[115] N. W. Ashcroft, N. D. Mermin, *Solid State Physics* (Holt-Saunders, 1976).

[116] C. Kittel, *Introduction to Solid State Physics* (Wiley, 2004), 8th edn.

[117] D. Eagles, *Journal of Magnetism and Magnetic Materials* **28**, 117 (1982).

[118] B. Anderson, R. Anderson, *Fundamentals of Semiconductor Devices* (McGraw-Hill, Inc., USA, 2004).

[119] K. R. Jeon, *et al.*, *Physical Review B* **84**, 165315 (2011).

[120] R. Bouwman, W. M. H. Sachtler, *Journal of Catalysis* **140**, 127 (1970).

[121] W. Sachter, G. J. H. Dorgelo, *Journal of Catalysis* **4**, 654 (1965).

[122] R. Bouwman, G. J. Lippits, W. M. Sachtler, *Journal of Catalysis* **25**, 350 (1972).

[123] S. C. Fain, J. M. McDavid, *Physical Review B* **9**, 5099 (1974).

[124] A. You, *et al.*, *AIP Advances* **7**, 056029 (2017).

[125] W. Zhang, *et al.*, *Journal of Applied Physics* **115**, 17A308 (2014).

[126] S. Takahashi, S. Maekawa, *Physical Review B* **67**, 052409 (2003).

[127] T. Sasaki, *et al.*, *Applied Physics Express* **2**, 053003 (2009).

Appendix A

Basic Theory of Spin Current in Semiconductors

Here, I describe the basic theory of spin current in semiconductors, which is often used in the main text. Valet and Fert proposed the theory of spin transport 1993 [6]. Takahashi and Maekawa deduced measurable spin accumulation voltage covering spin injection and detection in the spin-valve structure [126], which are the basic theory in this section.

A.1 Charge and Spin Currents

Charge current J^{charge} is driven by drift and diffusion of electrons with both spins. J^{charge} can be written by using current of electron J_s with spin $s(s =\uparrow (\downarrow)$ means up(down)spin), an electrical field $\boldsymbol{E}$, and diffusion constant D_s:

$$\begin{aligned} J^{\text{charge}} &= \sum_{s=\pm 1} \left\{ J_s^{\text{drift}} + J_s^{\text{diffusion}} \right\} \\ &= \sum_{s=\pm 1} \{\sigma_s \boldsymbol{E} + eD_s \nabla n_s\} \\ &= \sum_{s=\pm 1} \{-\sigma_s \nabla \phi + eD_s \nabla n_s\}, \end{aligned} \tag{A.1}$$

where, e is elemental charge, n_s is charge density. Drude model describes an electrical conductivityσ_s as $\sigma_s = e^2 n_s \tau_s / m_s^*$ with momentum relaxation time τ_s and effective mass m_s^*. By applying Einsteins

relations, the conductivity of spin s at the Fermi level is written as:

$$\sigma_s = N_s e^2 D_s. \tag{A.2}$$

Using chemical potential μ_s, and Eq.(A.1), we obtain

$$\nabla n_s = N_s \mathrm{grad} \mu_s.$$

Then, with the electrochemical potential $\overline{\mu}_s = \mu_s - e\phi$, J_s is written as:

$$J_s = \frac{\sigma_s}{e} \nabla \overline{\mu}_s. \tag{A.3}$$

Using the Eq.(A.3), J^{spin} and J^{charge} are written as:

$$\begin{aligned} J^{\mathrm{charge}} &= J_\uparrow + J_\downarrow \\ &= \frac{1}{e} \nabla (\sigma_\uparrow \overline{\mu}_\uparrow + \sigma_\downarrow \overline{\mu}_\downarrow), \end{aligned} \tag{A.4}$$

$$\begin{aligned} J^{\mathrm{spin}} &= -\frac{\hbar}{2e^2} (J_\uparrow - J_\downarrow) \\ &= -\frac{\hbar}{2e^2} \nabla (\sigma_\uparrow \overline{\mu}_\uparrow - \sigma_\downarrow \overline{\mu}_\downarrow), \end{aligned} \tag{A.5}$$

The Eq. (A.4) tells that we can measure the average of the electrochemical potential biased by the conductivity of each spins as a electric voltage. In nonmagentic metals the conductivity of both spins are same, $\sigma_\uparrow = \sigma_\downarrow$, so the difference in the electrochemical potential of both spins $\overline{\mu}_\uparrow - \overline{\mu}_\downarrow$ (called spin voltage) drives spin currents, which is similar to electric voltage drives charge current.

A.2 Spin Accumuration at Interfaces

The spin currents are measurable when converted to another physical value including voltage. The spin accumulation voltage is made by spin currents at a ferromagnet/nonmagnet interface. I explain the mechanism to detect spin accumulation voltage and spin currents.

Figure A.1 shows the density of states of each spin. The density of states of each spin is different in ferromagnets (Fig. A.1b), whilst they are the same in the nonmagnetic materials (Fig. A.1a). The major spins are referer to as up, and the minor spins are referred to as down in the ferromagnet. The exchange interaction makes spins in the same direction: the spin polarization of electron allows a finite magnetic moment and spin current.

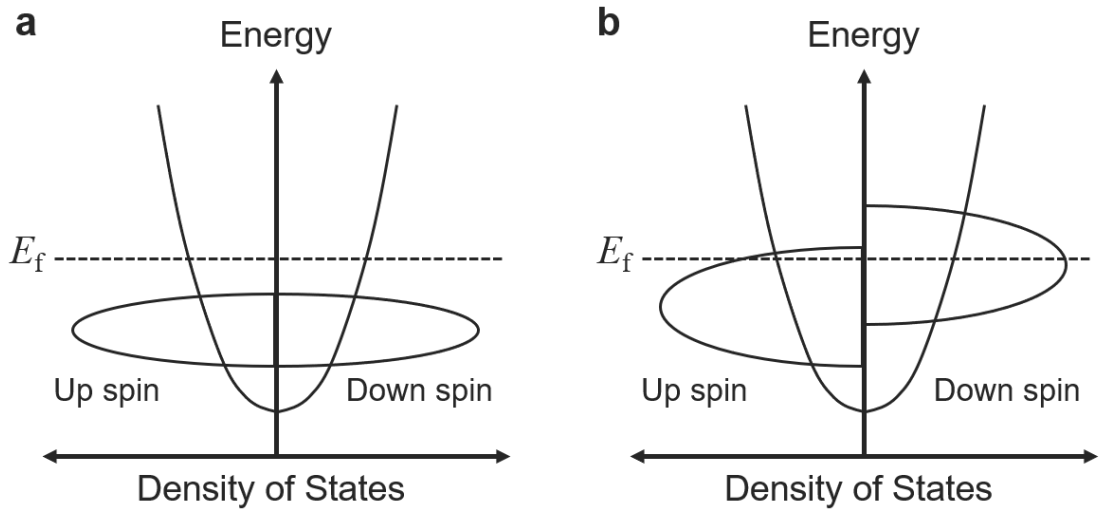

Figure A.1: Density of states of electrons

(a) Density of states of a nonmagnetic material **(b)** Density of states of a ferromagnetic metal.

The model of spin injection based on one-dimentional model is shown in Fig. A.2 involving ferromagnet (F)/nonmagnet(N) contact at $x = 0$. The electrochemical potential distributes as shown in Fig. A.3. The Drude model describe the conductivity σ as $\sigma = en\mu$ using the electronic density n, the mobilityμ, and elemental charge e. In a ferromagnet, σ depends on the spin because of the different n of each spins. I describe the conductivity provided by up and down spins as $\sigma_\uparrow$, $\sigma_\downarrow$. Then, the average of electrochemical potential in the ferromagnet is $\overline{\mu}_{\text{average}}$, which is expressed as:

$$\overline{\mu}_{\text{average}} = \frac{\sigma_\uparrow \overline{\mu}_\uparrow + \sigma_\downarrow \overline{\mu}_\downarrow}{\sigma_\uparrow + \sigma_\downarrow}.$$

As shown in Fig. A.3, $\overline{\mu}_{\text{average}}$ is inverted ratio of the $\sigma_\uparrow$ and $\sigma_\downarrow$ in the ferromagnet. $\overline{\mu}_{\text{average}}$ is the

centor of the $\sigma_\uparrow$ and $\sigma_\downarrow$ in the nonmagnet.

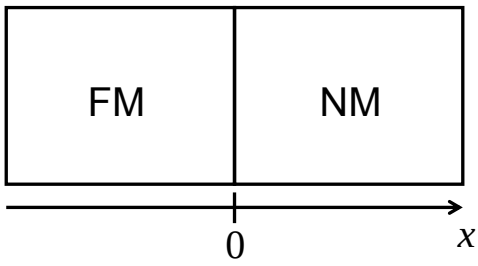

Figure A.2: One-dimentional model of FM/NM interface.

When electrons are injected from the ferromagnet to the nonmagnet by applying an electronic field. The field tilts whole the electrochemical potential. Because the spin polarization of the ferromagnet is non-zero $\alpha \equiv (\sigma_\uparrow - \sigma_\downarrow)/(\sigma_\uparrow + \sigma_\downarrow) > 0$, the density of the injected electron is also polarized: up spins are injected more than down spin. The spin polarization splits μ into two, so $\overline{\mu}_\uparrow - \overline{\mu}_\downarrow > 0$. The spin voltage drives spin current $J^{\rm spin}$ in nonmagnet. $J^{\rm spin}$ decreases exponentially in the length scale of spin diffusion length $\lambda_{\rm sf}$. $\overline{\mu}$ of each spins continue at the interface of ferromagnet and nonmagnet $x = 0$. The continuous condition splits$\overline{\mu}$ in the ferromagnet ($x < 0$) then, $\overline{\mu}_\uparrow - \overline{\mu}_\downarrow > 0$. As a result, $\overline{\mu}_{\rm average}$ are different at $x < 0$ and $x > 0$. Thus, spin injection from ferromagnet to nonmagnet make the difference $-eD$ in $\overline{\mu}_{\rm average}$. The difference is the spin accumulation voltage.

In case of the spin extraction, the profile of $\overline{\mu}$ is shown schematically in Fig. A.4. The extracted electrons from nonmagnet to ferromagnet have also spin polarization because the density of states are polarized in ferromagnet. The up spins extracted more than the down spins. The down spin remains more than up spin in the nonmagnet, so $\overline{\mu}_\uparrow - \overline{\mu}_\downarrow < 0$ ($x > 0$). Similar to the spin injection, the continuous conditions at $x = 0$ split $\overline{\mu}$ in the ferromagnet. Thus, spin extraction also make spin accumulation voltage $-eD$. Thus, spin injection and extraction produce measurable spin accumulation voltage.

I explain the spin transport in ferromagnet/nonmagnet/ferromagnet structure. Up and down spins are defined as the major and down spins, respectively, in the ferromagnet at the side of injection. Fig-

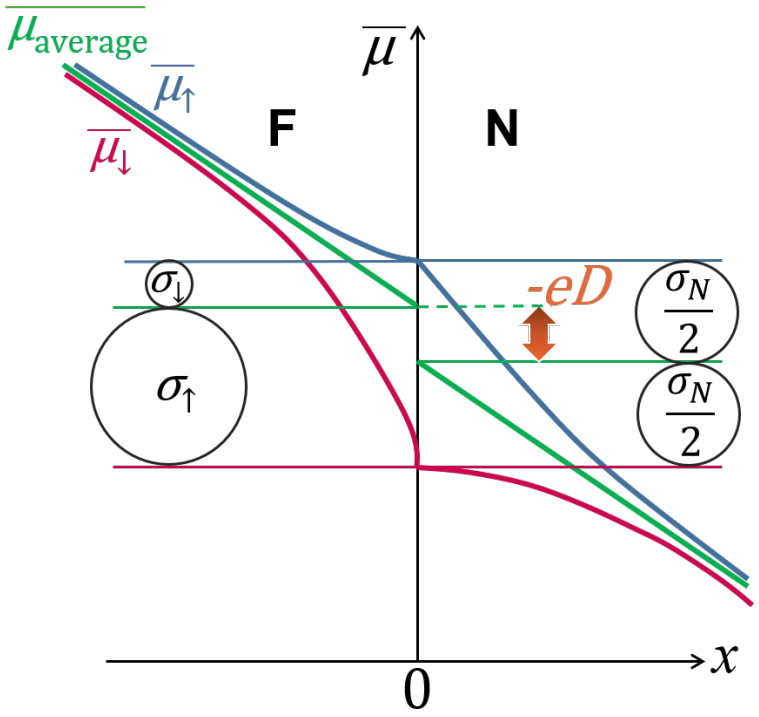

Figure A.3: Profile of electrochemical potential at the FM/NM interface in the case of spin injection.

The x-axis is space position, and y-axis is electrochemical potential. The red, blue, and green lines represents the electrochemicalpotential of up spin, down spin, and the average, respectively.

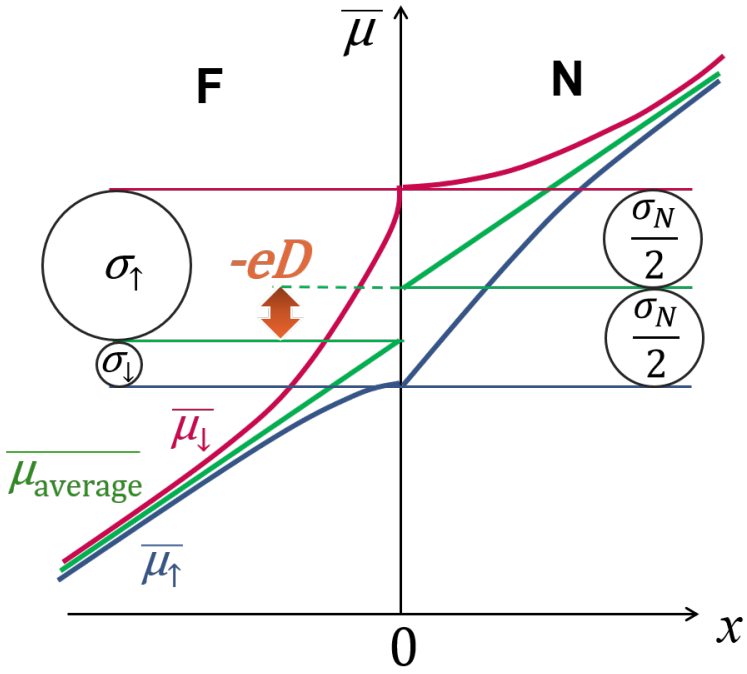

Figure A.4: Profile of electrochemical potential at the FM/NM interface in the case of spin extraction.

ures A.6a and A.6b represent profiles of $\overline{\mu}$s in the states of parallel (the magnetization of ferromagnets aligns the same direction) and antiparallel (the magnetization of ferromagnets align the opposite directions each other). The length scale of the N is smaller than its $\lambda_{\rm sf}$. The spin accumulation voltages affect each other at the spin injection and extraction. This is the spin transport: the spin-polarized electrons propagate along the nonmagnet. The spin accumulation voltages depend on the states of the ferromagnets' magnetization. The spin accumulation voltage at the extraction side is referred to as $D^{\rm P}$ (Parallel) and $D^{\rm AP}$ (AntiParallel). The difference $D^{\rm P} - D^{\rm AP}$ can be measured electrically and investigate the spin-related phenomena in materials.

A.3 Spin Diffusion Equation

I explain the spin diffusion equation[6]. Generally, the spin voltage $\overline{\mu}_\uparrow - \overline{\mu}_\downarrow$ decrease in the scale of the spin diffusion length $\lambda_{\rm sf}$ in a material, which is expressed as:

$$\Delta(\overline{\mu}_\uparrow - \overline{\mu}_\downarrow) = \frac{\overline{\mu}_\uparrow - \overline{\mu}_\downarrow}{\lambda_{\rm sf}^2}. \tag{A.6}$$

This is refered to as spin diffusion equation. The following are the charge conservation:

$$\Delta\left(\sigma_\uparrow \overline{\mu}_\uparrow + \sigma_\downarrow \overline{\mu}_\downarrow\right) = 0, \tag{A.7}$$

Starting from Eqs.(A.6) and (A.7), I deduce $\overline{\mu}$ in the case of Fig. A.2. Assume the conductivity of the ferromagnet is sum of the both spins $\sigma_{\rm F} = \sigma_{\rm F\uparrow} + \sigma_{\rm F\downarrow}$. In the ferromagnet ($x < 0$), Eqs. (A.6) and (A.7) provide following expression:

$$\sigma_{\rm F\uparrow}\overline{\mu}_\uparrow + \sigma_{\rm F\downarrow}\overline{\mu}_\downarrow = a_{\rm F}x + b_{\rm F}.$$

By solving with $\overline{\mu}_\uparrow$ and $\overline{\mu}_\downarrow$, we obtain:

$$\overline{\mu}_\uparrow = \frac{1}{\sigma_{\rm F}}(a_{\rm F}x + b_{\rm F} + \sigma_{\rm F\downarrow}A_{\rm F}e^{\frac{x}{\lambda_{\rm F}}}),$$

$$\overline{\mu}_\downarrow = \frac{1}{\sigma_{\rm F}}(a_{\rm F}x + b_{\rm F} - \sigma_{\rm F\uparrow}A_{\rm F}e^{\frac{x}{\lambda_{\rm F}}}),$$

where λ_{F} is the spin diffusion length of the ferromanet. a_{F}, b_{F}, A_{F} are constant values. Assume the conductivity of the nonmagnet is $\sigma_{\mathrm{N}} = 2\sigma_{\mathrm{N0}}$, then we obtain:

$$\overline{\mu}_{\uparrow} = \frac{1}{\sigma_{\mathrm{N}}}(a_{\mathrm{N}}x + b_{\mathrm{N}} + \sigma_{\mathrm{N0}}A_{\mathrm{N}}e^{-\frac{x}{\lambda_{\mathrm{N}}}}),$$

$$\overline{\mu}_{\downarrow} = \frac{1}{\sigma_{\mathrm{N}}}(a_{\mathrm{N}}x + b_{\mathrm{N}} - \sigma_{\mathrm{N0}}A_{\mathrm{N}}e^{-\frac{x}{\lambda_{\mathrm{N}}}}),$$

in the nonmagnet ($x > 0$), where λ_{N} is spin diffusion length of the nonmagnet, and a_{N}, b_{N}, and A_{N} are constant values. According to the condition of continuity of $\overline{\mu}_s$ and J_s, we obtain the following equations:

$$\overline{\mu}_{\uparrow}|_{x=0} = \frac{1}{\sigma_{\mathrm{F}}}(b_{\mathrm{F}} + \sigma_{\mathrm{F}\downarrow}A_{\mathrm{F}}) = \frac{1}{\sigma_{\mathrm{N}}}(b_{\mathrm{F}} + \sigma_{\mathrm{N0}}A_{\mathrm{N}}), \tag{A.8}$$

$$\overline{\mu}_{\downarrow}|_{x=0} = \frac{1}{\sigma_{\mathrm{F}}}(b_{\mathrm{F}} - \sigma_{\mathrm{F}\uparrow}A_{\mathrm{F}}) = \frac{1}{\sigma_{\mathrm{N}}}(b_{\mathrm{F}} - \sigma_{\mathrm{N0}}A_{\mathrm{N}}), \tag{A.9}$$

$$J_{\uparrow}|_{x=0} = \frac{\sigma_{\mathrm{F}\uparrow}}{e}\frac{1}{\sigma_{\mathrm{F}}}\left(a_{\mathrm{F}} + \frac{\sigma_{\mathrm{F}\downarrow}A_{\mathrm{F}}}{\lambda_{\mathrm{F}}}\right) = \frac{\sigma_{\mathrm{N0}}}{e}\frac{1}{\sigma_{\mathrm{N}}}, \tag{A.10}$$

$$J_{\downarrow}|_{x=0} = \frac{\sigma_{\mathrm{F}\uparrow}}{e}\frac{1}{\sigma_{\mathrm{F}}}\left(a_{\mathrm{F}} - \frac{\sigma_{\mathrm{F}\downarrow}A_{\mathrm{F}}}{\lambda_{\mathrm{F}}}\right) = \frac{\sigma_{\mathrm{N0}}}{e}\frac{1}{\sigma_{\mathrm{N}}}\left(a_{\mathrm{N}} + \frac{\sigma_{\mathrm{N0}}A_{\mathrm{N}}}{\lambda_{\mathrm{N}}}\right), \tag{A.11}$$

Generally, using constants A, B, C, a, and b, the electrochemical potentials in each spins are expressed as:

- Ferromagnet

$$\overline{\mu}_S = \frac{A}{\sigma_s}e^{-\frac{x}{\lambda_{\mathrm{F}}}} + Bx + C, \tag{A.12}$$

- Nonmagnet

$$\overline{\mu}_S = \frac{a}{\sigma_s}e^{-\frac{x}{\lambda_{\mathrm{N}}}} + bx, \tag{A.13}$$

A.4 Conductance Mismatch

Schmidt *et al.*, stated a fundamental obstacle named "conductance mismatch" in 2000 [23] that hampers the spin injection and the transport in semiconductors. The spins are relected at the metal/semiconductor interface because the most ferromagnets has larger conductivity than semiconductors. The obstacle was solved by Rashba in the same year [25]. He suggested to insert tunnel contacts to increase the

interfacial resistance to avoid the backflow of injected spins in the semiconductor. The samples prepared in the chapter have tunnel barrier at the interface to avoid conductance mismatch, which is explained here.

Spin polarization is defined as $\alpha = (\sigma_{F\uparrow} - \sigma_{F\downarrow})/(\sigma_{F\uparrow} + \sigma_{F\downarrow})$ and spin resistance of F and N as:

$$\frac{1}{\lambda_F}\frac{4\sigma_{F\uparrow}\sigma_{F\downarrow}}{\sigma_{F\uparrow}+\sigma_{F\downarrow}} = \frac{1}{r_F},$$

$$\frac{2\sigma_{N0}}{\lambda_N} = \frac{\sigma_N}{\lambda_N} = \frac{1}{r_N},$$

then the spin current are written as:

$$J_\uparrow - J_\downarrow = \alpha J + \frac{A_F}{e}\frac{1}{2r_F}. \tag{A.14}$$

Then, the spin polarization of the current in the nonmagnet is expressed as:

$$\beta = \frac{J_\uparrow - J_\downarrow}{J_\uparrow + J_\downarrow} = \alpha\left(1 - \frac{r_N}{r_F}\right)^{-1}, \tag{A.15}$$

From Eq. A.15, β depends on the ratio of the spin resistance in the F and the N. Usually ferromagnetic metals are applied to the source of spins, have higher conductivity by orders than semiconductors, and have smaller spin resistance by orders than Si. This means $r_N \gg r_F$ and the right side of Eq.(A.15) becomes zero. The spin current disappears in this case – the conductance mismatch [23].

Tunnel barrier treats the conductance mismatch [25,85]. By including an interfacial resistance of the tunnel barrier and reconsidering the condition of continuity at $x = 0$, Eqs. (A.8) and (A.9) are rewritten as:

$$\overline{\mu}_\uparrow|_{x=0} = \frac{1}{\sigma_F}(b_F + \sigma_{F\downarrow}A_F) + r_{i\uparrow}eJ_\uparrow = \frac{1}{\sigma_N}(b_F + \sigma_{N0}A_N). \tag{A.16}$$

$$\overline{\mu}_\downarrow|_{x=0} = \frac{1}{\sigma_F}(b_F - \sigma_{F\uparrow}A_F) + r_{i\downarrow}eJ_\downarrow = \frac{1}{\sigma_N}(b_F - \sigma_{N0}A_N), \tag{A.17}$$

where, $r_{i\uparrow}$ and $r_{i\downarrow}$ are the interface resistance of the tunnel barrier of up and down spins, respectively. Here I define the resistance r_i and the spin polarization at the interface γ as:

$$r_i = \frac{1}{4}(r_{i\uparrow} + r_{i\downarrow}).$$

$$\gamma = \frac{r_{\mathrm{i}\uparrow}^{-1} - r_{\mathrm{i}\downarrow}^{-1}}{r_{\mathrm{i}\uparrow}^{-1} + r_{\mathrm{i}\downarrow}^{-1}}.$$

By applying Eqs.(A.10) and (A.10), the spin polarization of the current in the nonmagnet is expressed as:

$$\beta = \frac{J_\uparrow - J_\downarrow}{J_\uparrow + J_\downarrow} = \frac{r_{\mathrm{F}} + r_{\mathrm{i}}\gamma}{r_{\mathrm{F}} + r_{\mathrm{N}} + r_{\mathrm{i}}}. \tag{A.18}$$

According to Eq.(A.18), in the case of $r_{\mathrm{N}} \gg r_{\mathrm{F}}$, if $r_{\mathrm{i}} \gg r_{\mathrm{F}}$ then, $J_\uparrow - J_\downarrow \neq 0$; spin current flows in the semiconuctor. Sasaki *et al.* reported electrical spin injection and spin transport in Si-based lateral spin valve structure using tunnel barrier made of MgO in 2009 [127]. Eq.(A.18) and the results means that in MgO tunnel barrier, the resistance have spin polarization $\gamma \neq 0$ and $r_{\mathrm{i}\uparrow} \neq r_{\mathrm{i}\downarrow}$. Thus, tunnel barrier allows us to make spin currents in Si so far. I prepared and measured the lateral spin valves including tunnel barrer of MgO.

A.5 Spindrift

The spin resistance in the N is proportional to the spin diffusion length. In semiconuctor, the drift of electrons drives spin currents when an electric field is applied, which transports spins much farther than the original spin diffusion length [7,8]. This effect is refered to as spin drift effect and investigated experimentally [15,16,26,46,53,90]. Here, I explain how the spin drift effect affects the spin diffusion length [7,8]. I write electron densities of the up and down spins as $n_\uparrow$ and $n_\downarrow$, the spin diffusion equation (A.6) is transformed to the spin drift equation including the drift term involved by the electric field $\boldsymbol{E}$ as:

$$\nabla^2(n_\uparrow - n_\downarrow) + \frac{e\boldsymbol{E}}{k_{\mathrm{B}}T}\nabla(n_\uparrow - n_\downarrow) - \frac{(n_\uparrow - n_\downarrow)}{\lambda_{\mathrm{N}}^2} = 0, \tag{A.19}$$

where, $k_{\mathrm{B}}$is Boltzmann constant and T is temperature. By using the solution of the characteristic equation x, we obtain:

$$x = -\frac{-e\boldsymbol{E}}{2k_{\mathrm{B}}T} \pm \frac{1}{2}\sqrt{\left(\frac{|e\boldsymbol{E}|}{k_{\mathrm{B}}T}\right)^2 + \frac{4}{\lambda_{\mathrm{N}}^2}}. \tag{A.20}$$

Then, using constants A_1 and A_2, the general solutions of eq.(A.19) is written as:

$$n_\uparrow - n_\downarrow = A_1 e^{-\frac{z}{\lambda_{\mathrm{d}}}} + A_2 e^{-\frac{z}{\lambda_{\mathrm{u}}}}, \tag{A.21}$$

where, $\lambda_{\rm d}$ and $\lambda_{\rm u}$ are the down and up stream spin transport length. Eq.(A.20) expresses the spin transport length of both stream as:

$$\lambda_{\rm d} = \left\{ -\frac{|e\boldsymbol{E}|}{2k_{\rm B}T} + \sqrt{\left(\frac{|e\boldsymbol{E}|}{k_{\rm B}T}\right)^2 + \frac{1}{\lambda_{\rm N}^2}} \right\}^{-1}, \tag{A.22}$$

$$\lambda_{\rm u} = \left\{ \frac{|e\boldsymbol{E}|}{2k_{\rm B}T} + \sqrt{\left(\frac{|e\boldsymbol{E}|}{k_{\rm B}T}\right)^2 + \frac{1}{\lambda_{\rm N}^2}} \right\}^{-1}. \tag{A.23}$$

Thus, the electric field modifies the spin diffusion length. Figure A.5 shows the profile of the spin coherence with and without spin drift effect [7,8]. The down stream flow transports spins further than the diffusive current along with the electric field.

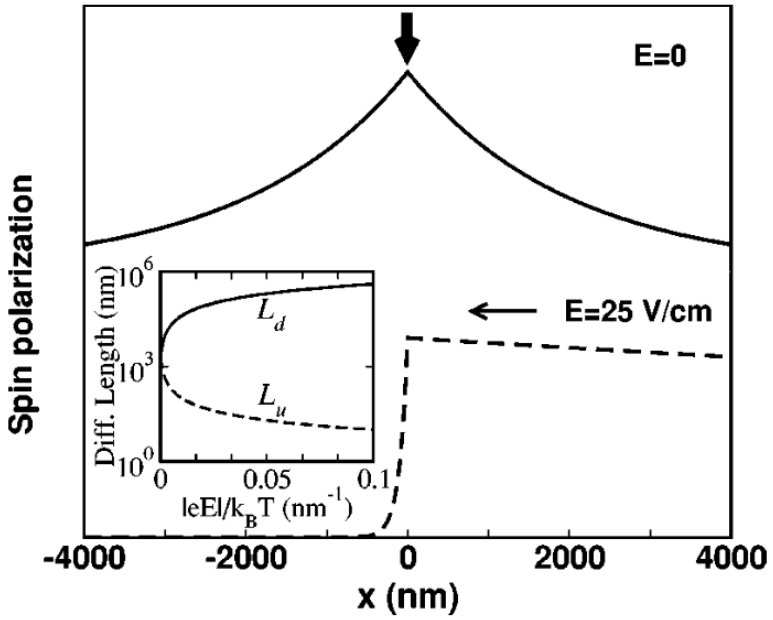

Figure A.5: Effect of electric field on the spin transport.
The figure is quoted from [8].

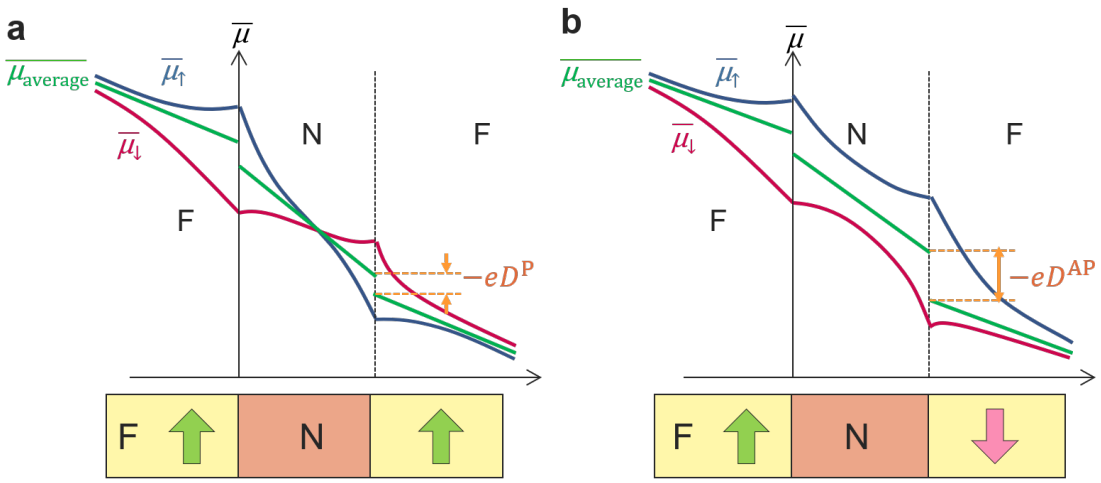

Figure A.6: Profile of electrochemical potential while spin transports in the nonmagnets. **(a)** Parallel state **(b)** Antiparallel state

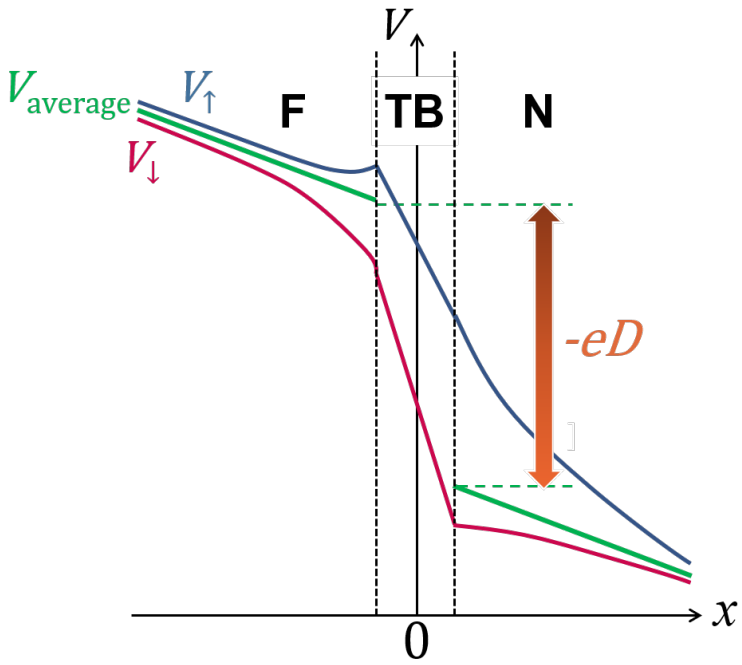

Figure A.7: Profile of electrochemical potential at the interface of ferromagnet/nonmagnet considering interfacial resistance.

A.6 The Requirement of the Interface Resistance for the Future Spin MOSFET

Here, I state the effectiveness of a small interface resistance of ferromagnetic electrode by considering the future spin MOSFETs with a short channel length, which consists of semiconductor channel (SC) and ferromagnetic electrodes (FM), as schematically shown in Fig. A.8a. The magnetoresistance (MR) ratio, G_e, is calculated by assuming the one-directional model of the lateral spin valve as shown in Figs. A.8b and A.8c. The spin signal, i.e., the spin-dependent voltage between F1 and F2, $\Delta V_{2\mathrm{T}}$, was calculated by using the spin drift diffusion model, taking the spindrift effect into account [34]. The MR ratio is calculated by the equation:

$$G_e = \frac{\Delta V_{2\mathrm{T}}}{(R_{\mathrm{ch}} + R_{\mathrm{i}1} + R_{\mathrm{i}2})I}, \tag{A.24}$$

where $R_{\mathrm{ch}} = L_{\mathrm{ch}}/(\sigma_{\mathrm{ch}} wd)$ and $R_{\mathrm{i}1(2)} = \frac{RA_{\mathrm{int}}}{h1(2)w}$ are the resistance of the semiconductor channel and the interface of ferromagnetic electrodes F1(2), respectively (see Fig. A.8c). The parameters employed in the calculation are summarized in Table A.1. The values of $\Delta V_{2\mathrm{T}}$, $1/RA_{\mathrm{int}}$, and G_e are plotted after devided by the maximum of each value in Figs. A.8d, A.8e, and A.8f, respectively. The RA_{int} dependence of $\Delta V_{2\mathrm{T}}$ shows the necessity of a moderate interfae resistance (see Fig. A.8d). In the case of a small RA_{int}, the spin current injected from FM into SC mainly flow back into FM because of the large difference in the spin resistance between FM and SC, resulting in a low MR ratio. A large RA_{int} enables a highly efficient spin injection from FM to SC by inhibiting a back flow of spins [25,85]. A color contour plot of the MR ratio as a functions of RA_{int} and L_{ch} is shown in Fig. A.8f. In contrast to $\Delta V_{2\mathrm{T}}$ shown in Fig. A.8d, the MR ratio has an optimum condition of RA_{int} for each L_{ch}. The green dot indicates the values of the interface resistance and the channel length in the previous study [55]. If the L_{ch} gets shorter, the optimum condition of RA_{int} shifts lower because the resistance of SC decreases. Therefore, reduction in RA_{int} is desired to realize the high MR ratio in the future spin MOSFET with a short L_{ch}.

Table A.1: The parameters for the calculation of MR ratio in a Si-based spin MOSFET

Label	Symbol	Value	Value
Conductivity of the Si channel	σ_{ch}	1000	S/m
Conductivity of FM	σ_{FM}	10^7	S/m
Spin diffusion length of the Si channel	λ_{ch}	1.4	µm
Spin diffusion length of FM	λ_{FM}	3.0	nm
Charge current	I	10	µA
Thickness of the Si channel	d	100	nm
Width of the Si channel	w	1.0	µm
Width of F1	$h1$	0.2	µm
Width of F2	$h1$	0.2	µm
Spin polarization at teh FM/Si interface	β	0.5	–

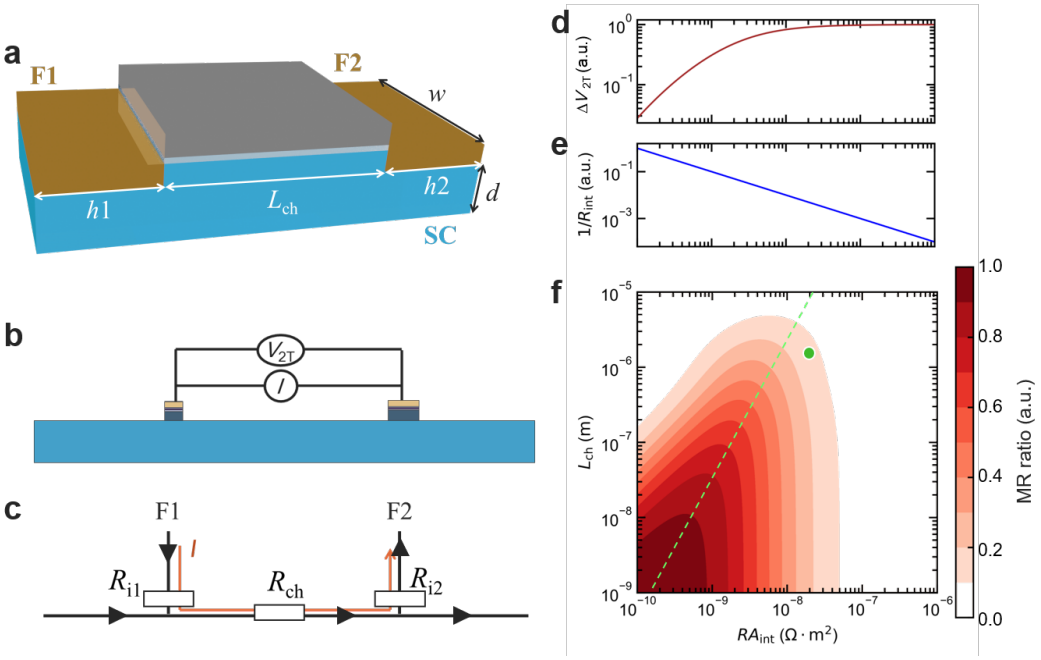

Figure A.8: Magnetoresistance ratio in future spin MOSFET.

(a) A schematic image of spin MOSFET and the two terminal configuration. **(b)** The side-view of a lateral spin-valve for measurement of the magnetoresistance (MR) ratio. **(c)** One-dimensional model of the lateral spin-valve for calculation of MR ratio. The interfacial resistance, RA_{int}, dependences of **(d)** the spin dependent voltage between F1 and F2, $\Delta V_{2\mathrm{T}}$, and **(e)** the inverse of RA_{int}. **(f)** A color contour plot of the MR ratio as a functions of RA_{int} and L_{ch}. The green circle indicates the value of the current silicon-based spin MOSFET reported in the previous study [55]. The green dashed line is guide to eyes for optimum condition at each L_{ch}.

Appendix B

List of Publications

Journals as the First Author

1. **Naoto Yamashita**, Yuichiro Ando, Hayato Koike, Shinji Miwa, Yoshishige Suzuki, and Masashi Shiraishi, "Thermally Generated Spin Signals in a Nondegenerate Silicon Spin Valve", *Physical Review Applied* **9**, 054002 (2018). Published by American Physical Society.

2. **N. Yamashita**, S. Lee, R. Ohshima, E. Shigematsu, H. Koike, Y. Suzuki, S. Miwa, M. Goto, Y. Ando, and M. Shiraishi, "Enhancement of spin signals by thermal annealing in silicon-based lateral spin valves", *AIP Advances* **10** 095021 (2020), selected as Editor ' s Pick. Published by AIP Publishing.

3. **N. Yamashita**, S. Lee, R. Ohshima, E. Shigematsu, H. Koike, Y. Suzuki, S. Miwa, M. Goto, Y. Ando, and M. Shiraishi, "Investigation of the thermal tolerance of silicon-based lateral spin valves", *Scientific Reports* **11** 10583 (2021). Published by Springer Nature.

N. Yamashita, R. Ohshima, E. Shigematsu, S. Honda, Y. Ando, and M. Shiraishi, "Large Modulation of the Work Function in an iron-based alloy", in preparation.

Journals as a co-Author

1. S. Lee, **N. Yamashita**, Y. Ando, S. Miwa, Y. Suzuki, H. Koike, and M. Shiraishi, "Investigation of spin sattering mechanism in silicon channels of Fe/MgO/Si lateral spin valves", *Applied Physics Letters* **110**, 192401 (2017). Published by AIP Publishing.

2. S. Lee, H. Koike, M. Goto, S. Miwa, Y. Suzuki, **N. Yamashita**, R. Ohshima, E. Shigematsu,Y. Ando, and M. Shiraishi, "Synthetic Rashba spin-orbit system using a silicon metal-oxide semiconductor", *Nature Materials* (2021). Published by Springer Nature.